INFORMATION TO USERS

This manuscript has been reproduced from the microfilm master. UMI films the text directly from the original or copy submitted. Thus, some thesis and dissertation copies are in typewriter face, while others may be from any type of computer printer.

The quality of this reproduction is dependent upon the quality of the copy submitted. Broken or indistinct print, colored or poor quality illustrations and photographs, print bleedthrough, substandard margins, and improper alignment can adversely affect reproduction.

In the unlikely event that the author did not send UMI a complete manuscript and there are missing pages, these will be noted. Also, if unauthorized copyright material had to be removed, a note will indicate the deletion.

Oversize materials (e.g., maps, drawings, charts) are reproduced by sectioning the original, beginning at the upper left-hand corner and continuing from left to right in equal sections with small overlaps. Each original is also photographed in one exposure and is included in reduced form at the back of the book.

Photographs included in the original manuscript have been reproduced xerographically in this copy. Higher quality 6" x 9" black and white photographic prints are available for any photographs or illustrations appearing in this copy for an additional charge. Contact UMI directly to order.

UMI®

Bell & Howell Information and Learning
300 North Zeeb Road, Ann Arbor, MI 48106-1346 USA
800-521-0600

Electron Impact Ionization and Dissociation Probed by Laser Induced Fluorescence

by

Nina Abramzon

A dissertation submitted to the graduate Faculty in Physics in partial fulfillment of the requirements for the degree of Doctor of Philosophy , The City University of New York.

1999

This manuscript has been read and accepted by the Graduate Faculty in Physics in satisfaction of the dissertation requirement for the degree of Doctor of Philosophy.

3/30/99
Date

Chair of Examining Committee

3/31/99
Date

Executive Officer

Edward A. Whittaker

Vladimir Petrarca

Frederick W. Smith

THE CITY UNIVERSITY OF NEW YORK

Abstract

Electron Impact Ionization and Dissociation Probed by Laser-Induced Fluorescence

by

Nina Abramzon

Thesis Advisor : Professor Kurt Becker

A combination of electron scattering and laser-induced fluorescence (LIF) techniques has been employed in the direct experimental determination of the absolute $N_2^+(X^2\Sigma_g)$ ionization cross section as a function of electron energy from threshold to 200 eV. Electron impact on N_2 produces N_2^+ ground-state ions which are detected by pumping the ($X^2\Sigma_g^+ \rightarrow B^2\Sigma_u^+$) (0,0) vibrational transition at 391 nm with a tunable dye laser and detecting the subsequent LIF of the ($B^2\Sigma_u^+ \rightarrow X^2\Sigma_g^+$) (0,1) vibrational transition at 428 nm. LIF spectra obtained at different electron energies yield the relative N_2^+ (X) cross section which is put on an absolute scale by independent calibration to the well-known "benchmark" cross section for the production of He atoms in the $2s\ ^3S$ state by electron impact at 20.4 eV on He in the $1s\ ^1S$ ground state. Our results are compared with the recent measurement by Doering and Yang (J. Geophysical Research, 102, 9683 (1997)) obtained from electron-electron coincidence (e,2e) experiments at 100 eV and with a recent estimate by Van Zyl and Pendelton (J. Geophysical Research, 100, 23755(1995)).

To My Parents

Acknowledgments

There are times when one thinks that one will not be able to make it , that perhaps one doesn't have and doesn't want what it takes to be a scientist. Throughout all of this there was always someone ready to help, to encourage or to give advice. These individuals softened the blows and affirmed that I was doing the right thing.

I wish to express my deep appreciation to my advisor Prof. Kurt Becker who always knew how to generate new ideas, and who gave me the momentum to complete this project. I would like to thank him for his guidance, insight and the ability to provide just enough support and just enough freedom to make this research complete, all the while increasing my interest in the subject. I would also like to thank him for his concern for those aspects in life outside of physics.

Dr. Ralph Siegel, a former graduate student in our group, was always available even long after he left the group. He patiently introduced and trained me in the LIF technique, and even came on weekends to help me out. I have learned a lot from his tutorials and from many conversations. I am extremely thankful to him.

I am thankful to my colleagues in the laboratory throughout the years for creating a pleasant atmosphere for teaching me and helping me in the lab.
I would especially like to thank Dr. Vladimir Tarnovsky, who has been a Senior Research Associate in the group for the constant interest he had shown in my work and for many interesting discussions which helped me to get a clearer physical explanation and always stimulated new ideas. I would like to thank Peter Kurunczi, a graduate student in the group for many useful suggestions, for teaching me basic lab techniques and for his constant help. I would also like to thank Larry Grone, who was a summer student working with me for being very helpful during the move of our lab from CCNY to Stevens Institute.

I would like to thank Mr. Joe Altman, the foreman in the machine shop at CCNY, who patiently introduced me to technical drawings and helped me with the designs. I would like to thank the machinists Linden and Joseph for their professional work. I would also like to thank Feng Du from the electronic shop for helping me with the computer.

I thank the faculty at CCNY for their education and advice. I would especially like to thank Prof. J. Gersten, Prof. M. Mittleman and and Prof. J. Birman. I would like to thank Prof. T. Boyer, Prof. H. Cummins and Prof. P. Nair for contributing to my interest in Physics. I would also like to thank Prof. V. Chung and Prof. N. Tzoar for helping me in my initial stages at CCNY.

I wish to thank Prof. M. Sarachik, Prof. F. Smith, Prof. R. Alfano and Prof. M. Gunner from CCNY and Prof. E. Whittaker from Stevens Institute for generously permitting me to use their equipment.

I would like to thank the members of my thesis committee, Prof. J. Gersten, Prof. F. Smith, Prof. V. Petricevic, and Prof. E. Whittaker for showing interest in my work.

Lastly I would like to thank all my friends at CCNY, too many to mention, for the exciting years I have spent here both professionally and personally .

Table of Contents

List of Figures

List of Tables

Chapter 1. Introduction

1.1 Historical Background

When electrons collide with molecules, a variety of processes may take place. These processes can be divided into two general categories, processes in which the electron transfers a portion of its kinetic energy to the excitation of an internal degree of freedom of the molecule (inelastic collisions), e.g. vibrational and/or rotational states may be excited with or without change of the electronic state, and processes in which no energy is transferred to the molecule (elastic collisions). This thesis deals with a particular category of inelastic electron-molecule collision processes, molecular ionization. Ionization refers to a process in which the incident electron removes one (or more) of the bound molecular electrons in the collision process and leaves a positively charged ion behind. In addition, the remaining ion may be left in an electronically excited state and may also be vibrationally and/or rotationally excited.

The first inelastic electron collision measurements were carried out by Lenard (1902) only five years after the discovery of the electron by Thomson (1897). Early studies included the investigation of energy losses suffered by an electron swarm in a gas by Franck and Hertz (1914), the measurement of the angular distribution of inelastically scattered electrons by Dymond (1927) and by Mohr and Nicoll (1932), the introduction of a technique for the measurement of total cross-sections for scattering of electrons by

atoms using beams by Ramsauer and co-workers (1921a, 1921b), and the development of the swarm technique for quantitative measurements of the total cross-section for electron scattering by atoms by Townsend and co-workers (1922) . The interpretation of the results obtained in the experiments of Franck and Hertz and Ramsauer and co-workers provided an experimental verification of some of the early predictions of quantum mechanics, e.g. the existence of discrete energy levels of atoms and molecules and the quantum mechanical nature of electron scattering. The possibility of spin exchange in electron-impact excitation , as pointed out by Oppenheimer (1928), made possible the study of electronic states which are not accessible by optically allowed, dipole excitation from the ground state. A comprehensive review of these early electron collision studies can be found in many reviews, e.g. in the book by Massey et al. (1969).

The early experiments had many limitations such as insufficient energy resolution in the electron beam, inefficient electron detection efficiency, and inferior vacuum techniques. Technological developments in the 1950s marked the beginning of a new age of electron collision studies. The introduction of the cylindrical energy analyzer by Marmet and Karwin (1960), the use of hemispherical energy analyzers by Lassettre and co-workers (Skerbele and Lassettre, 1964) and Simpson and co-workers (Simpson, 1964; Kuyatt and Simpson, 1967), the utilization of electron multipliers as signal detectors, and general progress in vacuum techniques and electronics opened up new avenues for the study of electron collision processes . The application of coincidence techniques and laser excitation techniques to electron collision studies and the utilization of spin-selected electron beams and target beams enabled the experimentalist to approach the "perfect scattering experiment" in which all quantum numbers associated with the system

before and after the collision process are specified and no averaging over unresolved states is required (Bederson 1969, Trajmar et al. 1984) . The advent of tunable dye lasers provided a major stimulus to the study of molecular collision processes. The high spectral purity and high light intensity in a very narrow wavelength interval provided by such lasers allowed the preparation of state-selected projectiles and targets and the state-selected detection of collision products. These are particularly useful attributes in collisions involving molecules which have a large number of narrowly spaced quantum states.

1.2 Motivation for the Present Work

Electron impact ionization and dissociation processes are phenomena of considerable practical as well as basic interest (Märk and Dunn 1985). The ionization and dissociation of molecules following electron impact are among the most basic collisional interactions between electrons and molecules. As far as applications are concerned, ionization and dissociation processes are important in astrophysics, planetary atmospheres (e.g. the plasma torus around Jupiter and its satellites), gas discharges and plasmas, radiation chemistry, mass spectrometry, and chemical analysis. In plasma-assisted material processing, the precise control of the characteristics of the process and the properties of the processed materials require a knowledge of the equilibrium (steady state) number density of various reactive neutral and ionic species in the plasma. Therefore, there is a critical need for cross section data for electron impact induced processes relevant to the creation and destruction of these species (Becker 1994). In

addition, experimental data on ionization and dissociation are vital to advance the theory of electron collisions, since they provide tests of assumptions and approximation on which these calculations are based. Not only are data required for stable atoms and molecules, but also for transient species, i.e. radicals. The detection of excited-state atomic or molecular fragments produced by electron-impact induced dissociation or ionization can use the radiation that is subsequently emitted by these species. However, in order to assess the importance of a particular dissociation channel relative to all other dissociation channels of a molecule, the production of ground-state fragments must also be taken into account. The detection and measurement of neutral ground-state species is crucial to the complete understanding of electron impact dissociation processes. The importance of experimental data for electron impact ionization and dissociation and, in particular, the dissociation into ground-state fragments and the ionization into state-selected ions provided the motivation for us to study the electron impact ionization and dissociation of certain molecules by using laser-induced fluorescence (LIF) to detect a specific product of an electron-impact ionization/dissociation process. The experiments are carried out in an apparatus which employs three intersecting beams , electron beam, laser beam and target gas beam (triple-beam apparatus). This triple beam apparatus for the study of electron-impact processes, in which the products are in their ground state, was designed as part of previous thesis project (Siegel 1996). The conceptual idea of this experiment is to measure cross sections for the production of electron-impact produced molecular fragments in their ground electronic state by using laser induced fluorescence to measure the population densities of these species. The first process that

was studied was the electron-impact ionization of N_2, leading to the formation of N_2^+ ions in their electronic ground state

$$N_2 + e^- \rightarrow N_2^+\left(X^2\Sigma_g^+\right) + 2e^- . \qquad (1.2.1)$$

We are able to study the above reaction (1.2.1) because the $N_2^+(X\,^2\Sigma_g)$ product ions can be detected by LIF. The N_2^+ $(X\,^2\Sigma_g)$ production can be distinguished from all other ground-state electron-impact produced species such as N_2, N and N^+ by its unique and well-known absorption spectrum (Lofthus et al. 1977). The N_2^+(X→ B) transition has a wavelength which makes it easily accessible to tunable dye-lasers. In addition, the excited molecules emit before they leave the interaction region, i.e. their lifetime is sufficiently short.

LIF techniques applied to measurements of ground state species produced by electron-impact on a molecule under single collision condition have been carried out by other groups. McCconkey and co-workers (using a supersonic gas beam and a pulsed electron beam) (Darrach 1990, Zetner et al. 1988) estimated the cross section for electron-impact ionization of N_2 (Darrach 1990) and studied the rotational distribution of N_2^+(X) ions (Zetner et al. 1988). We use an effusive gas beam and a continuous electron beam in an effort to measure the cross section for the same process. The use of an effusive gas beam and a continuous electron beam simplifies the timing sequence of the experiment and reduces the systematic uncertainties of such a measurement. However, the fluorescence produced by the LIF process is the same as the fluorescence produced continuously in the process

$$N_2 + e^- \rightarrow N_2^+\left(B^2\Sigma_u^+\right) + 2e^- \quad . \qquad (1.2.2)$$

and both fluorescence signals are produced simultaneously. Therefore, the LIF signal is more difficult to isolate in our experiment.

As part of a previous thesis project (Siegel 1996), preliminary data for the above process have been obtained. The preliminary data suffered mainly from a poor signal-to-noise ratio. The main objectives of the present thesis project are i) significant improvements in the signal-to noise ratio, ii) a measurement of the relative cross section for the formation of $N_2^+(X)$ ions, and iii) the independent absolute calibration of the relative cross section data.

Chapter 2. Background

2.1 Molecular Spectroscopy using Laser Induced Fluorescence

Basic Concepts:

Laser induced fluorescence (LIF) is a technique in which an atom, ion or molecule absorbs a resonant photon provided by a laser and spontaneously re-emits a photon of the same or a different wavelength after a characteristic time, the lifetime of the excited state of the atom, ion or molecule.

Some Concepts from the Theory of the Spectra of Diatomic Molecules:

Classification of Molecular Electronic States

The fact that the masses of the atomic nuclei in a molecule are very large compared with the masses of the electrons plays an important part in the theory of molecular spectra. Because of this difference in the respective masses, the velocity of the nuclei in the molecule can usually be neglected compared with the velocities of the electrons. This is the basis of the Born Oppenheimer approximation which assumes that the electrons move relative to the nuclei which are fixed in space. The Hamiltonian for such a system of nuclei and electrons has the form

$$H = -\frac{\hbar^2}{2m}\sum_i \nabla_i^2 - \sum_A \frac{\hbar^2}{2M_A}\nabla_A^2 - \sum_{A,i}\frac{Z_A e^2}{r_{Ai}} + \sum_{A>B}\frac{Z_A Z_B e^2}{R_{AB}} + \sum_{i>j}\frac{e^2}{r_{ij}} \qquad (2.1.1)$$

(kinetic energy of the electrons) (kinetic energy of the nuclei) (electron - proton attraction) (proton - proton repulsion) (electron - electron repulsion)

In order to solve the Schrödinger equation with this Hamiltonian in an effort to find the energy levels of the molecule, one assumes that the wave function is separable into a nuclear part and an electronic part (Born Oppenheimer approximation) as follows:

$$\Psi_{\text{molecular}}(r,R) = \Psi_e(r;R)\ \chi_N(R) \qquad (2.1.2)$$

The Born-Oppenheimer approximation assumes that the set of nuclear coordinates R is constant, that is the nuclei are stationary. The molecular potential is a sum of all Coulomb potentials in which the electrons move and interact with one another. If we use the above product wave function in the Schrödinger equation for the molecule, we find that it can be separated into two equations, one for Ψ_e and one for χ_N :

$$H_e\Psi_e = \left\{-\frac{\hbar^2}{2m}\sum_i \nabla_i^2 - \sum_{A,i}\frac{Z_A e^2}{|R_A - r_i|} + \sum_{i>j}\frac{e^2}{r_{ij}}\right\}\Psi_e = E_e(R_A)\Psi_e(R_A) \qquad (2.1.3\text{-a})$$

$$H_N\chi_N = \left\{-\sum_A \frac{\hbar^2}{2M_A}\nabla_A^2 + E_e(R_A) + \sum_{A>B}\frac{Z_A Z_B e^2}{|R_A - R_B|}\right\}\chi_N = E_{\text{total}}\chi_N \qquad (2.1.3\text{-b})$$

A solution of the first equation yields the electronic energy levels of the molecule. Unlike the energy levels of atoms which are uniquely labeled by quantum numbers, the molecular energy levels are still a function of the separation between the various nuclei in the molecule. In the simple case of diatomic molecule AB, the electronic energy levels depend on the internuclear distance R_{AB}. Whereas atomic energy levels are classified corresponding to the total orbital angular momentum L of all (valence) electrons, such a classification is not possible for molecules. In diatomic molecules, the electric field has axial symmetry about the internuclear axis. The projection of the orbital angular momentum on this axis is conserved (i.e. a constant of the motion) and we can classify the electronic energy levels of the molecule according to the value of this projection. The angular momenta of the electrons in a diatomic molecule are L_A (total electronic orbital angular momentum of atom A) and L_B (total electronic orbital angular momentum of atom B) and their sum is $L= L_A+ L_B$ and the component of this sum along the internuclear axis of the molecule is Λ. Λ can have values ranging from 0,1,2,... L_A+L_B . The symbols used to denote states with different values of Λ are analogous to those used in atoms, i.e. :

$\Lambda=0$,1 ,2 ,3 corresponding to Σ, Π, Δ, Φ states

Each electronic state of a diatomic molecule is further characterized by the total spin $S=S_A+S_B$ of all the electrons in the molecule. If S is not zero, there is a (2S+1) fold

degeneracy with respect to the direction of the total spin. This is called the multiplicity of the term as in the case of an atom and is written as an superscript preceding the term. For the classification of molecular electronic states, there are additional symmetry properties of the electronic eigenfunctions that have to be considered. These symmetry properties depend on the symmetry properties of the field in which the electrons move. In a diatomic molecule, any plane through the internuclear axis is a plane of symmetry. Therefore, the electronic eigenfunctions of a non-degenerate state (e.g. a Σ state) either remain unchanged or change sign when reflected at a plane passing through both nuclei. In the first case, the state is called a Σ^+ state and in the second case it is called a Σ^- state. If the two nuclei in the molecule have the same charge, the field in which the electrons move has in addition a center of symmetry. The field remains unaltered by a reflection of the atom at this center of symmetry (the midpoint of the internuclear axis). As a consequence of this symmetry, the electronic eigenfunctions remain either unchanged or change sign when reflected relative to this center of symmetry. In the first case, the state to which the eigenfunction belongs is called an even state, and in the second case it is called an odd state. This symmetry property, even or odd, is indicated by adding a subscript (g) or (u) to the term symbol. Thus, $^2\Sigma_g^+$ donates a term with Λ=0, S=1/2 and the electronic eigenfunction remains unchanged 1) upon reflection through plane passing through both nuclei (+) and 2) upon reflection relative to the center of symmetry (g).

Selection rules

The selection rules which determine the electronic transitions in diatomic molecules are as follows:

$$\Delta\Lambda = 0,\pm 1 \qquad (2.1.4\text{-a})$$

$$\Delta\Sigma = 0 \qquad (2.1.4\text{-b})$$

$$\Delta\Omega = 0,\pm 1 \qquad (2.1.4\text{-c})$$

Here Λ is the component of the sum of the orbital angular momenta along the internuclear axis of the molecule, Σ is the component of the sum of the spins of all electrons in the molecule along the internuclear axis, and Ω is the quantum number of the resultant electronic angular momentum along the internuclear axis, $\Omega = |\Lambda + \Sigma|$. In addition, (+) states combine only with (-) states while (g) states combine only with (u) states.

The total energy E of the molecule may be approximately represented as a sum of the electronic energy, the vibrational energy and the rotational energy, i.e.,

$$E = E_e + E_{vib} + E_{rot} \qquad (2.1.5)$$

In diatomic molecules, the vibration of nuclei takes place along the internuclear axis of the molecules, while the rotation takes place about a line perpendicular to the axis of the molecule. In a first approximation, the vibration of the two nuclei can be described by a harmonic oscillator potential (to which an anharmonic term has to be added to

adequately describe large amplitude vibrations). In this harmonic oscillator approximation, the vibrational energy (of the lower vibrational levels) is given by

$$E_{vib} = \hbar w_e (v + \frac{1}{2}) \qquad (2.1.6)$$

where w_e is the characteristic frequency of the vibration and $v = 0,1,2...$ is the corresponding vibrational quantum number. If anharmonic terms in the potential are taken into account, the expression for the vibrational energy becomes:

$$E_{vib} = \hbar w_e (v + \frac{1}{2}) - \hbar\, w_e x_e (v + \frac{1}{2})^2 + ... \qquad (2.1.7)$$

where x_e is the so-called anharmonic constant. There are no rigorous selection rules for the quantum number v and hence each vibrational state of an electronic state can combine with any vibrational state of another electronic state as long as the electronic states satisfy the previously stated selection rules for electronic transitions.

The rotational energy is, in a first approximation, given by the energy levels of a quantized rigid rotator

$$E_{rot} = \frac{h^2}{8\pi^2 I} J(J+1) = hBJ(J+1) \qquad (2.1.8)$$

In this expression I is the moment of inertia of the molecule, J is the rotational angular momentum quantum number (J= 0,1,2,3....), and B is the rotational constant. Each rotational state has (2J+1) sublevels associated with the quantum number M (= -J,...0...,J), which defines the projection of J onto an arbitrary space-fixed axis. This degeneracy arises from the symmetry of the three dimensions in space and may be removed by the application of an external field. Transitions are allowed between those states for which the transition dipole integral $\langle J, M | \mu | J', M' \rangle$ is non-zero. The components of the dipole moment vector in terms of the spherical polar angles (θ,ϕ) are:

$$\mu_x = \mu_0 \sin\theta \cos\phi \qquad (2.1.9\text{-a})$$

$$\mu_y = \mu_0 \sin\theta \sin\phi \qquad (2.1.9\text{-b})$$

$$\mu_z = \mu_0 \cos\theta \qquad (2.1.9\text{-c})$$

where μ_0 is the permanent dipole moment of the molecule. Note that molecules without permanent moments have no pure rotational spectrum. The transition dipole matrix elements also vanish unless J=J±1 and M=M' or M'±1. The selection rules are, therefore, $\Delta J = \pm 1$ and $\Delta M = 0, \pm 1$.

Angular Momentum Coupling cases:

When we analyze the rotational level structure of molecules, we need to take into account the coupling of the electronic angular momentum to the molecular rotation. While strictly speaking none of the individual angular momenta are truly constants of motion, there are several limiting coupling cases which describe fairly accurately the angular momentum coupling for many molecules. These are known as Hund's coupling cases (Herzberg 1950). Hund's cases (a) and (b) are the most important of the five coupling cases that can be distinguished (Herzberg 1950).

Hund's case (a)

In this coupling scheme, the strongest interaction is the electronic interaction which couples the electron spin (S) and the orbital angular momentum (L) separately to the molecular (internuclear) axis. The projection of L on the axis is designated by Λ and the projection of S is labeled Σ. Their sum is donated by Ω, $\Omega = \Lambda + \Sigma$. Ω couples to the rotational angular momentum N of the nuclear motion to form the total angular momentum J. The conserved quantities in this coupling scheme are J^2, J_z, and Ω . This coupling case is depicted in figure (2.1.1-a). The quantum number J can assume the values $\Omega + N$, where $N = 0,1,2...$ The rotational energy levels are given by

$$\left[\frac{h^2}{8\pi^2\mu R_e^2}\right] N^2 = B\left[J(J+1) - \Omega^2\right] . \qquad (2.1.10)$$

The total energy of the vibronic contribution to the energy has the form

$$B\left[J(J+1)-\Omega^2\right]+A\Omega^2 = BJ(J+1)+(A-B)\Omega^2 \ , \qquad (2.1.11)$$

where A is essentially the molecular spin-orbit coupling constant .

Hunds case b:

When $\Lambda=0$, but $S\neq 0$ in a diatomic molecule, Hund's coupling case (b) depicted in figure (2.1.1-b) generally applies. Here S does not couple to the internuclear axis and the electron spin remains fixed in space while the molecule rotates. The angular momentum component Λ and the rotational angular momentum N form K, which is the total angular momentum apart from the spin. The total quantum number J can assume values $J=K+1/2$ and $J=K-1/2$. This splitting of the energy level with a fixed values of J due to the coupling of the electronic spin to the rotational motion of the molecule is known as ρ- doubling.

Hund's Case A

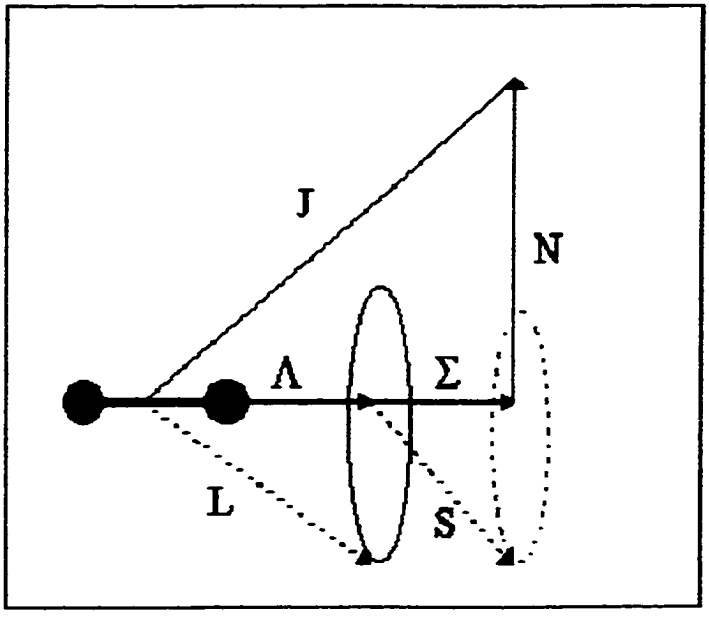

Figure (2.1.1-a)

Hund's Case B

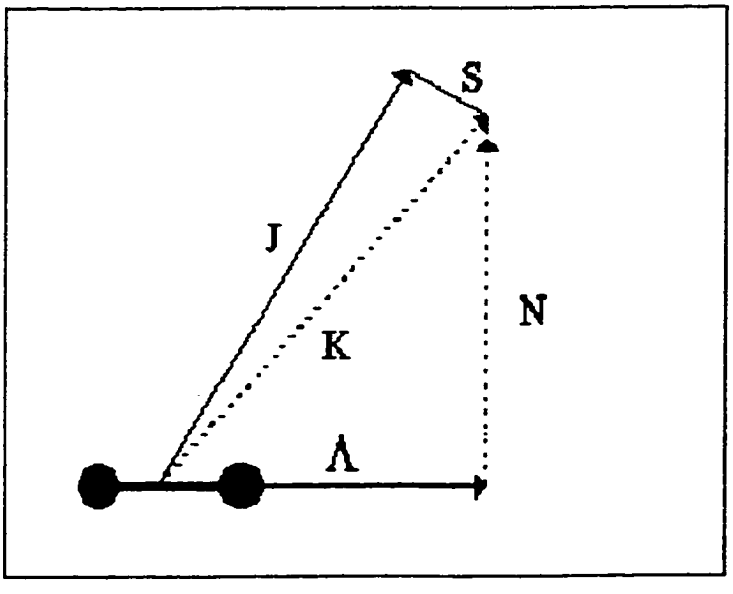

Figure (2.1.1-b)

Theoretical Details Of Molecular Spectroscopy by LIF

As a starting point, we assume that a specific rotational -vibrational (ro-vibronic) level E_k (v_k', J_k') of an excited electronic state of a diatomic molecule has been selectively populated by optical pumping from the ground state. The excited molecules undergo spontaneous transitions to a lower level E_m (v_m", J_m") with a mean lifetime of $\tau_k = \frac{1}{\sum_m A_{km}}$ (where A_{km} is the spontaneous transition probability and the sum extends over all states m of lower energy to which the excited state can decay according to the applicable selection rule). If we denote the population density in the excited state by N_K (v_k', J_k'), the intensity I_{km} of the fluorescence with frequency $\nu_{km} = \frac{E_k - E_m}{h}$ is given by

$$I_{km} \propto N_k A_{km} h \nu_{km} \quad . \tag{2.1.12}$$

The spontaneous transition probability A_{km} is proportional to the square of the matrix element

$$A_{km} \propto \left| \int \psi_k^* \cdot \bar{r} \cdot \psi_m d\tau_n d\tau_{el} \right|^2 \tag{2.1.13}$$

where the integration extends over all nuclear and electronic coordinates. The total wave function can be separated into a product of electronic, vibrational , and rotational wave functions

$$\psi = \psi_{el}\psi_{vib}\psi_{rot} \quad , \tag{2.1.14}$$

if the Born-Oppenheimer approximation holds. The total transition probability is then proportional to the product of three factors

$$A_{km} \propto |M_{el}|^2 |M_{vib}|^2 |M_{rot}|^2 \quad , \tag{2.1.15}$$

The first factor represents the electronic matrix element which depends on the coupling of the two electronic states. The second factor is the so-called Franck-Condon factor which couples the two vibrational levels. The underling assumption is that the electronic transition occurs in a time that is short compared to the vibrational period. Therefore, the position of the nuclei and their velocity does not change during the electronic transition. The third factor is the so called Hönl-London factor which represents the intensity distribution of the rotational lines under the assumption of negligible interaction of the rotational and electronic motion. Only those transitions for which all three factors are non-zero have a non-vanishing fluorescence intensity. The Hönl-London factors are always zero unless $\Delta J = J_k' - J_m'' = 0, \pm 1$. If a single upper level (v_k', J_k') has been selectively excited, each vibrational band $v_k' \rightarrow v_m''$ consists of at most three sub-bands :

a P band ($J' - J'' = -1$), a Q band ($J' - J'' = 0$), and an R band ($J' - J'' = +1$). For diatomic homonuclear molecules, additional symmetry selection rules further reduce the number of possible transitions. For $\Sigma_u \rightarrow \Sigma_g$ transitions, only P and R bands are allowed .

In the present thesis, we use LIF to probe the rotational population in the $N_2^+ (X^2\Sigma_g^+)$ ground state produced by electron impact ionization of N_2 . Specifically, the laser is tuned to pump the ($X^2\Sigma_g^+ \rightarrow B^2\Sigma_u^+$) ($v'=0$, $v''=0$) vibrational band and the resulting absorption is measured by monitoring the subsequent ($B^2\Sigma_u^+ \rightarrow X^2\Sigma_g^+$) ($v'=0$, $v''=1$) spontaneous emission as shown schematically in figure (2.1.2) (the rotational spacings are not to scale)

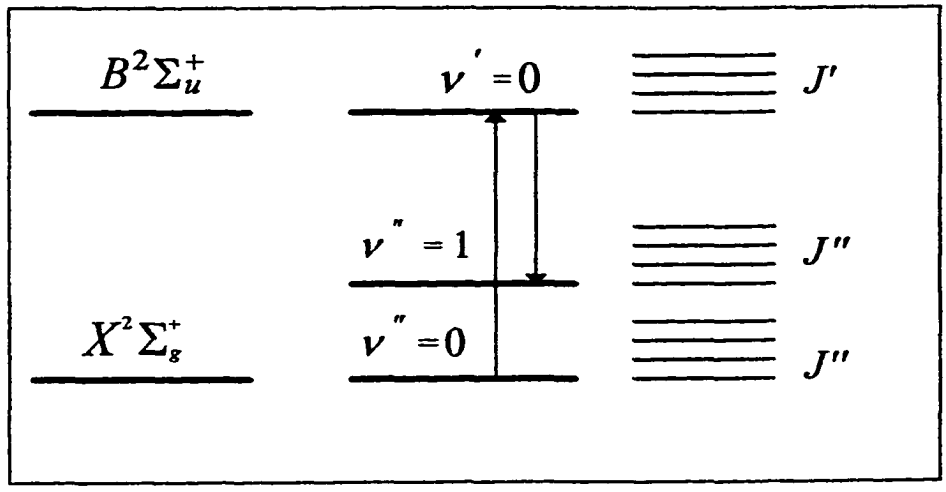

Figure (2.1.2)

Rotational Structure of the $N_2^+(B^2\Sigma_u^+ \rightarrow X^2\Sigma_g^+)$ Band System:

The $(B^2\Sigma_u^+ \rightarrow X^2\Sigma_g^+)$ band system of N_2^+ is rather accurately described by Hund's coupling case (b) (Herzberg 1950). Except for the splitting due to the coupling of the electronic spin to the rotational motion of the molecule (ρ - doubling) and the intensity alteration of successive lines in the rotationally resolved spectrum (rotational lines) due to the extra symmetry of the eigenfunctions of homonuclear diatomic molecules (see below), the rotational structure of the $N_2^+(B^2\Sigma_u^+ \rightarrow X^2\Sigma_g^+)$ band system shows the simplest possible structure for transition involving two electronic states of a diatomic molecule. The ρ-doubling causes a splitting of the lines of the R and P branches, which appear as single lines for $^1\Sigma \leftrightarrow {}^1\Sigma$ transition, into two components. This splitting is very small (< 0.01 Å) for small rotational quantum numbers (J" <10) (Bouchoux et al. 1976). Since the bandwidth of our laser is approximately 0.01Å and the intensity of the lines of the P branch has a maximum for $J'' = 7$ (corresponding to room temperature), it is very unlikely that the ρ- doubling will be observed in the present experiment. As a consequence, the rotational structure of the $N_2^+(B^2\Sigma_u^+ \rightarrow X^2\Sigma_g^+)$ spectrum can be treated similar to a $^1\Sigma \leftrightarrow {}^1\Sigma$ transition, i.e. we can assume single R and P branches .

The intensity alteration of successive lines of the rotationally resolved spectrum mentioned above is a phenomenon which effects only homonuclear molecules, such N_2^+. It is the result of the symmetry of the molecule under the exchange of its nuclei. This results in a special symmetry property of the eigenfunctions and leads to a selection rule which governs the intensity. All eigenfunctions of a homonuclear diatomic molecule are either symmetric or antisymmetric with respect to the exchange of the individual nuclei.

This results in the general (and very powerful) selection rule that prohibits symmetric levels from combining with anti symmetric levels under any kind of interaction. The intensity of successive lines of the rotational spectrum then follows from the fact that these lines originate successively from symmetric and anti-symmetric levels. Symmetric and anti-symmetric levels carry different statistical weights for homonuclear diatomic molecules. In the case of N_2^+ the result is a ratio of 2:1 for symmetric to anti-symmetric lines. For the $^2\Sigma$ ground state of N_2^+, levels with an even value of J are symmetric, levels with an odd value of J are anti-symmetric This results in the observed 2:1 intensity ratio of even to odd levels (see figure 2.1.3) (Siegel 1996).

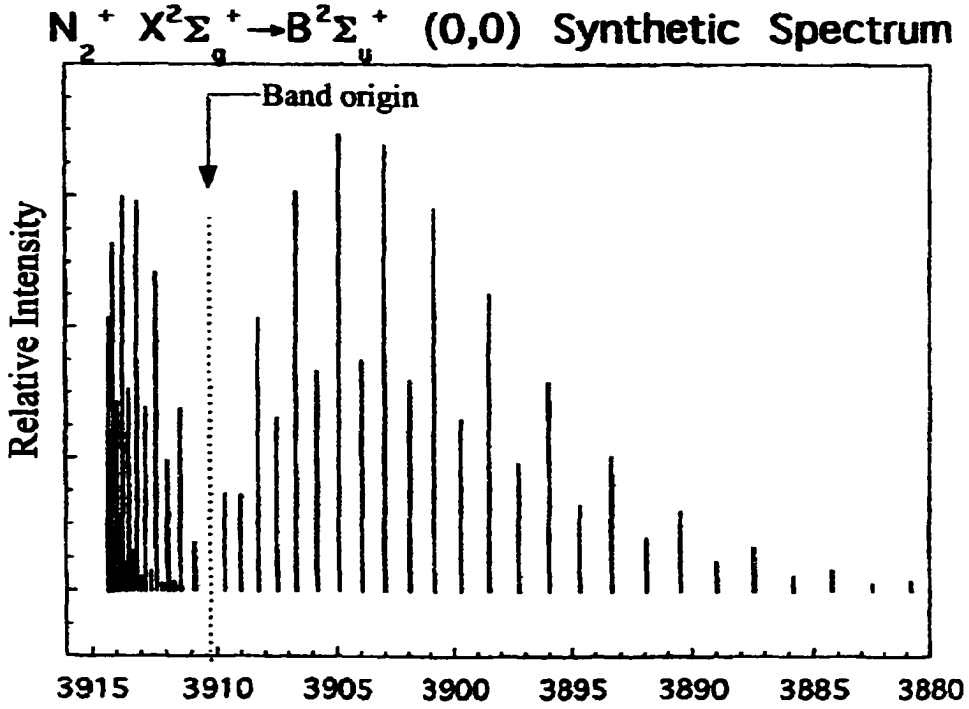

Figure (2.1.3)

The Polarization of the Laser Induced Fluorescence

In the current experiment, where the incident electron beam is unpolarized the value of the polarization of the electron impact induced fluorescence is zero (Fano el al. 1973). However, the fixed polarization of the laser leads to polarized fluorescence, even under conditions of isotropic distribution of angular momentum vectors. The polarization of the laser induced fluorescence results from the dependence of the electrical dipole transition matrix element on the orientation of the angular momentum vector of the molecule in the initial state **m**. Specifically for linearly polarized light the absorption probability is proportional to $(\hat{\varepsilon}\cdot\vec{\mu}\,)^2$ where $\hat{\varepsilon}$ is the polarization axis of the laser and $\vec{\mu}$ is the transition dipole moment of the $\mathbf{m} \rightarrow \mathbf{k}$ transition ($\vec{\mu} = -e\,\langle m|\vec{r}|k\rangle$). The direction of $\vec{\mu}$ has a fixed relationship relative to the orientation of the angular momentum vector $\vec{J}$, which depends on the magnitude J of the initial state **m** and on the ΔJ involved in the $\mathbf{m} \rightarrow \mathbf{k}$ transition (Case et al. 1978). Therefore, the transition probability of the molecule in an initial state **m** depends on the orientation of the angular momentum vector with respect to the polarization of the laser. Figure (2.1.4) shows the variation of the observed intensity as a function of J due to the variation of the polarization. The observed intensity is shown for two different experimental configurations, observation parallel and perpendicular to the polarization axis of the laser (Green et al. 1983). As shown, the variation is large for $J \leq 2$, but is small for large J. Therefore, in the present experiment the error caused by the intensity variation due to the polarization effect will not be significant when extracting populations from the LIF measurements .

Variation of The LIF Intensity as a Function of J Due to Variation in Polarization

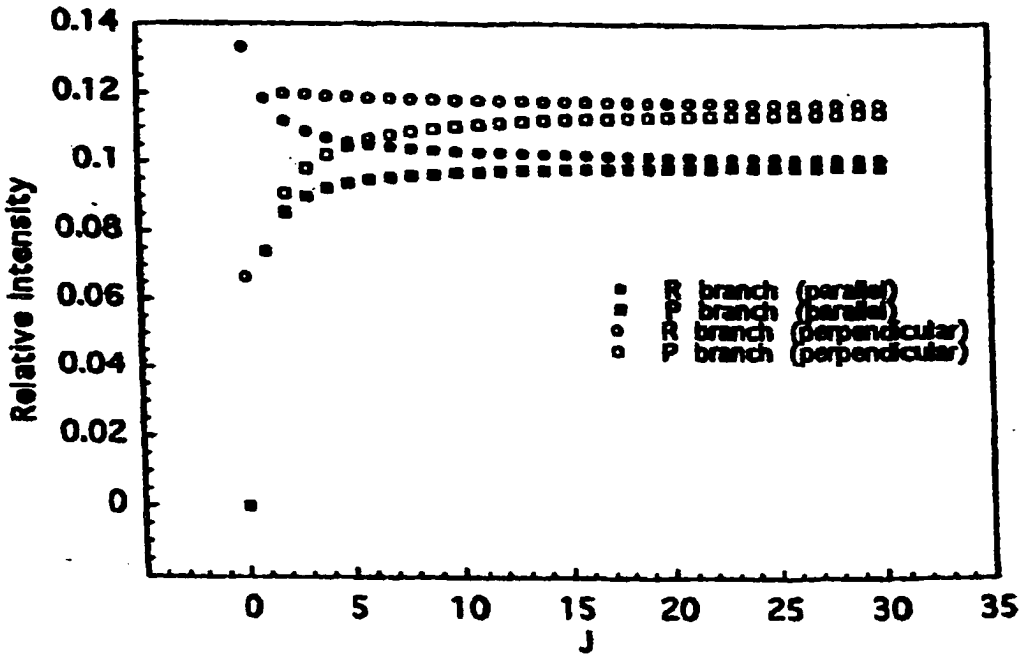

Figure 2.1.4

2.2 The Concept of the Collision Cross Section

Classification of collisions:

A number of different processes may result from the encounter of an electron with a gas atom or molecule. These may be distinguished as elastic, inelastic, superelastic, or radiative. In an elastic collision, no energy exchange takes place between the internal motion of the atom and the electron. In an inelastic collision, some kinetic energy is transferred from the electron to the internal motion of the target. Further classification of collision processes may be carried out by distinguishing the state of internal motion that is excited. First of all, a broad distinction may be made between ionization and non-ionizing collisions, depending on whether or not sufficient energy is transferred to lead to the ejection of one or more electrons from the target. Non-ionizing inelastic collisions will result in the excitation of distinct target states, so that the specification of the excited state provides further classification. Ionizing collisions may be analyzed further in terms of the number of electrons ejected from the target and the energy of the ejected electrons. Superelastic collisions in which the outgoing electron is more energetic than the incoming electron can only occur between an electron and an excited target. The electron gains energy from the internal motion of the target. Collisions which result in the subsequent emission of electromagnetic radiation are sometimes separated from other inelastic collisions and referred to as radiative collisions.

The definition of the collision cross section

Consider a parallel beam of electrons of uniform velocity passing through a gas consisting of solid spherical targets each having a cross sectional area of σ [cm^2] . If there are N such targets/cm^2, the probability that an electron will undergo a collision when moving a small distance δx [cm] through the gas is given by the product $N\sigma\delta x$. The magnitude of the beam current lost after traversing a distance δx from an initial point P is given by

$$\delta I = N \sigma I_p \delta x \qquad (2.2.1)$$

where I_p denotes the beam current at P. If P is at a distance x from the origin x=0, integration yields

$$I_P = I_0 e^{-N\sigma x} \qquad (2.2.2)$$

where I_0 is the beam current at x=0. The above definition yields the total effective cross section for all types of collisions between the electron and the target. No distinction has yet been made between elastic collisions and the various kinds of inelastic, superelastic , or radiative collisions. In order to do this, we may assign probabilities $P_o(v)$, $P_n(v)$, etc., which represent the probability (cross section) that a collision of an electron of velocity v with a target atom or molecule is elastic or inelastic, involving excitation of the nth state of the atom or molecule, etc. These quantities can be expected to vary with the electron

velocity. The cross section $P_o(v)\,\sigma$ is then defined as the effective cross section for elastic collisions of electrons of velocity v with the target concerned, $P_n(v)\,\sigma$ is the effective cross section for inelastic collisions involving excitation of the nth target state, etc. We then have (Massey et al. 1969)

$$\begin{aligned}\sigma &= P_o(v)\sigma(v) + \sum P_n(v)\sigma(v) \\ &= \sigma_o + \sum \sigma_n\end{aligned} \qquad (2.2.3)$$

Here we have written σ_O, σ_n, etc., respectively, for the individual cross sections.

The Electronic Structure and Ionization Mechanism of N_2

The electron configurations of the $X^2\Sigma_g^+$ ground state of N_2 and the $X^2\Sigma_g^+$ ground state and the $B^2\Sigma_u^+$ excited state of N_2^+ are as follows (Lofthus et al. 1977)

$$N_2(X^1\Sigma_g^+): (\sigma_g 1s)^2(\sigma_u 1s)^2(\sigma_g 2s)^2(\sigma_u 2s)^2(\pi_u 2p)^4(\sigma_g 2p)^2 \qquad (2.2.4\text{-a})$$

$$N_2^+(X^2\Sigma_g^+): (\sigma_g 1s)^2(\sigma_u 1s)^2(\sigma_g 2s)^2(\sigma_u 2s)^2(\pi_u 2p)^4(\sigma_g 2p) \qquad (2.2.4\text{-b})$$

$$N_2^+(B^2\Sigma_u^+): (\sigma_g 1s)^2(\sigma_u 1s)^2(\sigma_g 2s)^2(\sigma_u 2s)\,(\pi_u 2p)^4(\sigma_g 2p)^2 \qquad (2.2.5\text{-c})$$

The N_2^+ ($X^2\Sigma_g^+$) ground state results from removal of one $\sigma_g 2p$ outer valence electron and the N_2^+ ($B^2\Sigma_u^+$) excited state results from the removal of one $\sigma_u 2s$ inner valence electron from the ground state configuration of N_2 (Fons et al. 1994). The

N_2^+ ($B^2\Sigma_u^+ \rightarrow X^2\Sigma_g^+$) emission is due to the $\sigma_g 2p \rightarrow \sigma_u 2s$ electronic transition. There is a difference between the ionization mechanism leading to the formation of N_2^+ ($X^2\Sigma_g^+$) ions compared to N_2^+ ($B^2\Sigma_u^+$) ions. N_2^+ ($B^2\Sigma_u^+$) from N_2 (X) are formed by electron impact via a pure dipole interaction; i.e. the final Σ_u^+ state is connected to the initial Σ_g^+ state via a dipole allowed transition. This is not the case for the production of N_2^+ ($X^2\Sigma_g^+$) ions , since the final state is a Σ_g^+ state and Σ_g^+ states do not combine with other Σ_g^+ states in the dipole approximation (Herzberg, 1950). A $\Sigma_g^+ \leftrightarrow \Sigma_g^+$ dipole transition with $\Delta J = \pm 1$ violates the rigorous selection rule that symmetric states does not combine with anti-symmetric states. However , there is contrary evidence that points to the production of N_2^+ ($X^2\Sigma_g^+$) ions through interactions that are dipole in character. This evidence comes from partial photoionization ($h\nu + N_2 \rightarrow N_2^+$ (various final states) + e + kinetic energy) experiments in which cross section for the production of the various final states of the N_2^+ ion were determined (Brion et al. 1981). These experiments revealed that $N_2^+(X^2\Sigma_g^+)$ ions are produced with a probability as large or larger than the N_2^+ ($B^2\Sigma_u^+$) ions . Additional evidence comes from an estimate of the cross section for the process $N_2 + e^- \rightarrow N_2^+(X^2\Sigma_g^+) + 2\ e^-$ at high incident electron energies. It has been suggested (Zetner et al. 1988) that the production of $N_2^+(X^2\Sigma_g^+)$ ions proceeds through an excited complex that consists of a $^1\Sigma_u^+$ or $^1\Pi_u$ ionic core plus an ejected electron which rapidly autoionizes to the final $^2\Sigma_g^+$ state of the N_2^+ ion. In this model, the ejected electron carries away the odd parity necessary to preserve the overall dipole character of the $\Sigma_g^+ \leftrightarrow \Sigma_g^+$ transition .

Estimate of the $N_2(X^1\Sigma_g^+) + e^- \rightarrow N_2^+(X^2\Sigma_g^+) + 2e^-$ cross section.

The cross section for the production of N_2^+ ions in the ground state $N_2^+(X^2\Sigma_g^+)$ by electron impact on N_2 can be estimated crudely from previously measured cross sections. Specifically, we have $\sigma [N_2^+(X^2\Sigma_g^+)] = \sigma [N_2^+ (\text{total})] - \Sigma \sigma [N_2^+ (\text{excited state})]$ where $\sigma [N_2^+ (\text{total})]$ and $\sigma [N_2^+ (\text{excited state})]$ are the cross sections for the production of N_2^+ ions into all final states and into a specific excited state, respectively. Itikawa et al. (1986) summarized cross sections for electron impact ionization of N_2 and there have been recent measurements of the total and partial N_2 ionization cross sections by Krishnakumar and Srivastava (1990) who compared their data with all previous measurements. They state that their cross section for N_2^+ production is accurate to within $\pm 8\%$. The only excited ionic states of N_2^+ with appreciable cross sections are the $A^2\Pi_u$ and $B^2\Sigma_u^+$ states. More highly excited states of N_2^+ exist, e.g. the $C^2\Sigma_u^+$ and $A^2\Pi_u$ states, but since emissions from those states is very weak, it is safe to say that they do not contribute significantly to the total N_2^+ production (Fons et al. 1994). $N_2^+(A)$ state excitation measurements have resulted in conflicting results as discussed by Piper et al. (1986) with discrepancies of more then a factor of 2. This is probably due to the long lifetime of this state (~10 μs), which makes it (i) difficult to collect all emitted photons from its optical decay and (ii) makes an optical photoemission experiments susceptible to collisional quenching. If we accept the "best guess" of Piper et al. (1986) for the $N_2^+(A)$ cross section, we obtain the $N_2^+(X)$, $N_2^+(A)$, and $N_2^+(B)$ cross sections shown in figure (2.2.1) (Siegel 1996).

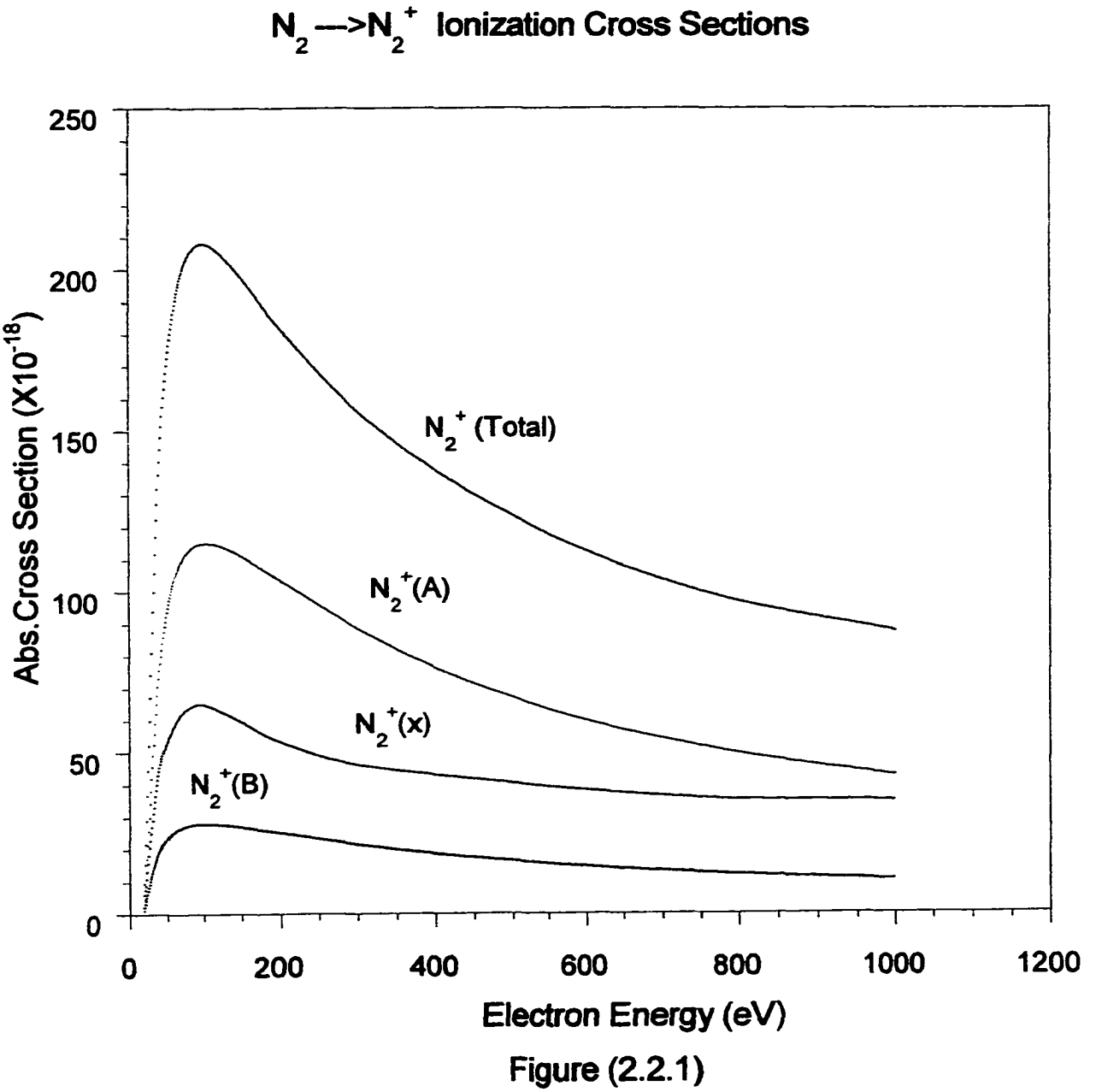

Figure (2.2.1)

Table (2.2.1) summarizes the "best guess" values of the cross sections for electron impact ionization of N_2 at 100eV

N_2^+ final state	Cross Section [$10^{-18}cm^2$]	Reference
$N_2^+(total)$	208 ± 17 ($\pm 8\%$)	Srivastava et al.(1990)
$N_2^+(A)$	115 ± 23 ($\pm 20\%$)*	Piper et al (1986)
$N_2^+(B)$	28 ± 3 ($\pm 10\%$)	Borst and Zipf (1970)
$N_2^+(X)$	65 ± 43 ($\pm 66\%$) *	Subtraction

(Table 2.2.1)

* If we use a more realistic error estimate of the N_2^+(A) cross section of $\pm 60 \times 10^{-18}$ cm^2 ($\pm 60\%$), the error of the N_2^+(X) cross section increases to $65 \pm 80 \times 10^{-18} cm^2$ at 100 eV. It is obvious that the large uncertainty of the N_2^+(A) cross section makes it impossible to estimate the N_2^+(X) cross section with any reasonable level of confidence.

Chapter 3. The Experimental Setup

3.1 Overview

The core of the experimental set-up consists of three beams (electron beam, laser beam, molecular gas beam) which intersect inside a high vacuum chamber. The electron beam is produced by an electrostatic 160^0 electron monochromator. The gas beam (which intersects the electron beam at right angles) is an effusive beam emanating from a multi - capillary nozzle. The laser beam (which counter propagates the electron beam) is produced by an excimer - pumped dye laser. Optical detection is made in the direction perpendicular to both the electron beam and the gas beam. The entire triple-beam set-up is housed in a stainless - steel vacuum chamber which is pumped by a turbo - molecular pump station. Gated photon detection techniques are employed to record the LIF signal.

A schematic diagram of the experimental arrangement is shown in figure (3.1.1).

Each component of the experimental set-up will be discussed separately in the following sub-sections. Since a detailed description of the original apparatus has been given in a previous thesis (Siegel 1996), the experimental description here will be limited to those components that have been developed or significantly improved as part of this thesis.

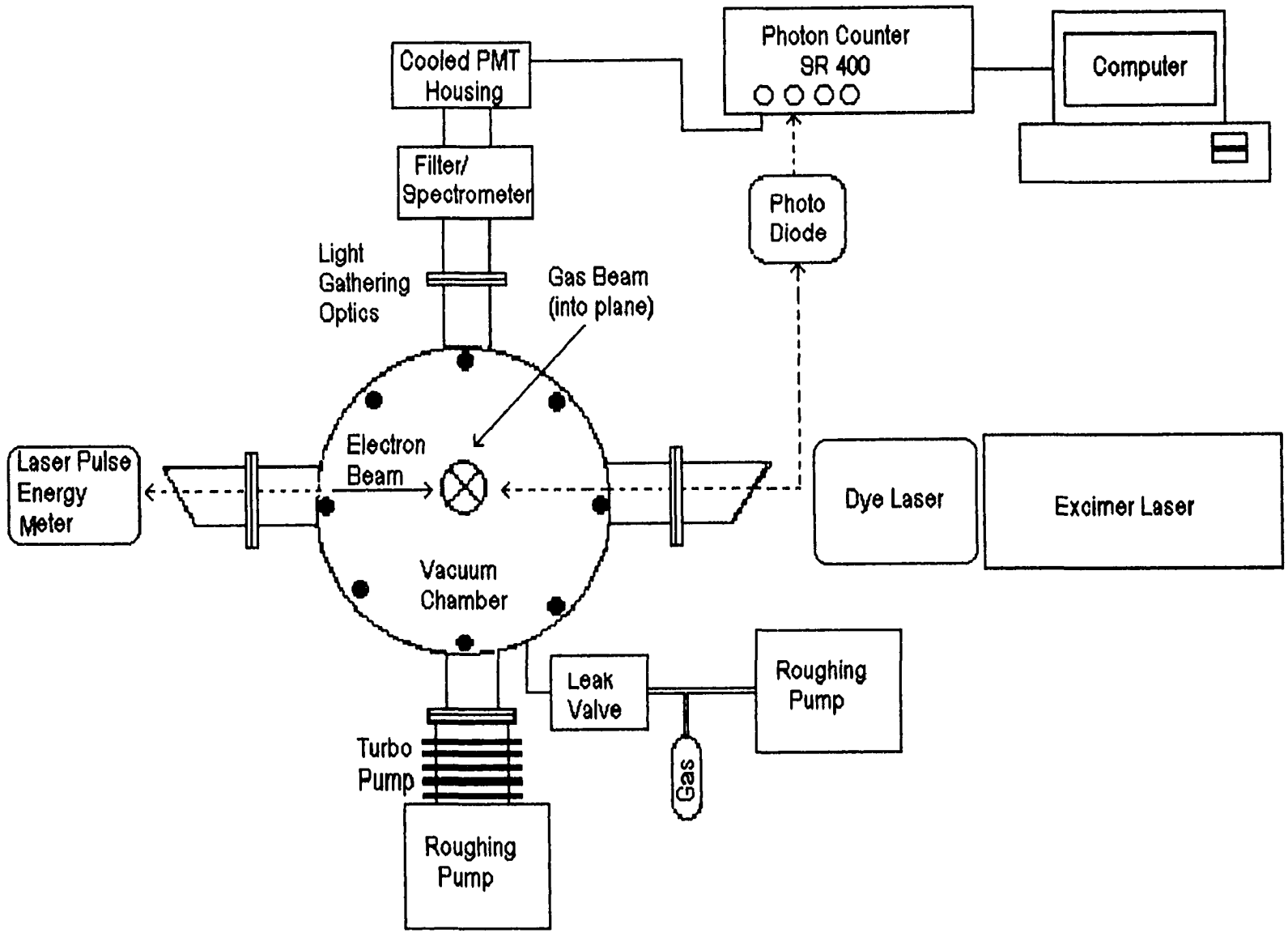

Figure (3.3.1)

3.2 The Vacuum System

The triple-beam apparatus is housed in a cylindrical stainless steel vacuum chamber which has a diameter of 6" and a height of 18". A schematic diagram (top view) of the vacuum chamber is shown in figure (3.2.1). Attached to the vacuum chamber are four ports (90° apart) in a horizontal plane . Three ports are utilized as (1) entrance port for the laser beam, (2) exit port for the laser beam, and (3) port for the optical detection. There is an additional port for the ionization gauge to monitor the pressure in the vacuum chamber. Viton O-rings are used throughout to seal the flanges. The gas beam nozzle, the electron monochromator, and the Farady cup, which is used to collect and measure the electron beam current, are mounted on a circular stage that is attached to the top flange of the vacuum chamber via a vertical shaft and a bellows assembly that allows a fine height adjustment of the crossed beam set-up. A Balzers model TSH332 turbomolecular pump station is used to evacuate the chamber. It consists of a turbomolecular pump (model TPH 330) backed by a rotary vane mechanical pump (model DUO 016B). The pumping station has a nominal pumping speed of 300 1/s for N_2 which it sufficient to achieve a base pressure (without the target gas) of approximately $2x10^{-7}$ Torr. The injection of the gas into the apparatus is controlled by a leak valve (Granville Phillips model 203) and the pressure in the gas line is monitored with a capacitance monometer (MKS model 122AA). With a pushing pressure (pressure behind the nozzle) of 0.5 Torr, the operating pressure inside the vacuum chamber is approximately $2x10^{-5}$ Torr.

Schematic of The Vacuum Chamber

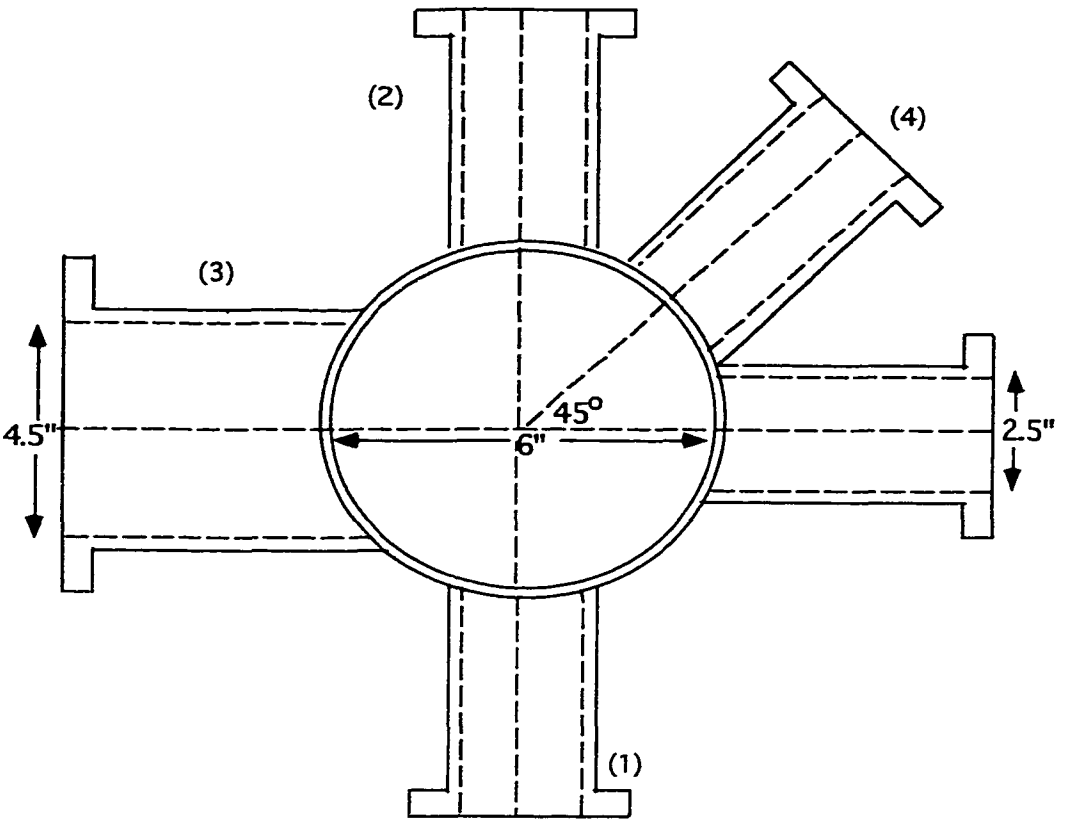

(1) entrance port for the laser beam
(2) exit port for the laser beam
(3) port for the optical detection
(4) port for the ionization gauge

Figure (3.2.1)

3.3 The Gas Beam

The target gas is admitted into the interaction region through a multicapillary array which consists of a 5x9 array of 45 individual nozzles (figure 3.3.1).

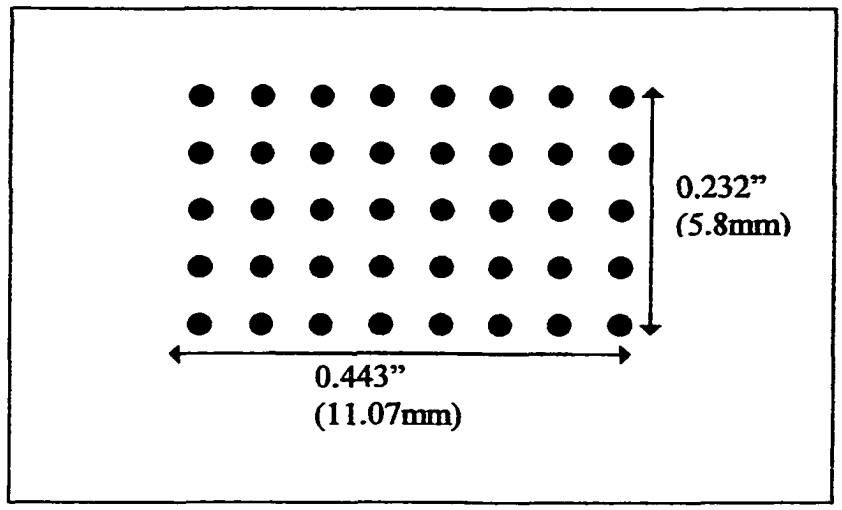

Figure (3.3.1)

Each nozzle is 0.150" (3.8mm) long and has a diameter of 0.020" (0.5mm). The separation between two adjacent nozzles is 0.032" (0.8mm).

The multicapillary array is positioned approximately 8 mm above the electron beam axis with the long axis of the array parallel to the electron beam axis. The number density of the gas molecules in the interaction region is determined by two factors:

1. the gas throughput , i.e. the total rate of gas flow through the array, and
2. the beam shape, i.e. the distribution of the gas density as a function of the polar angle with respect to the axis of individual nozzle. In order to make a quantitative estimate of the number density of N_2 molecules in the interaction region, calculations were made (Siegel 1996) utilizing a model described by Giordmane and Wang 1960. Figure (3.3.2a)

and figure (3.3.2b) (Siegel 1996) show the result of this calculation. The curves refer to the flow of N_2 molecules through the multicapillary nozzle described above. They were obtained by summing the contributions from each single nozzle over all 45 nozzles in the multicapillary array. Each figure gives the number density of N_2 molecules in units of n_0, the number density behind the nozzle, at three different heights below the array. The structure in the curves labeled "4 mm below nozzle" results from contributions from individual channels, which are still distinctly recognizable at this height, but are smeared out at heights of 8 mm and 16 mm below the nozzle. At a distance of 8 mm from the nozzle, approximately 50% of the total beam intensity lies within a rectangular region of the size of the multicapillary array. The target gas number density behind the nozzle n_0 is given by the usual ideal gas law .With $T=300^0$ and with a pressure behind the nozzle of 100 mTorr an average number density of target gas molecules of approximately $1.5x10^{12}/cm^3$ in the interaction region (8 mm downstream from the array) is obtained. Under normal operating conditions pushing pressures up to 2 Torr were used resulting in target gas number densities of up to a few times 10^{13} molecules/cm^3 in the interaction region. We note that for pushing pressures exceeding 1 Torr molecular flow conditions will no longer prevail and the conclusions from the above model calculation may no longer apply.

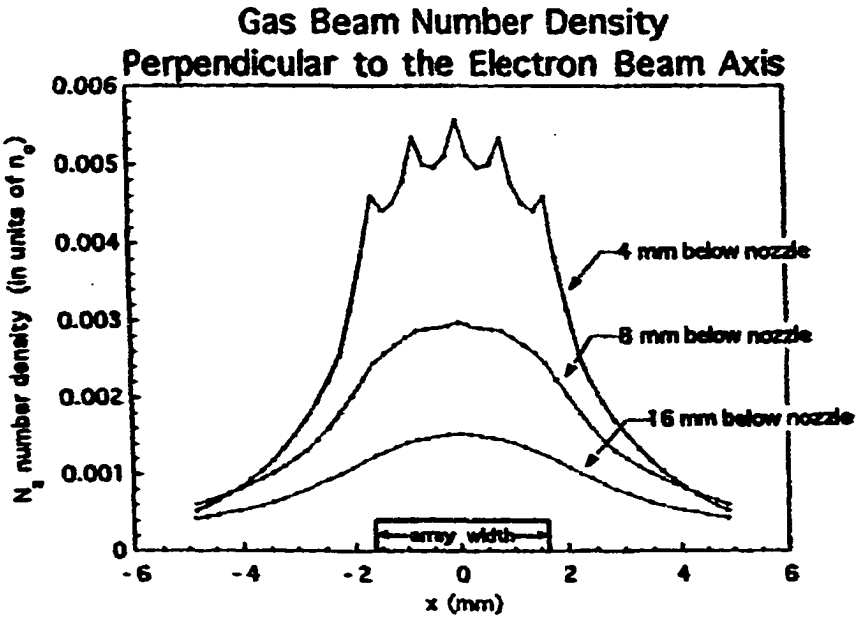

Figure 3.3.2-a

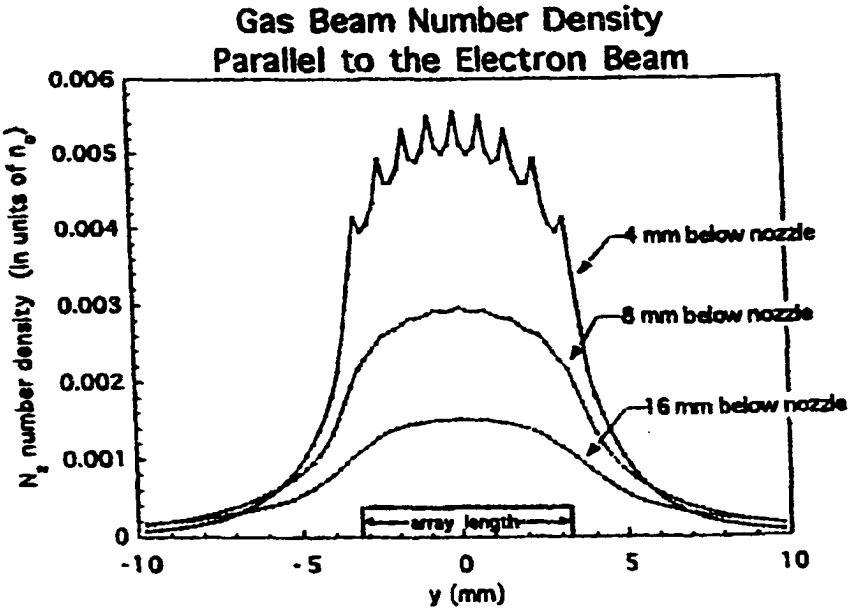

Figure 3.3.2-b

3.4 The Electron Beam

The electron beam has the following characteristics: beam energy 5-400 eV, energy spread 0.5 eV (FWHM), beam diameter in the interaction region 1-2 mm, beam current up to 10 μA at 50 eV for continuous operation. We also have the option to pulse the electron beam with beam rise and fall times about 10 ns (see section 4.2).

The electron beam is produced by an electrostatic electron monochromator which consists of:

1) a heated tungsten filament and a three element electron gun as the electron source
2) a commercially available electrostatic energy analyzer (Comstock model AC-901)
3) a three-element Einzel lens to focus the electron beam into the interaction region.

A schematic diagram of the various elements of the electron beam system are shown in figure (3.4.1).

The electron gun

A bare tungsten filament is heated to about 2000°K with a current between 2.2 A and 2.5 A causing thermionic emission (Moor et al. 1983). The filament is placed behind three stainless steel apertures (A1, A2, A3) separated by ceramic washers. These electrodes are used for extraction and collimation of the electrons.

Schematics of Electron Beam

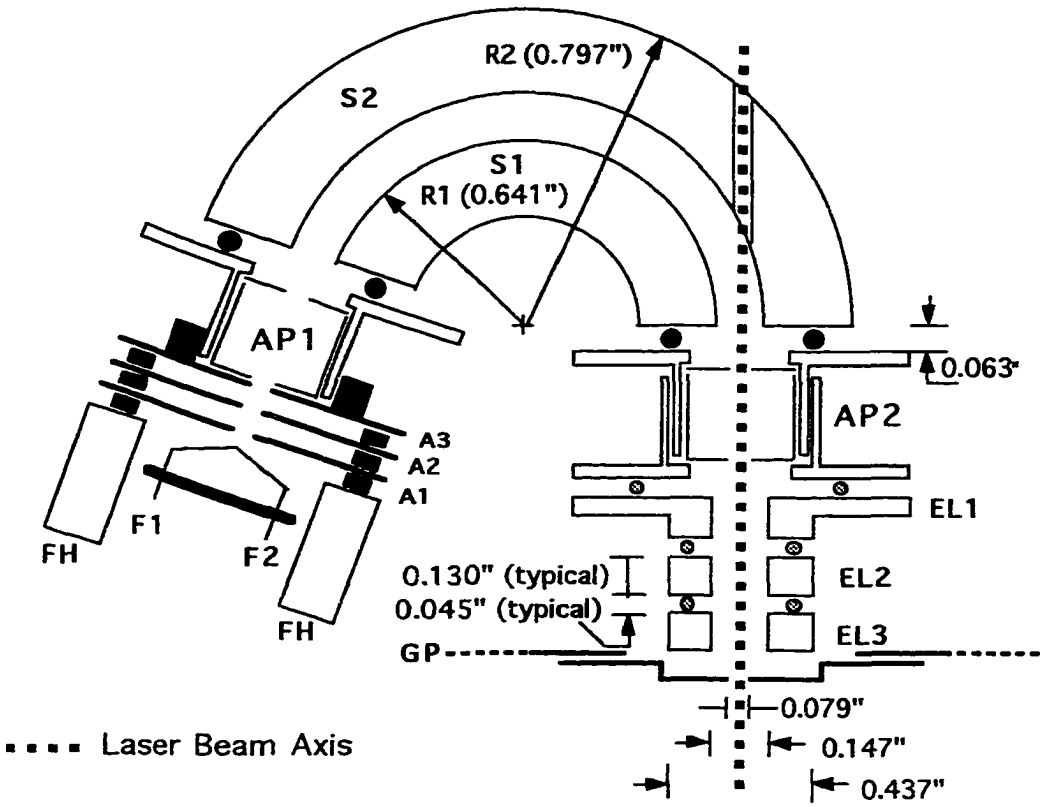

NOTES

- ⊗ 0.0625" ruby balls (used as insulating spacers)
- ● 0.09375" ruby balls (used as insulating spacers)
- ▬ 0.055" thick ceramic (or teflon) washers

AP1 & AP2 are 0.08" diameter double apertures supplied by Comstock

A1, A2 & A3 are "thin" 0.042" diameter apertures

Figure (3.4.1)

The Energy Analyzer

The energy analyzer consists of two concentric 160^0 spherical sector surfaces. The inner surface has a radius of 3.25 cm and is of convex shape and the outer surface has a radius of 4.05 cm and is of concave shape. The two surfaces, machined from oxygen-free copper, are accurately held in position about a common center and insulated from each other by ruby balls located in holes. Two copper end plates at the entrance and exit of the analyzer allow the placement of apertures (AP1,AP2) with different openings at the focal point of the analyzer. The main reason for using an energy analyzer in our experiment was to maximize the overlap between the electron beam and the laser beam by making them collinear. For this reason, the analyzer was modified by drilling a 3 mm hole in the outer sector, thus allowing the laser to pass through. In addition, we removed the input and output apertures which are normally used with the analyzer to limit the spatial spread of the electron beam and which in conjunction with the pass energy through the analyzer determine the energy resolution of the electron beam. This allowed us to increase the cross section of the electron beam, but reduced the energy resolution considerably. The energy resolution of the electron beam (0.5 eV full width half maximum - FWHM) in our mode of operation is entirely determined by the thermal energy spread of the electrons emitted by the heated tungsten filament. The analyzer without the apertures and with a high transmission energy (60V) acts merely as a bender for the electron beam, thus allowing collinear electron and laser beams.

The Einzel Lens

The Einzel lens is a three element lens system which is used to focus the electron beam from the exit of the electrostatic energy analyzer into the interaction region. A final grounded plate GP between the Einzel lens and the interaction region adds flexibility to the operation of the electron monochromator by allowing us to operate the element EL3 of the Einzel lens at a potential other then ground.

Figure (3.4.2) shows the circuit diagram for the control electronic of the electron beam system. The filament current supply floats on top of the electron energy supply. The filament housing is held at the potential supplied by the electron energy supply. The monochromator voltages A1, A2, A3/AP1/AP2, EL1, EL2, EL3, S1, and S2 float on top of the filament housing voltage. The voltages of the spherical sectors S1 and S2 float on top of AP1/AP2 potential. The potential difference between S1 and S2, ΔV (S1, S2) defines the transmission energy of the monochromator. The optimum voltages that are applied to the different elements will be discussed in section (4.1).

Collection of the Electron Beam

A customary device for measuring electron beam fluxes is a Faraday cup, which in its simplest version consists of a grounded collector electrode connected to an ammeter. In general, however, more elaborate Faraday cup designs are used to prevent or minimize the reflection of the electrons back into the interaction region and the production of secondary electrons at the collector electrode. This is typicaliy achieved by using a long cylinder, open on one side and capped on the other side, instead

Wiring of Power Supply

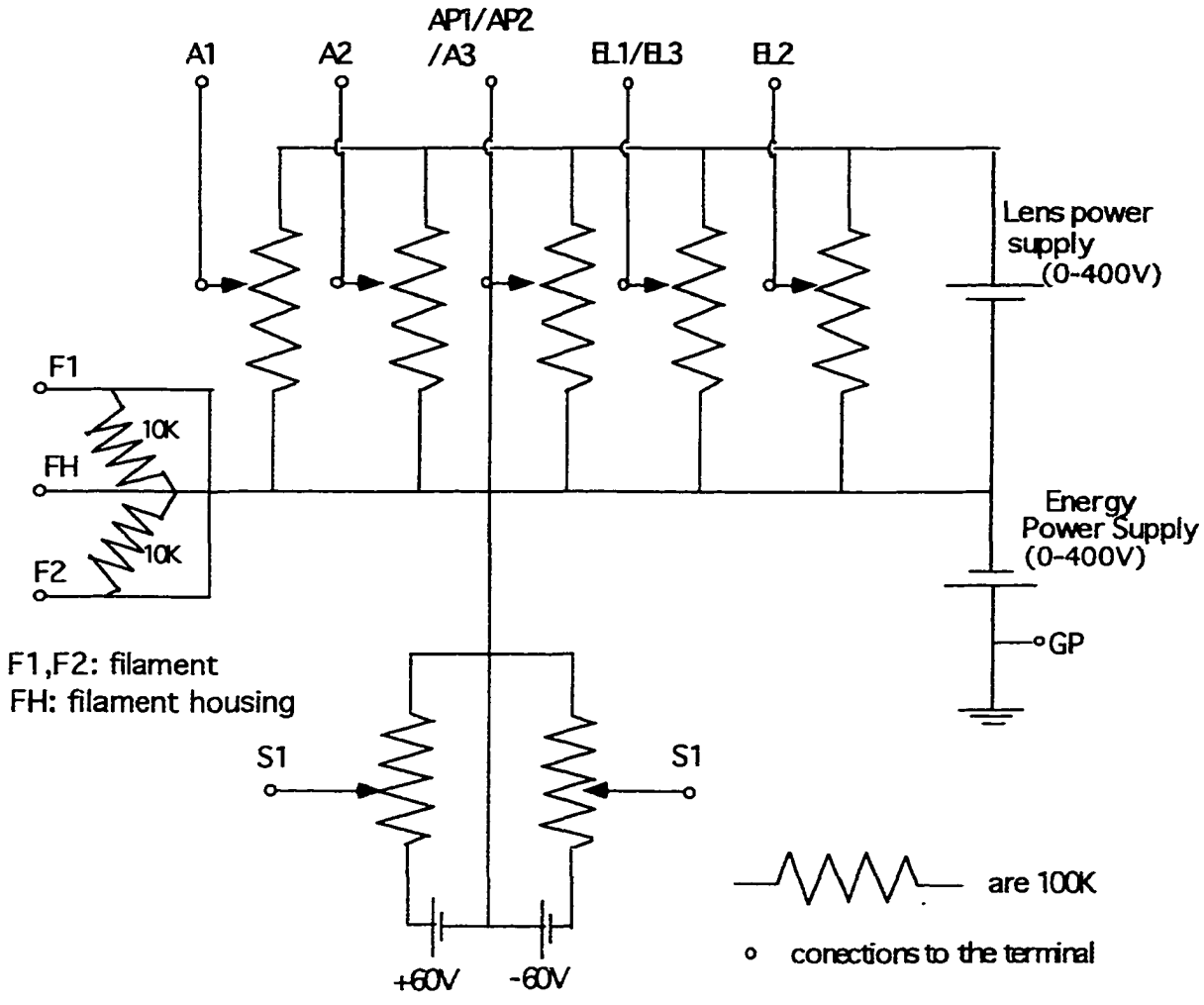

Figure (3.4.2)

of a simple flat electrode. Two or more additional cylinders are often used with one mounted inside the other and with a slight bias voltage applied to it. Any charged particles leaving the Faraday cup will give rise to an erroneous measurement of the beam current. Any electrons of appreciable kinetic energy that are reflected into the interaction region may give rise to secondary processes which may lead to erroneous contributions to the measured signal. Two basic features are commonly employed to prevent errors due to electrons ejected and reflected from the Faraday cup. First, an entrance aperture is used that subtends only small angle at the base of the cup and geometrically restrict the escape of particles. Secondly, suppression of secondary electrons is achieved with proper electrical focusing and suitable geometry. Under the best of circumstances, the errors inherent in measuring electron beam currents with a Faraday cup can be be substantially less than one percent (Thomas 1970) .

In the present experiment, the electron beam was collected in a Faraday cup which consisted of three electrically insulated elements which allowed the beam divergence as well as the total beam current to be measured. The two outer cups are coaxial cylinders with a 5 mm diameter hole in the back, to allow the laser beam to exit the cup, while the third "cup" consists of a rectangular plate mounted off- axis parallel to the electron beam axis inside the second cup and close to the exit hole. The outer Faraday cup was kept at ground potential while the inner two cups were biased positively with respect to ground, typically +9 V for the second cup and +45 V for the plate. With this arrangement, the laser was allowed to exit the Faraday cup unobstructed, while the electron beam was collected by the various elements of the Faraday cup. In addition, the bias voltages served to minimize the scattering of electrons back into interaction region

(backscattering). To minimize backscattering even further, the outer Faraday cup was approximately three inches deep, which had the additional effect of preventing field penetration into the interaction region. (see figure 3.4.3).

The electron analyzer and the Faraday cup were mounted on a circular stage attached to the top flange of the vacuum chamber. The height of the stage could be varied. Those components of the electron spectrometer which were exposed to electrons were coated with Aerodag-G (Acheson Colloids Company). Aerodag is a colloidal graphite dissolved in isopropyl alcohol. A coating of Aerodag G reduces the yield of elastically reflected electrons as well as the formation of secondary electrons and it produces comparatively uniform surface potentials. The components of the electron spectrometer which might be exposed to direct laser light or scattered laser light were coated with Aerodag as well in order to absorb the some of laser light.

Faraday Cup

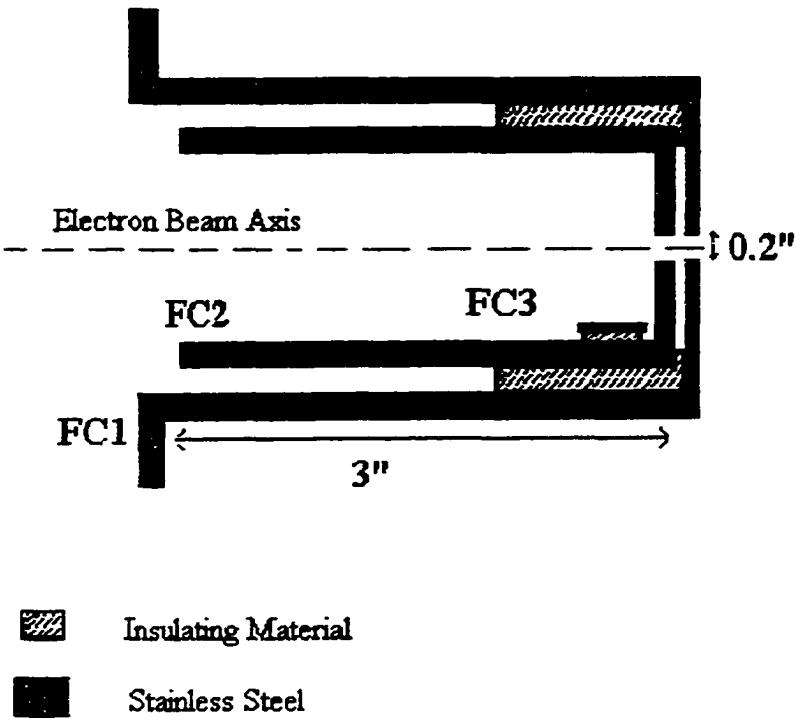

Figure (3.4.3)

3.5 Laser Beam System

The laser system consists of an Excimer laser (Lumonics Ex-520) which is used to pump a dye laser (Lumonics HD-500) . The Xe, HCl , He, Ne gas required for the Ex-520 were obtained commercially (Spectra Gases) in the quantities and purities specified by Lumonics. The dye for the HD-500 Excalite 392A, was obtained from Exciton .

The Excimer Laser

A detailed description of the excimer laser was already given in the previous thesis (Siegel 1996) and only a brief discussion will be given here. The operating principle of an excimer laser is as follows. An inert gas atom and a halogen gas atom form a short lived complex, called an excimer, in a pulsed electrical discharge. The excimer is formed in an excited state which dissociates upon decay, thus creating the needed population inversion. The excimer molecules are contained in a discharge vessel where the lasing takes place. A plane mirror at the back of the vessel and a quartz flat at the front of the vessel, both aligned perpendicularly to the laser beam axis, form the resonant cavity. The quartz flat, with a reflectivity of less than 5% , serves as the output coupler. The output is pulsed with the pulse length determined by the lifetime of the excimer complex.

The feed gases used in our laser were Xe and HCl , forming the XeCl excimer that lases at 308 nm . Typical excimer laser output specification are given in table (3.5.1) below.

Excimer laser out put specifications:	
Excimer	XeCl
Wavelength	308 nm
Pulse duration	8-10 ns
Pulse energy	80-100 mJ
Repetition rate	20-100 HZ
Average power	4-10 Watts

Table (3.5.1)

The Dye Laser

A dye laser consists of an active medium, usually an organic dye molecule dissolved in an appropriate solvent, which is placed in an optical cavity. The dye is activated (pumped) by another laser. The pump process leads to a population inversion in which the majority of the dye molecules are raised to an excited state. The active medium then emits coherent light through stimulated emission. For the work carried out as part of the present thesis we employed a new dye laser, a model HD-500 from Lumonics. In the HD-500, a diffraction grating serves both as a reflector and as the dispersing element, which restricts the laser gain to a narrow bandwidth. A beam expander is used to ensure that the grating is filled which improves the spectral resolution of the laser beam. Tunability is achieved by rotating the grating. The HD-500 is designed in an oscillator/amplifier configuration to provide narrow linewidth and high conversion efficiency. The oscillator employs a prism beam expander and a near-grazing incident

grating to achieve high resolution while maintaining useful efficiency. The dye laser system is comprised of the oscillator/amplifier dye beam optical path, a suitable set of pump beam optics, a dye recirculation system, and a wavelength scan control unit with remote keypad control .

A schematic diagram of the dye laser is shown in figure (3.5.1). The pump beam enters from port 1 in our experiment. A portion of the pump beam is reflected from the mirror M1 into the oscillator dye cell, while the remainder of the beam is directed by the mirrors M2, M3 and M4 into the amplifier cell. The dye laser beam exits through port 2.

Typical dye laser output specification are given in table (3.5.2) below.

The Dye Laser Specifications	
Direct tuning range	XeCl pump: 320-950 nm
Tuning range using Excalite (392A)	373-397 nm
Repetition rate	up to 500 pps
Line width	0.0015 nm

Table (3.5.2)

The laser beam intensity is monitored by a laser pulse energy meter (LASER PROBE RM-3700) We obtained a typical pulse energy of 3mJ/pulse.

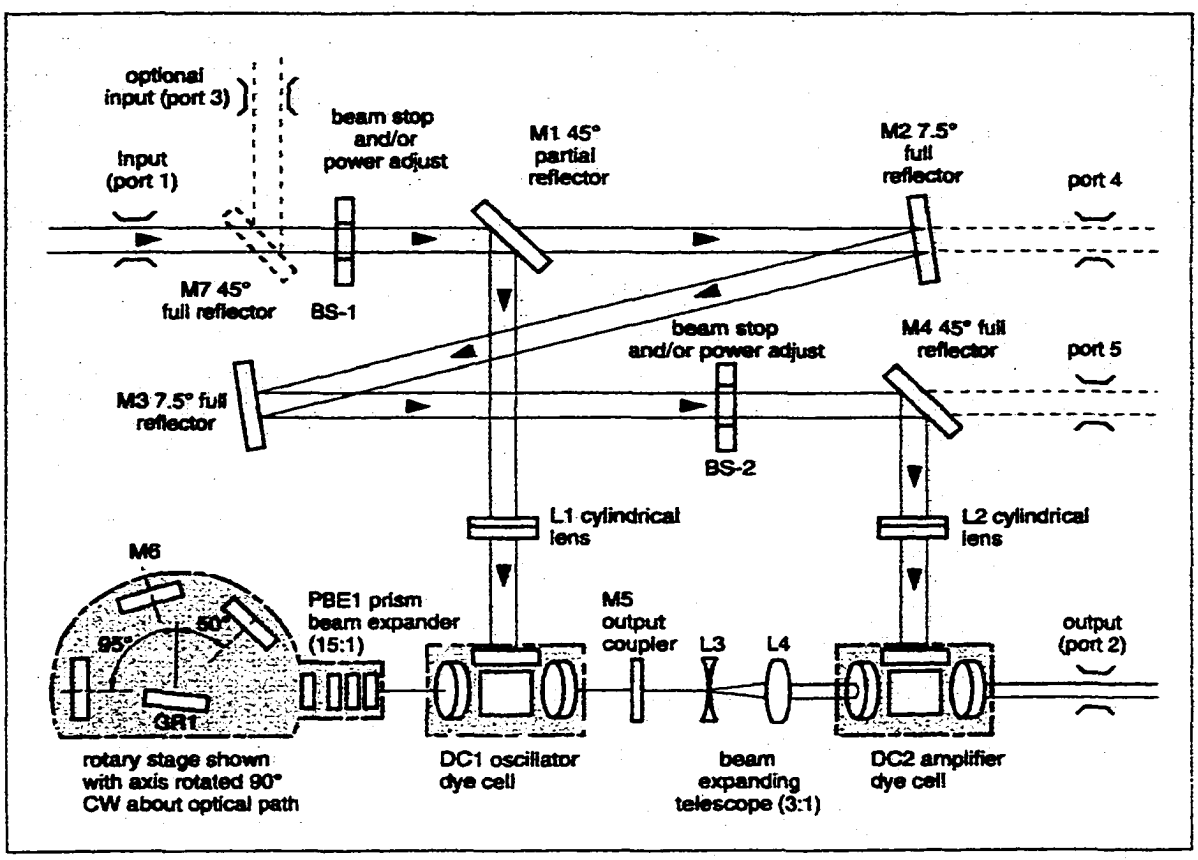

Figure (3.5.1) schematic diagram of the SpectrumMaster lasers showing input ports for the pump beam (ports 1 or 3), the pump beam path, possible pump beam exit ports (ports 4 and 5), and the dye beam output port (port 2).

Laser beam spectrum

Figure (3.5.2) shows a wavelength scan of the HD 500 dye laser. This scan was obtained by using an optical spectrometer (SPEX model 500M , 0.5 meter spectrometer) and a liquid N_2 cooled PMT (Hammamatsu model R1104). A minimum resolution of 0.1 Å (FWHM) was obtained with the narrowest slits (10μ) and by using the spectrometer in second order. In the scan shown in figure (3.5.2), the monochromator was kept at a fixed wavelength and the laser was scanned over a wavelength range of 0.4 nm (4Å). The narrow peak structure around the maximum makes it possible to determine the wavelength precisely. The measured 0.1 Å (FWHM) linewidth represents the minimum resolution of the spectrometer and not the true linewidth of the laser, which is 0.015Å according to the manufacturer's specification.

The wavelength control of the dye laser

Figure (3.5.3) provides a schematic diagram of the components of the wavelength scan controller of the HD-500. The main electronics are located in a separate box and include the power supply , the user interface I/O board, the CPU, the encoder board, and up to three boards to drive stepper motors. The I/O board has connections to the keypad, a built-in RS232 interface for the host computer option, and a trigger output to the pump laser. The CPU board has a microprocessor to run the unit. The stepper drive cards contain sophisticated electronics for a high resolution (500 steps/rev) stepper motor and then group these "microsteps" into "ministeps" for improved linearity of the motion. The resultant resolution is 7×10^{-6} degrees per step, which corresponds to 20 steps per

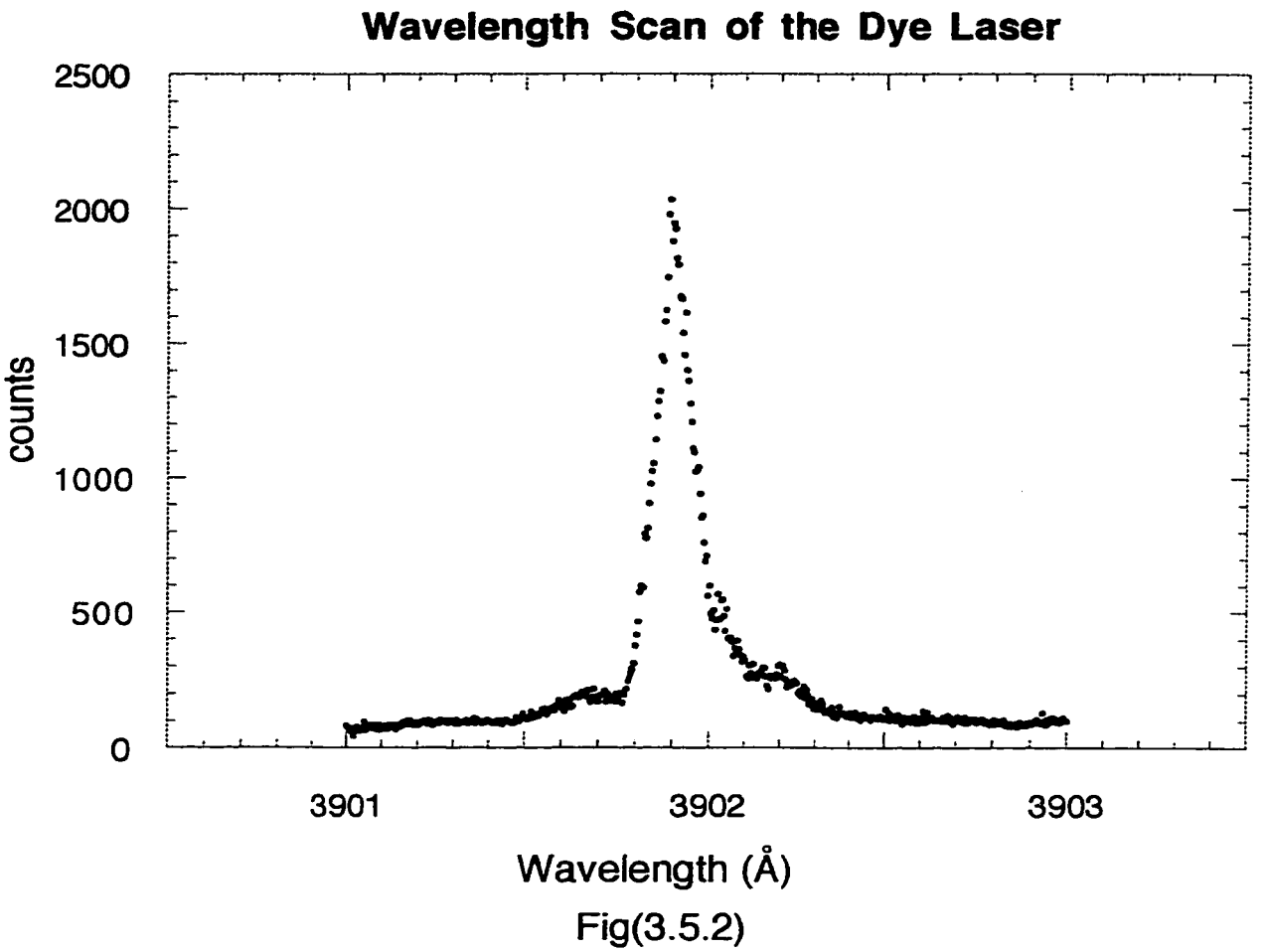

Fig(3.5.2)

unit linewidth . The scan unit has the capability to control up to three stepper motors. We are using one motor for the wavelength drive. The scan unit can also be used as a trigger for the excimer laser . For each trigger pulse the excimer laser will fire once.

Scan Unit Control

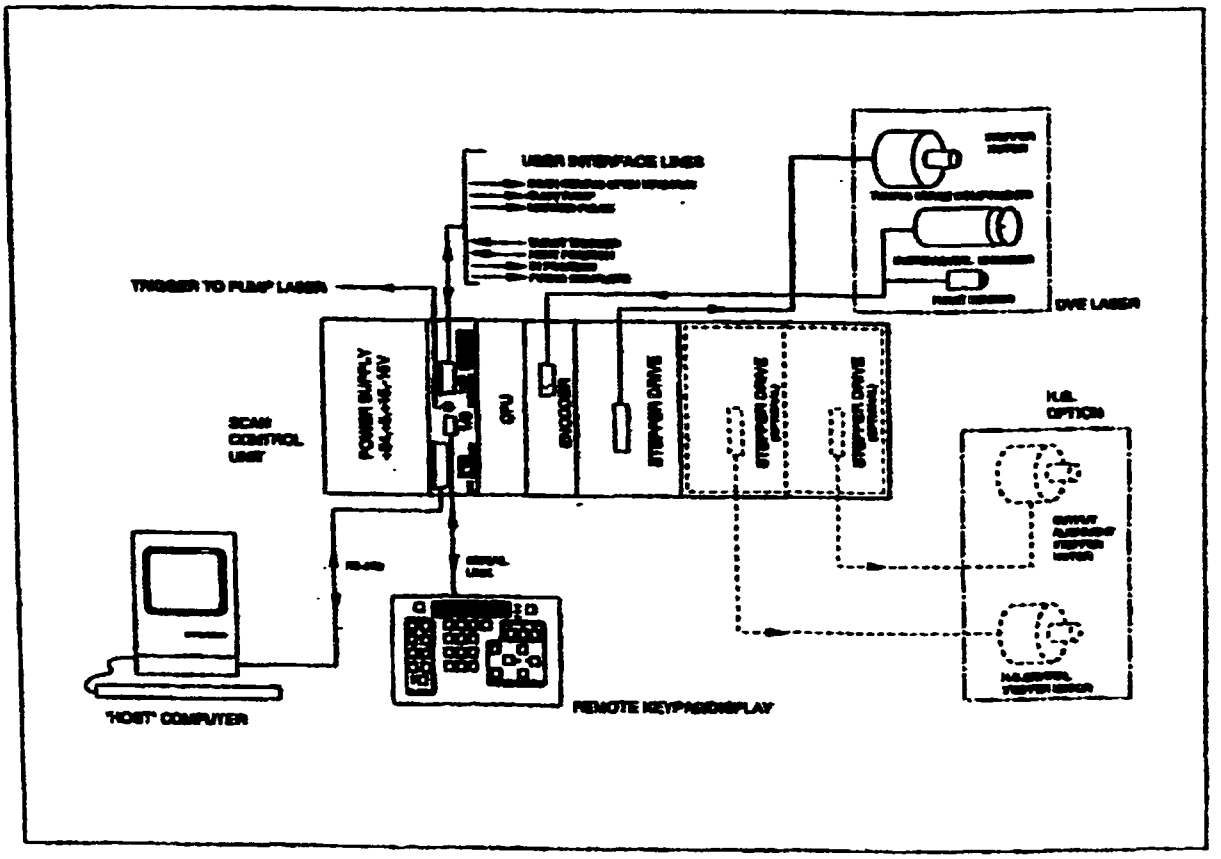

Figure 3.5.3

3.6 The Light Detection System

The light detection system was designed to maximize the collection and transport of radiation originating in the interaction region to the photon detector while minimizing the amount of scattered laser light that reaches the detector. The basic detection system consists of 4 components (1) the optical system to collect as much of the light emitted from the collision region as possible, (2) a filter or monochromator to separate the spectral line of interest from all the other emissions, (3) a cooled photomultiplier tube for the photon detection, and (4) a data acquisition system.

The light collection system

The light collection system consists of an aperture and a primary lens that are located inside the vacuum chamber. A window serves as a vacuum-to-atmosphere seal and a secondary lens outside the vacuum system completes the collection optics. Both lenses are plano-convex. The primary lens has a focal length of 50 mm and a diameter of 40 mm and the secondary lens has focal length of 75 mm and a diameter of 50 mm. For extended transmission into the UV, the lenses and the window are made from uncoated synthetic silica (Melles Griot) All optical components located outside the vacuum system including the detector are placed inside a telescopic aluminum tube to prevent stray light from entering the light collection system.

Spectral isolation

Spectral isolation is achieved by either i) an interference filter or ii) a monochromator.

i) the interference filter (Andover Corporation) with a band pass of 10 nm FWHM and a transmission of 40% is used to select a single vibrational band for detection, in the present case the $N_2^+(B^2\Sigma_u^+ \rightarrow X^2\Sigma_g^+)$ (0,1) band at 428 nm.

ii) A model H-20 Instruments S.A. monochromator can be used instead of the filter. Some specification of the monochromator are given in table (3.6.1).

The monochromator is compact and provides high throughput at a reasonably good spectral resolution. The monochromator is equipped with an aberration- corrected holographic grating. This grating replaces three optical elements in traditional monochromator designs, light collection, diffraction, and aberration-corrected focusing.

Monochromator Specification	
Focal length	200 mm.
Aperture	f/4.2
Grating	40x45 mm aberration corrected holographic grating.
Bandpass	2,4 or 8 nm with 0.5, 1 or 2 mm slits
Resolution	0.4 nm with 0.1 mm slits
Stray light level	10^{-5} at 8 nm from 632.8 nm laser light.
Size	339 mm x 84 mm.

Table (3.6.1)

The monochromator is equipped with several sets of slit inserts and height-limiting apertures are provided at the entrance and exit slits, We normally use 4 mm x 8 mm slits to allow maximum signal throughput. The resolution obtained under those condition is 16 nm (FWHM).

The photon detector

The photomultiplier tube (PMT) is a Hammamatsu R1104 photomultiplier tube. The PMT is placed inside a thermoelectrically cooled housing which keeps it at a temperature of -40^0 C. The PMT was chosen to have a high detection efficiency in the UV. The quantum efficiency of the photocathode, i.e. the ratio of incident photons to ejected photoelectrons, is 18.5% at 428 nm (Hamamatsu Corp., 1985).

Data acquisition

Time resolved fluorescence studies were made possible by the use of a Stanford Research model SR400 gated photon counter which counts the pulses from the PMT that arrive within specified time window, or gate. The Stanford Research model SR400 gated photon counter consists of an internal 200 MHZ clock and three independent counting units, each consisting of an amplifier, a discriminator, a gate, and a counter. The SR400 was programmed to open a gate at a predetermined time after receiving a start pulse or alternatively each gate could be held open continuously (CW). The trigger pulse can come from the internal clock or from an external source. The time between the trigger pulse and the opening of the gate , the gate delay, was fixed or could be

scanned. Additionally, the gate width could be varied . The minimum gate width is 5 ns and the minimum gate delay is 25 ns. During a data run each scanned parameter was incremented after a predetermined number of trigger pulses, the counting period, and a data point consisted of the number of PMT pulses received during one counting period . In the present experiment, the SR400 was programmed to open a gate after receiving a trigger pulse from a photodiode which was used to monitor (a small part of) the dye laser beam.

Chapter 4. Experimental Procedure

4.1 Operation of the Electron Monochromator

The energy of the incident electron beam E (5-400 eV) is essentially determined by the voltage difference ΔV between the filament tip (and filament housing) and ground potential. The final element of the electron gun, the interaction region, and the outermost Faraday cup are all held at ground potential, so that the interaction region is field free. The transmission energy of the electrons through the monochromator/bender is determined by the fact that a singly charged particle of energy K is transmitted between two concentric spheres of radi r_1 and r_2, if the potential difference, ΔV_r, between the spheres satisfies the relation

$$K=\frac{\Delta V_r}{r1/r2 - r2/r1} \qquad (4.1.1)$$

For $r_1 = 4.05$ cm and $r_2=3.25$cm we find $K= 2.254\ \Delta V_r$. This establishes the relation between transmission energy K and potential difference ΔV_r. The optimum voltages for the various other elements of the electron gun, monochromator, and Einzel lens are determined empirically by optimizing the electron beam current and the photon signal that arises from the electron impact excited $N_2^+(B\rightarrow X)$ emission. In general, the energy E of the electrons is not identical to the voltage difference applied between the tip of the

filament and the grounded interaction region ΔV . Contact potentials, i.e. potential differences between junctions of dissimilar metals due to a difference in the Fermi levels of the materials (Eisberg and Resnick 1985) can account for a difference between E and ΔV of typically a few electronvolts. Dielectric films (from pump oil and other hydrocarbon contamination) deposited on elements of the electron monochromator and electrostatic lenses can accumulate electric charge following electron impact. This can significantly alter the potentials "seen" by the electron and may result in energy shifts of 10 eV or more (Gilbert et al. 1990). The energy shift caused by charged dielectric films can change with time and with the magnitude of the electron beam current. The energy shift (often generally referred to as "contact potential") δ can be determined experimentally from the difference between the measured threshold for production of an optical emission feature from a particular target and the known energy for this emission determined from spectroscopic and thermochemical considerations . In the current experiment, the electron impact ionization/excitation of N_2 to produce the N_2^+ emission at 428 nm was used to determine the contact potential. Figure (4.1.1) shows the measured onset region of the N_2^+ 428 nm emission cross section . The measured onset in comparison with the well known minimum energy (19 eV) is used to calibrate the electron energy. The onset in figure (4.1.1) is determined to be 32.3 eV from the extrapolation of the photon yield curve. This yields a contact potential of 13.3 eV which as mentioned above is probably largely due to insulating films on the various elements of the electron beam system.

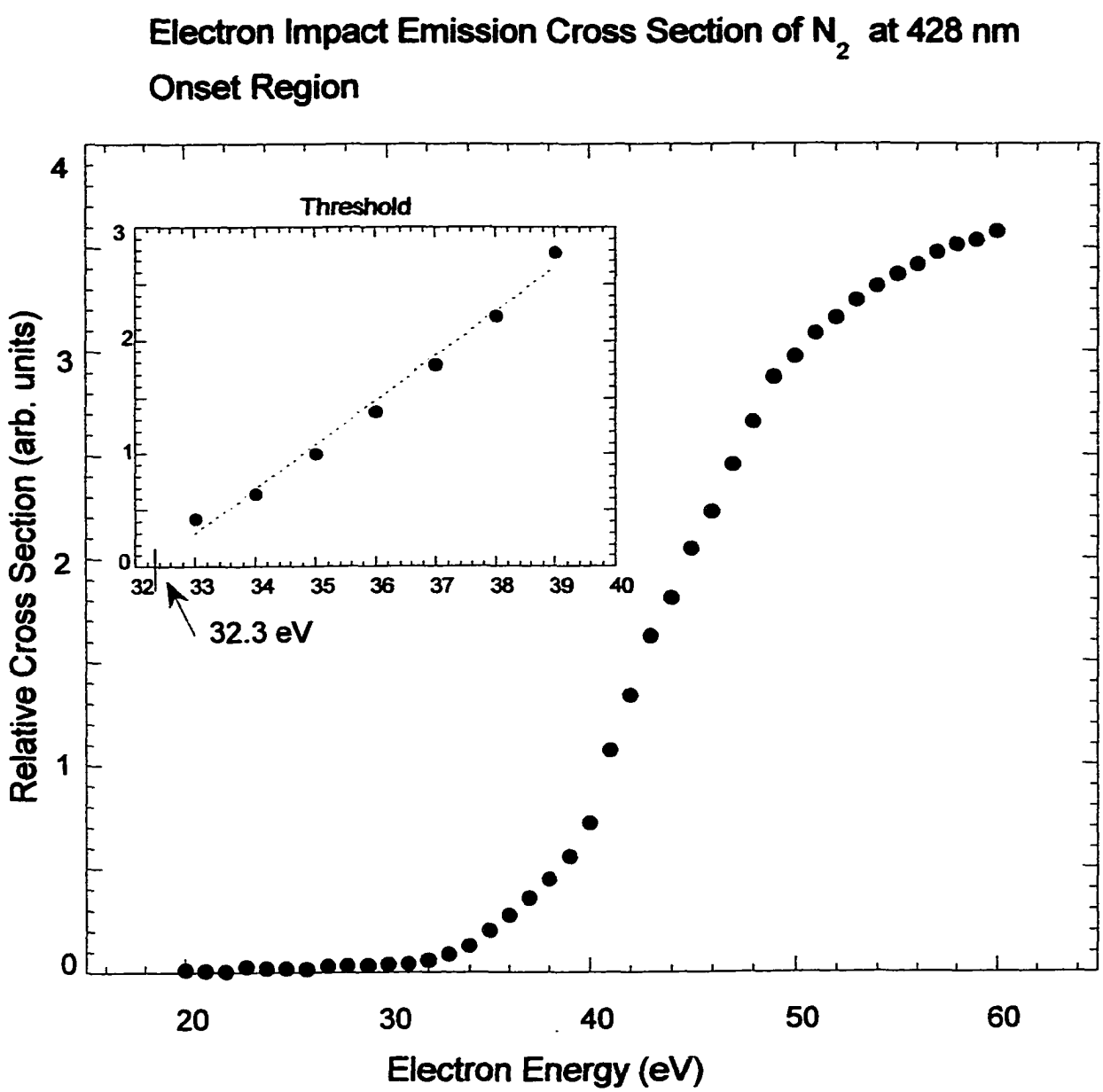

Figure (4.1.1)

4.2 Pulsed Electron Beam Operation

Pulsing of the electron beam was accomplished by applying a voltage to the lens element EL_3 which is more negative then the voltage applied to the filament tip. A pulse generator, HP model 214A, was used for that purpose which generated pulses with a fall time of less then 10 ns. We used the wavelength scan control of the dye laser as the master trigger for the excimer laser and the HP214A pulse generator. In order to test the pulsed electron gun, we monitored the time-resolved fluorescence signal from the electron-impact excited N_2^+ molecules. The time resolved intensity shown in Figure (4.2.1) was obtained using the SR400 gated photon counter with a 5 ns gate width that was incremented every 5 ns. Each data point represents data accumulated for 5 s. The time resolved fluorescence clearly shows 3 regions, electron beam on (region 1 and 3) and electron beam off (region 2). The fall time of the electron beam is 70 ns (corresponding to the life time of the excited N_2^+ molecules convoluted with the fall time of the pulse generator). It is important that the fall time is below 0.5 μs which is the time it takes the N_2^+ molecules to leave the interaction region. In region 2, the electron beam was turned off for about 300 ns which is about 5 times the radiative lifetime of $N_2^+(B)$ state. This will be discussed in more detail in section 5.1.

Time Resolved Fluorescence Signal from the Electron Impact Excited N_2^+ Molecules Using a Pulsed Electron Gun

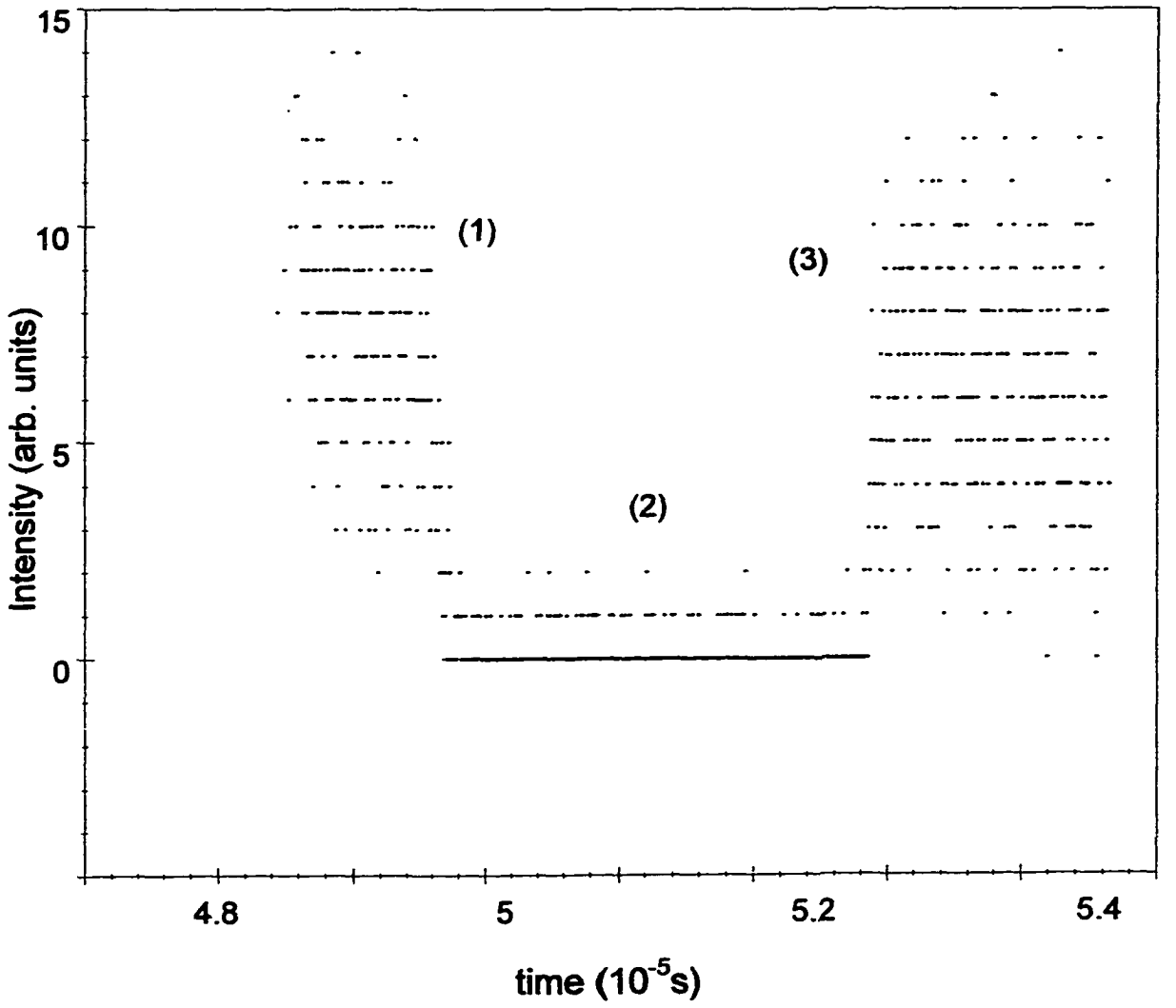

Figure (4.2.1)

4.3 Operation of the Laser System

In order to facilitate the detection of the LIF signal in our experiment , all experimental parameters of the laser system have to be optimized. The pulse energy has to be high, the scattered laser light has to be suppressed, and the control of the wavelength of the laser has to be accurate and reproducible .

1) Control of the Wavelength of the Laser

The dye laser incorporates a precision rotary tuning mechanism for control of the output wavelength. This rotary stage is driven by a stepping motor, which, in turn, is controlled by an electronic scan unit (SCU). The wavelength emitted by the dye laser is governed by the equation:

$$n\lambda = d(\sin\theta + \sin\phi) \qquad . \qquad (4.3.1)$$

Here λ is the wavelength

d is the spacing of the grooves of the grating (usually 417 or 555 nm)

ϕ is the angle of diffraction, and

θ is the angle of incidence (fixed near 86^0)

n is the order of diffraction (usually first or second order)

Since for a given configuration, the spacing of the grooves, the angle of incidence, and the order of diffraction are constant, the output wavelength is a simple sine function of

the angle of diffraction of the light coming from the grating. The precision rotary stage controls the angle of a tuning mirror, and a built-in microprocessor computes the wavelength. We are using the dye laser in the so-called BRUST mode. Instead of the wavelength changing linearly with time, the wavelength changes by fixed increments between the START POSITION and the END POSITION.

2) Scattered Laser Light

The proper alignment of the dye laser beam through the vacuum is crucial, since even a slightly misaligned laser causes significant scattered laser light which then "blinds" the PMT (see discussion below) The laser pulse was guided into the vacuum chamber by a system of three mirrors and several apertures (typically three). Initially, the output pulse from the dye laser is vertically polarized, but because the mirror arrangement rotates the plane of polarization, the laser pulse entering the vacuum chamber is linearly polarized horizontally. Examination of the laser spot on a blank sheet of white paper as it emerges from the vacuum chamber served an initial, visual test of the laser beam alignment. PMT blinding is caused by a brief, intense burst of incident light on the cathode of the PMT, which "overloads" the PMT. As a consequence, the PMT is unable to generate output pulses for a subsequent period of time (recovery time). The most common cause of PMT blinding is intense laser light scattered by any object inside the vacuum chamber. Even when the scattered laser light is not intense enough to cause PMT blinding, it can still obstruct the LIF signal by burying it in a large background. Therefore, it was essential to measure and minimize the amount of scattered laser light per laser pulse and to determine the time required for the scattered laser light signal to decay. We developed an

experimental procedure that ensured that these two parameters were always minimized. We will describe this procedure for two scenarios,

1) Laser pumping and LIF detection at different wavelengths.

2) Laser Pumping and LIF detection at the same wavelength .

Pumping and detecting at different wavelengths

Both entrance and exit windows for the laser beam are Brewster angle windows. Optical baffles consisting of hollow pipes whose inner surfaces were coated with Aerodag guide the laser light from the entrance window to the electron monochromator and from the Faraday cup to the exit window. Figure (4.3.1) below illustrates the effect of PMT blinding. The time-resolved laser pulse as seen by the PMT was obtained using the SR400 with a 5 ns gate width that was incremented by 5 ns after every 100 laser pulses. We take t=0 to be the time at which the SR400 receives a trigger pulse from the photodiode. It takes the laser pulse 40 ns to arrive into the interaction region. This delay is mostly due to electrical delay in the circuit. Two features are apparent in figure (4.3.1) The first feature is a peak generated by the incident laser pulse.The second feature is a tail whose magnitude and position indicates how long the PMT was blinded .We see in figure (4.3.1) a period of time where no pulses were counted (from 60 ns to 70 ns). This period of time, the "dead time" is the consequence of "PMT blinding". After the PMT "recovers", 30 ns after the laser peak there are still 26 counts resulting from the scattered laser light . The 26 counts represent the area under the intensity curve from 70 ns to 160 ns. Figure (4.3.2) illustrates a situation where no PMT blinding occurs. There is no "dead time" and there are only 7 counts in the time interval from 70 ns to 150 ns (i.e. 30 ns after the laser peak).

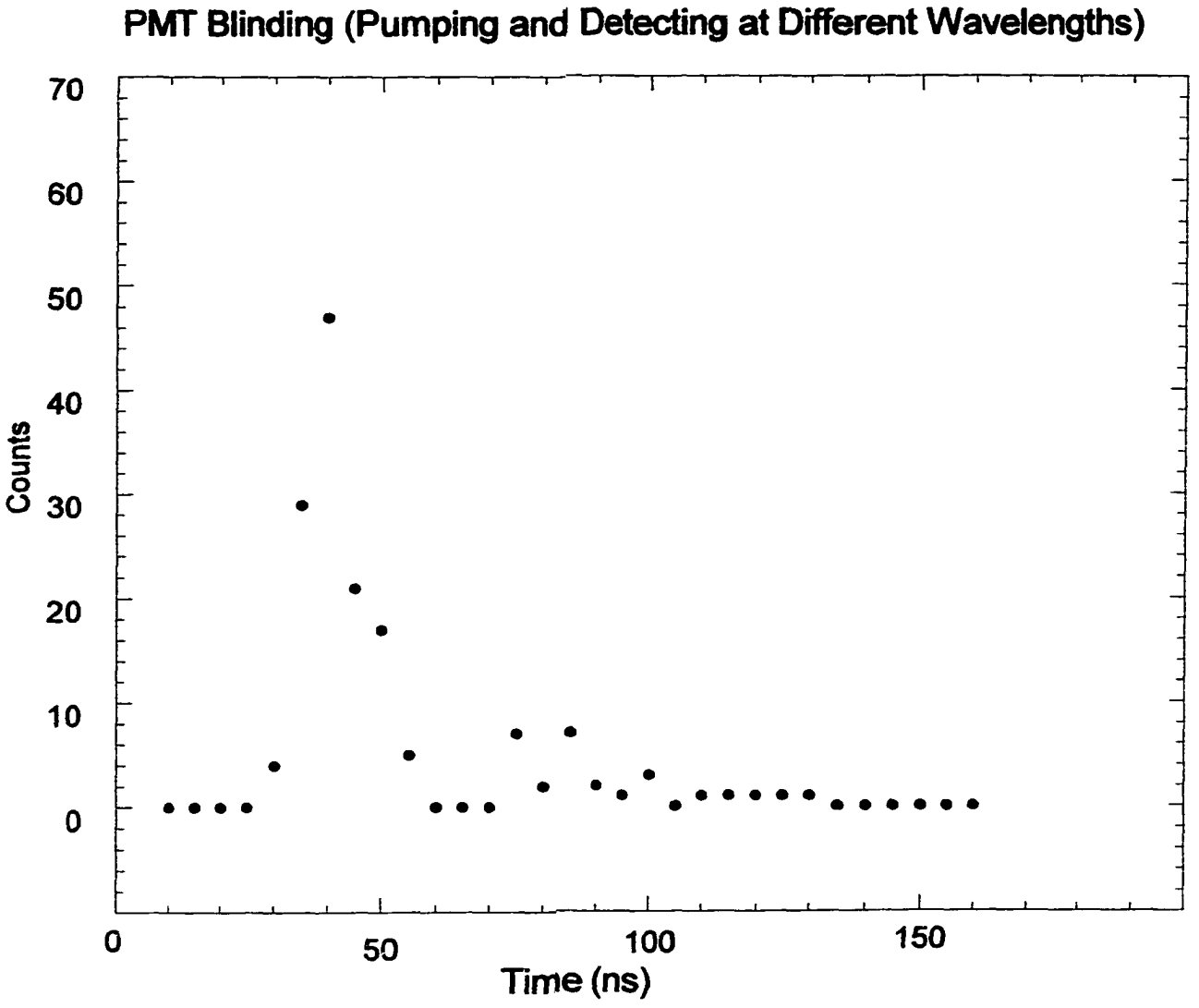

Figure (4.3.1)

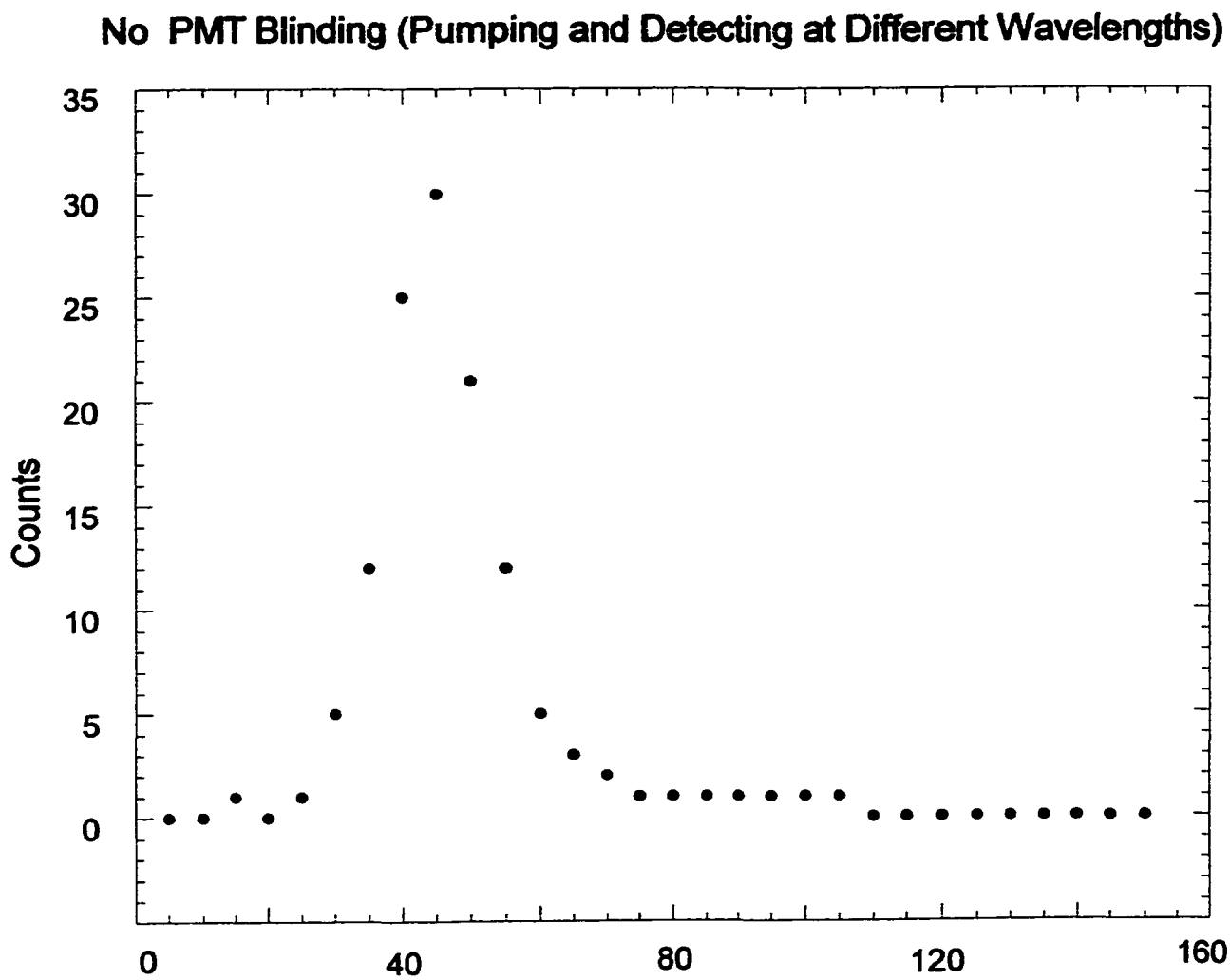

Figure (4.3.2)

Pumping and detecting at the same wavelength

Blinding of the PMT is a much more serious issue when trying to probe and detect at the same wavelength. Serious blinding of the PMT occurred under these circumstances, even when using an empty vacuum chamber and using neutral density filters in the light pass to attenuate the incident laser power. In order to solve this problem, we had to make a number of modifications to the experiment.

First we replaced the 390 nm interference filter with a monochromator (Instrument SA model H-20). The data in figures 4.3.3 and 4.3.4 show the scattered laser light signal taken with a laser pulse energy 25 μJ and entrance and exit slits of 2 mm width and 8 mm height. Figure (4.3.3) is taken with an empty vacuum chamber while figure (4.3.4) is taken with the electron monochromator / Faraday cup assembly inside the chamber. With an empty vacuum chamber we detected 16 counts from scattered laser light 30 ns after the laser peak (i.e. in the time interval from 65 ns to 250 ns there are 16 counts attributed to scattered laser light). With the electron monochromator / Farady cup assembly inside we detected 30 counts from scattered laser light during the same time interval. This is comparable with the excpected LIF signal and, therefore, constitutes an unacceptably high level of scattered laser light. As a consequence, additional steps had to be taken. We inserted a baffled light path along the direction of observation which restricted the light collection to light directly from the interaction region. Figure (4.3.5) shows the scattered laser light signal with the monochromator assembly in the vacuum chamber using 60 μJ laser pulse energy and the same slit size as before (figures 4.3.3 and 4.3.4). 30 ns after the laser pulse, the scattered laser light was reduced to 8 counts in the time interval beyond 70 ns. This represents an acceptable

Scattered Laser Light (Pumping and Detecting at the Same Wavelength)
No Assembly in the Chamber and 2x8 mm Slits in the Spectrometer

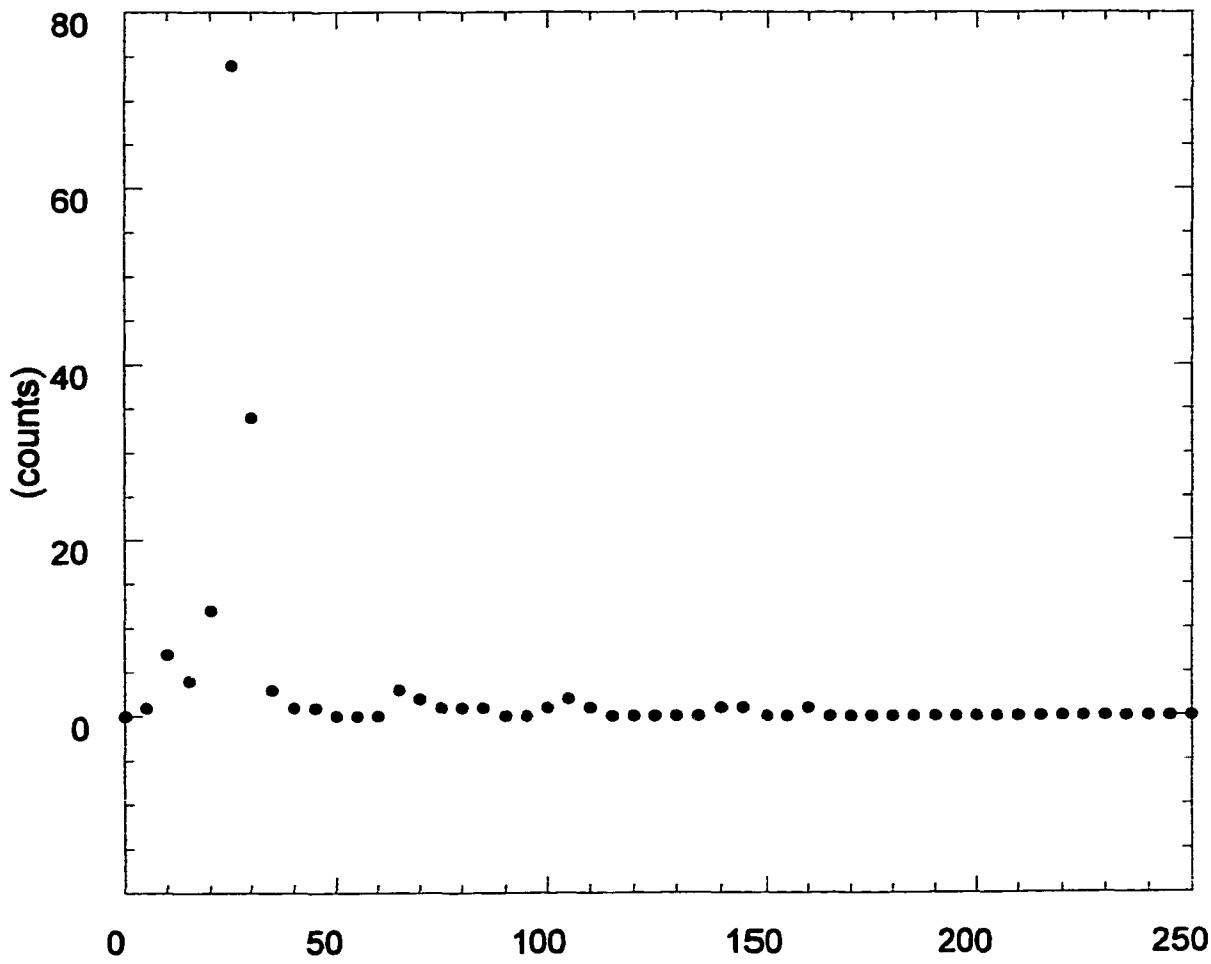

Figure (4.3.3)

Scattered Laser Light (Pumping and Detecting at the Same Wavelength) Assembly in the Chamber and 2x8 mm Slits in the Spectrometer

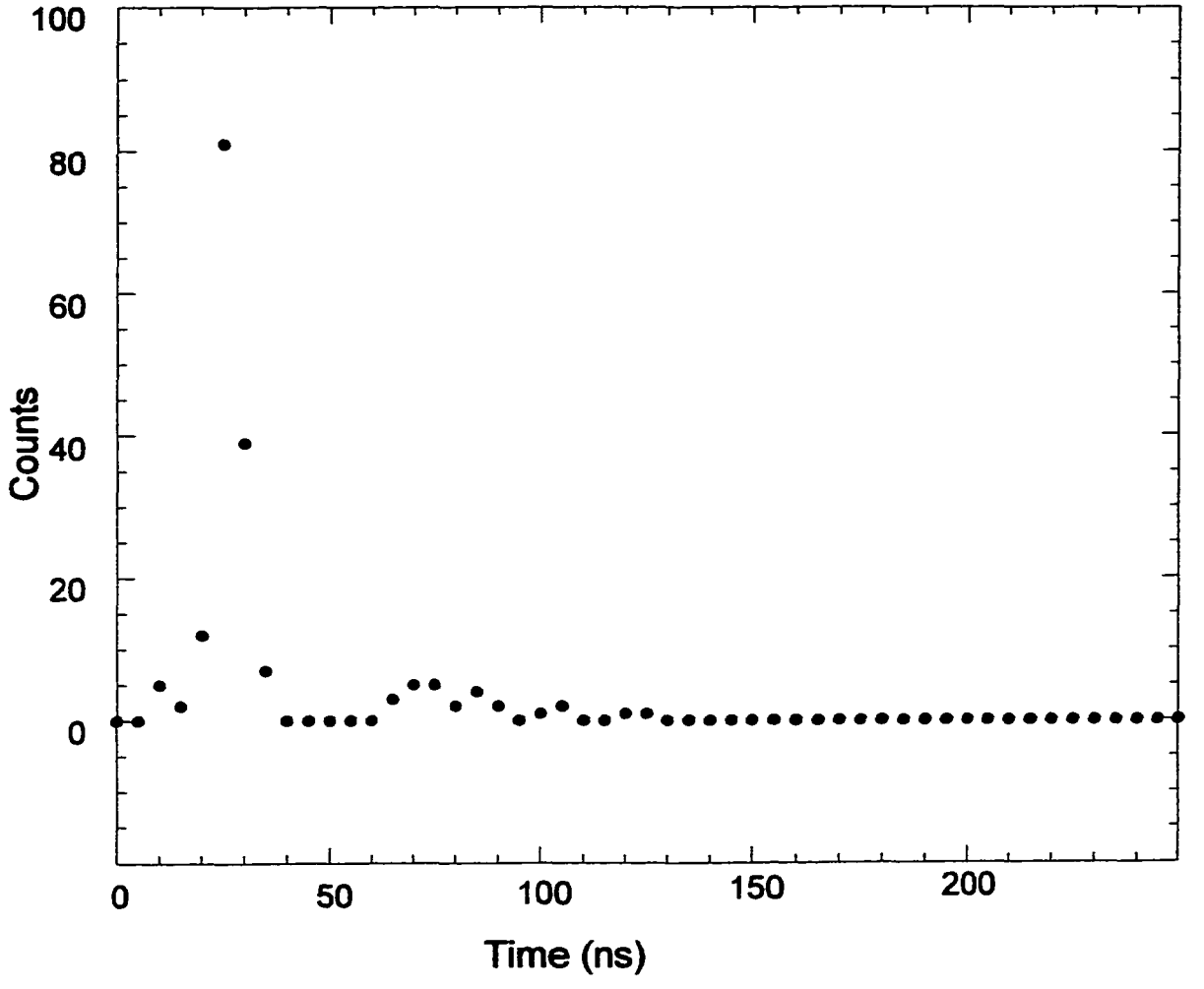

Figure (4.3.4)

level of scattered laser light. In order to use a filter instead of the monochromator , further modifications had to be made. With the light baffles placed along the path of the laser beam and along the optical detection system, 2 variable apertures were added , one at the exit of the chamber and one just in front of the PMT. This allowed us to pump and detect at the same wavelength using a filter. Figure (4.3.6) shows the scattered laser light taken with the 2 variable apertures and a filter. The laser pulse energy was 20 μ J. 30 ns after the laser pulse, the scattered laser light level is only 8 counts in the time interval 70 ns - 200 ns.

Scattered Laser Light (Pumping and Detecting at the Same Wavelength) Using Light Baffles

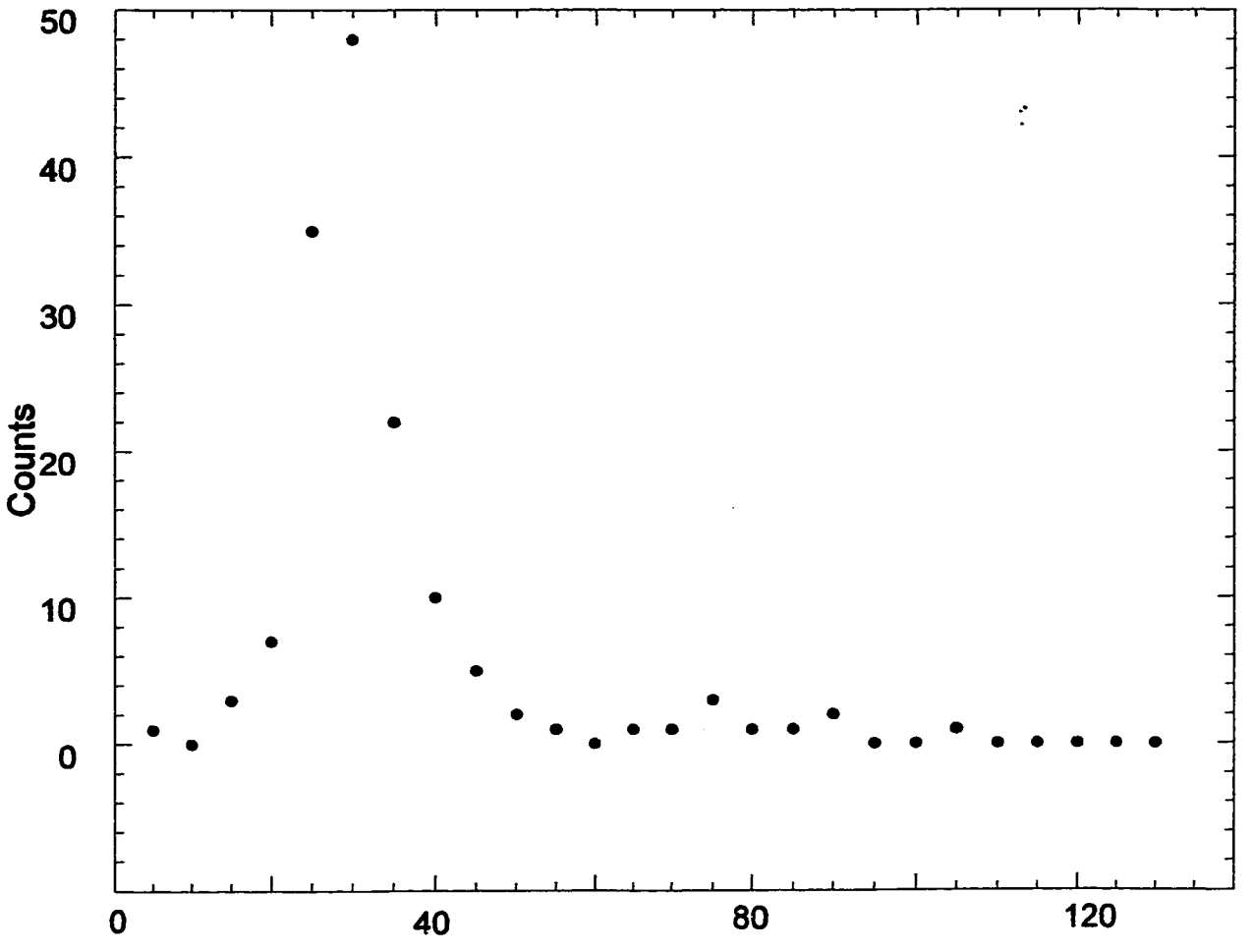

Figure (4.3.5)

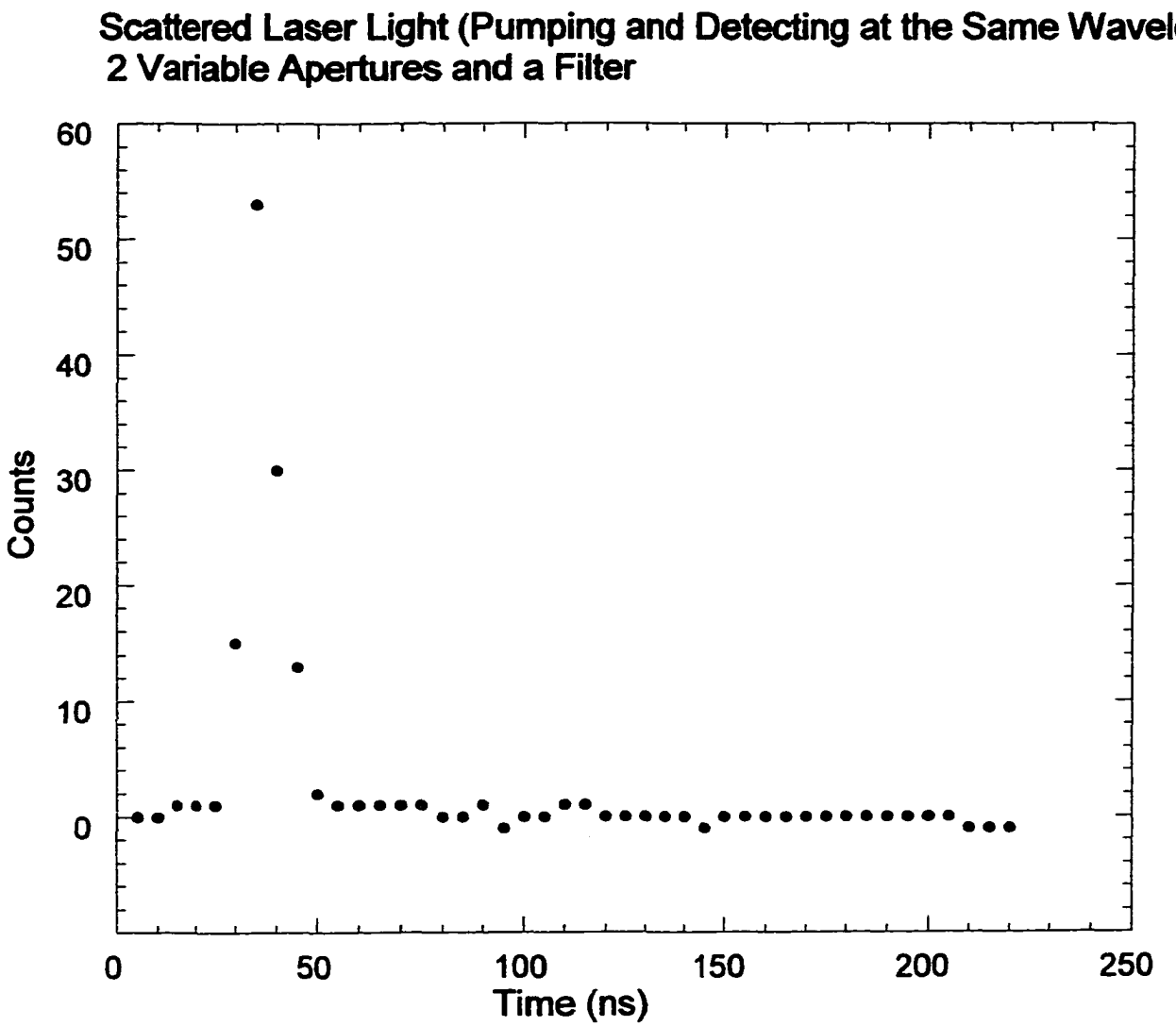

Figure (4.3.6)

4.4 The Data Acquisition Procedure for the LIF Signal:

We used a Stanford Research model SR-400 gated photon counter which was programmed to open a gate at a predetermined time after receiving a start pulse to detect the LIF signal . We directed a small fraction of the output of the dye laser to a fast photodiode which triggered the SR400. The time sequence for the counter gates is depicted in figure 4.4.1:

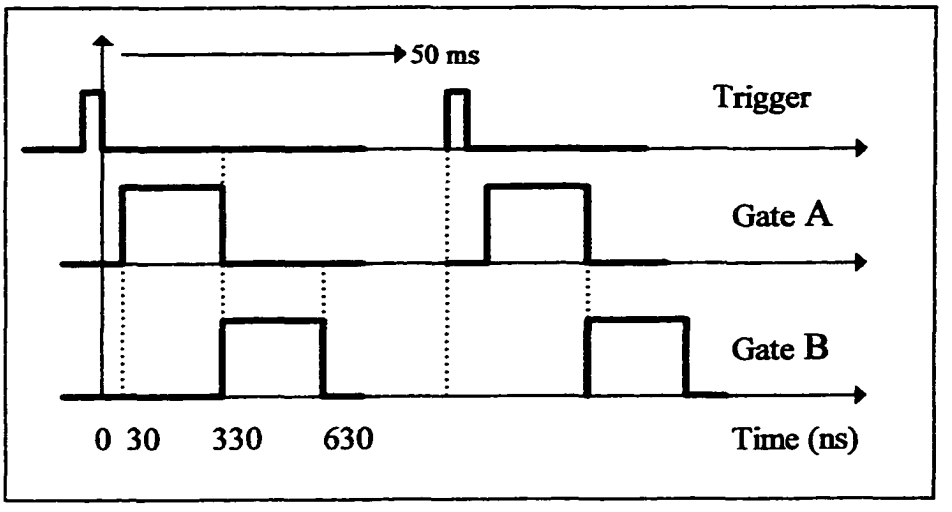

Figure (4.4.1)

Here t=0 is the time when the laser arrives in the interaction region. We used two gates labeled A and B. Both gates had a width of 300 ns which is about 5 times the radiative lifetime of the $N_2^+(B^2\Sigma_u^+)$ state . Gate A, which detects the LIF fluorescence plus the background emission, starts with a delay which was determined such that the gate opens after the laser pulse has traversed the interaction region and the scattered laser light has decayed to a negligible level. The delay was determined to be 30 ns after

the laser beam arrives at the interaction region (section 4.3). Gate B, which detects the continuous background emission produced by the electron beam starts, when gate A is closed . The gates control two counters whose outputs are fed into a personal computer. The LIF fluorescence signal of interest is obtained from the difference in the two gates, S=A-B.

Chapter 5. Results and Discussion

Application of the LIF technique to the detection of electron-impact produced ground-state species using an effusive gas beam and a continuous electron beam is technically challenging because of the weak signals involved. In the N_2 measurements carried out as part of the thesis project, the laser was tuned to pump the 0-0 vibrational band of the X-B transition of N_2^+ ions at 391 nm produced by electron impact ionization of N_2 and we detected the 0-1 vibrational band of the same electronic transition at 428 nm. By scanning the laser across the wavelength region of the rotational lines of the 391 nm band we obtained a rotationally resolved LIF spectrum of the 0-0 band. Figure (5.1) shows a portion of this spectrum near the head of the P branch for various incident electron energies (50 eV, 80 eV, 100 eV, 300 eV) . The different spectra have been displaced vertically relative to each other by 50 units for clarity of the presentation. Figure (5.2) shows a smoothed spectrum for an electron beam energy of 100 eV. The rotational structure of the N_2^+ ($B^2\Sigma_u^+ \rightarrow X^2\Sigma_g^+$) vibrational band is clearly resolved. The various peaks are labeled by the rotational quantum number of the lower rotational level. Note that the peak labeled J=12 also contains the rotational lines corresponding to J=11, 13-15 whose positions are within $\pm$ 0.05 Å of the position of J=12 line and could not be resolved. Rotational lines corresponding to J-values higher than 15

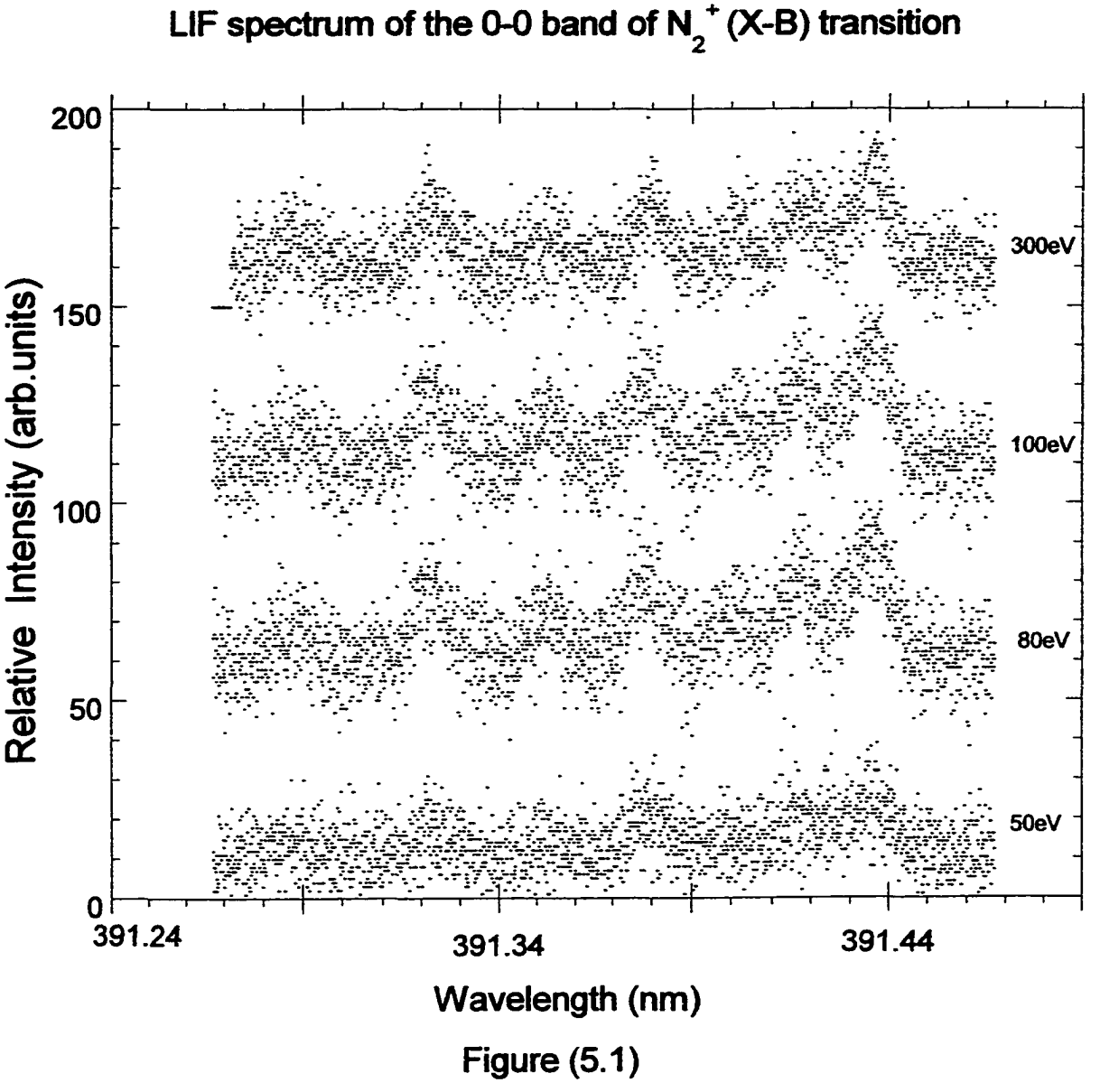

Figure (5.1)

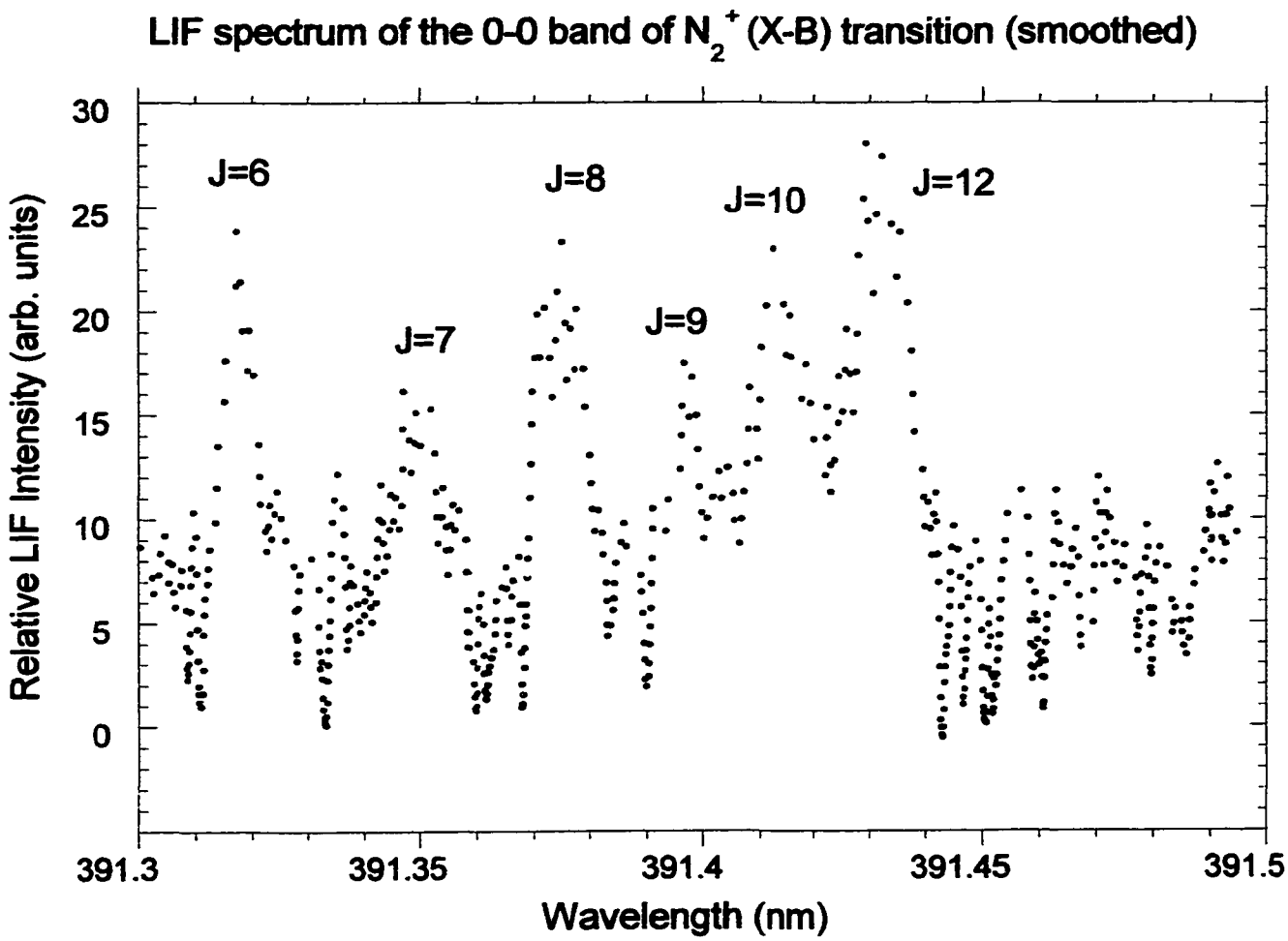

Figure (5.2)

are too weak to appear in the spectrum with appreciable intensity given that the temperature of our gas beam is close to room temperature.

The overall signal intensity is sufficiently high and the signal-to noise ratio sufficiently good to allow the observation of a distinct LIF signal. However, there is always the challenge to optimize the experimental parameters in order to improve the signal intensity and to optimize the signal-to-noise ratio. It was important to determine 1) which experimental parameters will give the highest LIF signal with the best signal-to noise ratio and 2) whether our electron beam optics and photon detection optics are properly aligned and positioned, so that the photon detector receives a signal coming from an interaction volume which is unaffected by changes in e.g. the electron beam energy. This was done by measuring the relative emission cross section for the production of N_2^+ ions in the excited $B^2\Sigma_u^+$ state following electron impact on N_2 and comparing its shape to the well-known cross section shape for B→X photoemission cross section (Borst and Zipf 1970). In section 5.1 we will discuss the variation of the LIF signal as a function of different experimental parameters. In section 5.2 we will discuss the behavior of the electron beam optics and the photon detection optics in section 5.3 we will present the electron impact cross section for formation of N_2^+ in the ground state obtained from these LIF spectra, and in section 5.4 we will present an independent calibration of the cross section obtained in section 5.3.

5.1 Variation of the LIF spectrum as a function of different experimental parameters.

Variation of the LIF Spectrum as a Function of the Delay Time Between the Laser Pulse and the LIF Detection

Since the LIF signal decays exponentially after the termination of the laser pulse, the LIF signal will be most intense, if we probe for ground state N_2^+ ions immediately after the end of the laser pulse. The factor which limits how close in time to the end of the laser pulse we can probe is the temporal decay of the scattered laser light that reaches the PMT. The data shown in figure (5.1.1) show a smoothed LIF signal of the, P(12), rotational line as a function of the delay time between the end of the laser pulse and the opening of the counter gate. There is no significant change in the rotational spectra obtained for delays between 75 ns and 85 ns measured from the arrival of the laser beam. Using longer or shorter delay times results in LIF spectra with worse signal-to-noise ratios. At a delay of 70 ns, there is distinct evidence of the presence of residual scattered laser light in the LIF spectrum. At delay of 90 ns, the LIF signal is very weak due to the exponential decay of the fluorescence . We chose to work with delays around 80 ns which represents a little more than one lifetime of the excited state.

Variation of the LIF intensity as a function of the delay time between the laser pulse and the begining of LIF detection (smoothed)

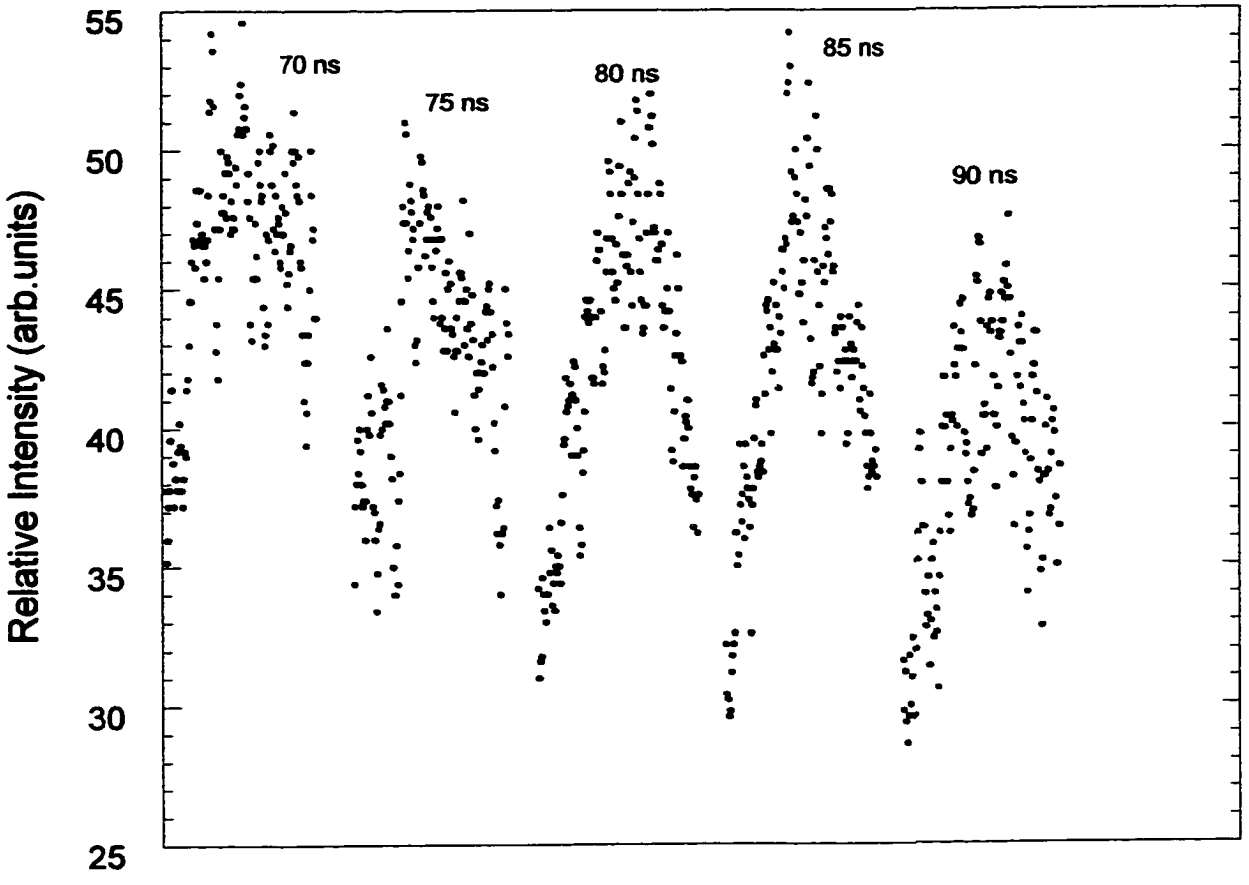

Figure (5.1.1)

Pulsing the Electron Beam - Variation of the LIF Spectrum as a Function of the Delay after Termination of the Electron Beam

The use of a pulsed electron beam eliminates the need to detect simultaneously the fluorescence originating from the N_2^+ ($B^2\Sigma_u^+$) excited state ions which are produced directly from the N_2 ground-state molecules by electron -impact ionization/excitation and the fluorescence from the LIF excitation of the $X^2\Sigma_g^+$ ground state ions. It was anticipated that the use of a pulsed electron beam would eliminate the noise in the LIF signal caused by unavoidable fluctuations in the electron beam current. Fluctuations in the electron beam current cause fluctuations in the fluorescence from electron impact produced N_2^+ ($B^2\Sigma_u^+$) ions which is the background for the detection of the LIF signal using a gated detection scheme. Figure (5.1.2) shows a single rotational line,P(12), obtained for four different laser-probe delay times after the termination of the electron beam. It was found that there was an improvement in the LIF spectrum, but that the improvement was not significant. This might indicate that the fluctuations in our electron beam current are not significant and not serious enough to cause noticeable fluctuations in the continuous background signal and that a proper background subtraction results in LIF spectra of signal intensity and signal-to-noise ratio (S/N) comparable to LIF spectra obtained with a pulsed e-beam. Table (5.1.1) shows the signal-to noise ratio for the different delays.

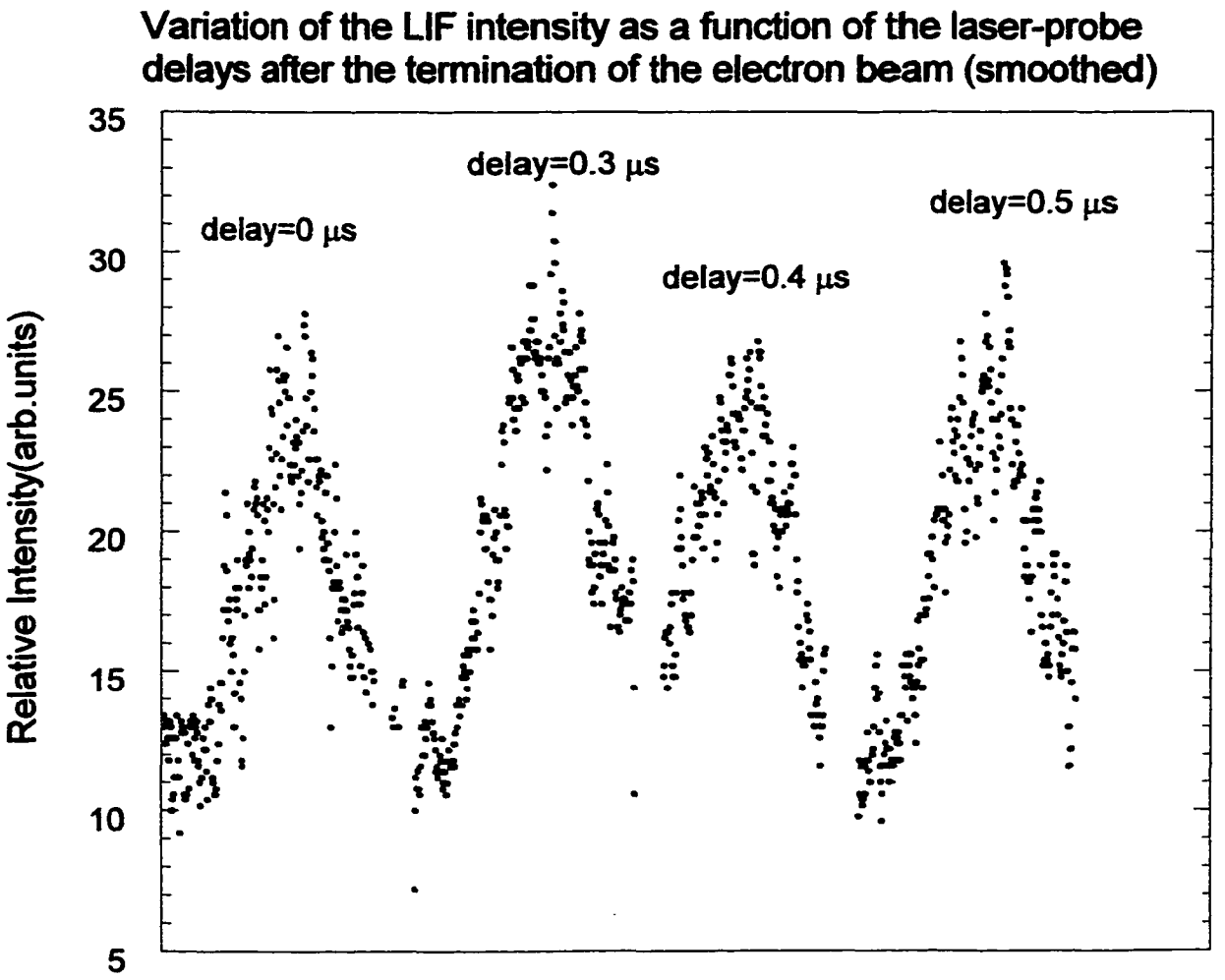

Figure (5.1.2)

Delay (μs)	S/N	S/N Improvement
0	1.91	
0.3	2.81	1.23
0.4	2.46	1.47
0.5	2.88	1.5

Table(5.1.1)

The maximum signal-to noise improvement is for a 0.5 μs delay giving an improvement in the S/N ratio by a factor of 1.5 . Due to the fact that improvement in the S/N due a pulsed e-beam is rather insignificant, we chose to work with a continuous electron beam for most of our studies.

Variation of the LIF spectrum as a function of the electron beam focusing:

If the electron beam is not properly focused in the interaction region there will be an area outside the interaction volume of the three beams (laser beam, gas beam, electron beam) where only the electron and the gas beam overlap. This region results in an emission that is detected with the same efficiency as the LIF signal and is, therefore, a source of additional noise in the LIF spectra. This is illustrated in figure (5.1.3). In case (1), the electron beam is expanding in the interaction region. This results in a large overlap between the gas beam and the electron beam which is not probed by the laser beam (light gray area). In case (2), the electron beam is focused too far behind the

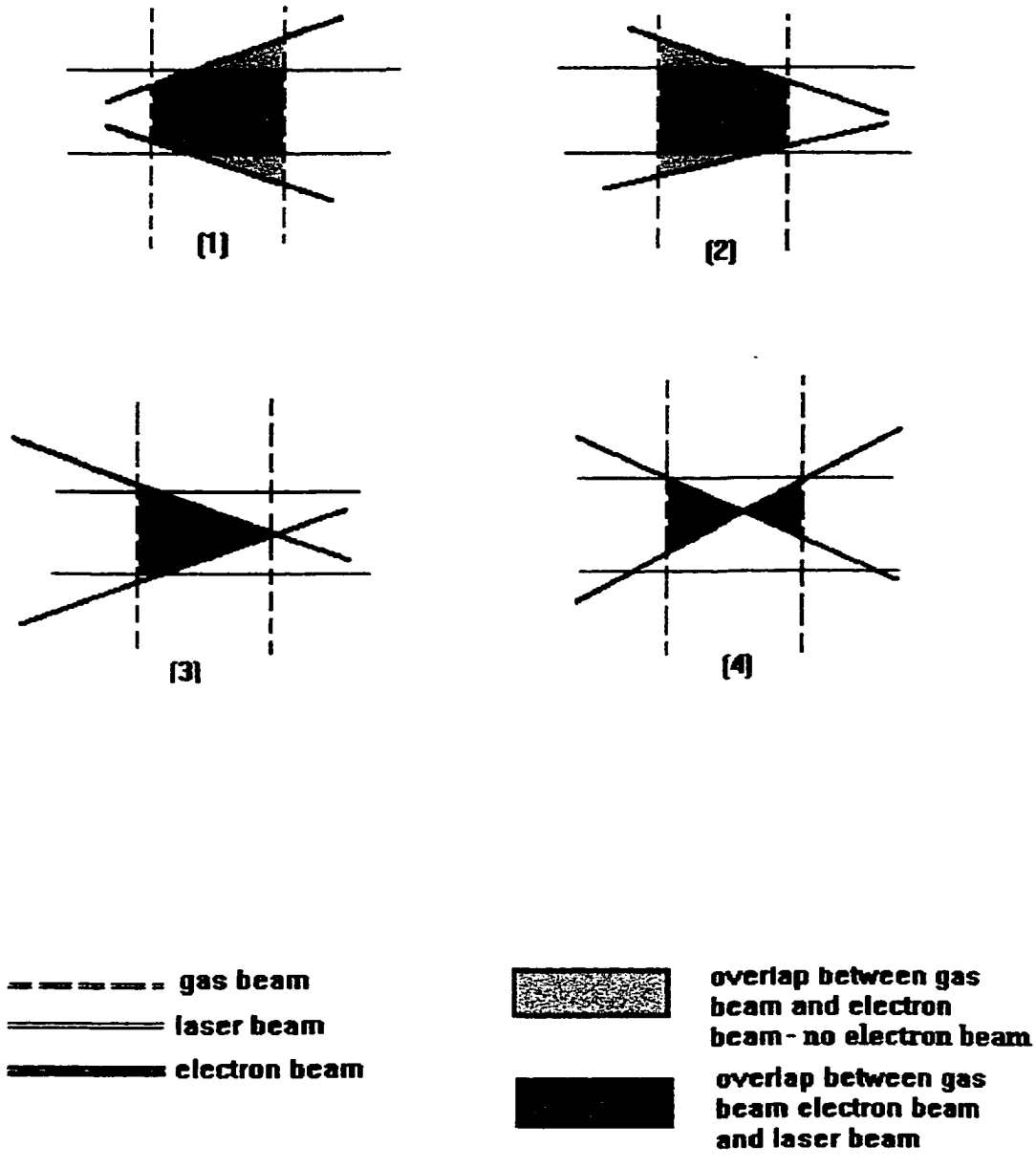

Figure (5.1.3)

interaction region and the result is similar to case (1). By contrast, in cases (3) and (4), the electron beam is focused in the interaction region and that results in a very small or no overlap between the gas beam and the electron beam in regions where there is no laser beam. Figure (5.1.4) shows single rotational line P(12) obtained for five different electron beam focusing conditions. When the voltage applied to the element EL1, V_{EL1} is smaller then the voltage applied to the element EL2, V_{EL2} , the S/N ratio is higher. The electron beam can be operated in two focusing modes, a decelerating mode where $V_{EL2}<V_{EL1}$ and an accelerating mode with $V_{EL2}>V_{EL1}$. As is illustrated in figure (5.1.3), the accelerating mode is preferred. Deceleration causes expansion of the transmitted electron beam which results in a large overlap volume between the electron beam and the gas beam . However, the LIF signal in that case is determined by the size of the laser beam which has a small diameter, so that enlarging the electron beam - gas beam overlap has a deleterious effect on the S/N ratio.

Variation of the LIF spectrum as a function of the laser pulse energy:

The analysis of the LIF data with the objective of extracting information about the population of the initial state depends on the spectral energy density of the incident laser beam, i.e. on the rate of incident photons/ cm^3 Hz. Different results are obtained in the linear regime, where the number of molecules absorbing laser photons and subsequently decaying radiatively depends linearly on the incident laser power and the in fully saturated regime, where the observed fluorescence becomes independent of the incident laser power. Therefore, it is important to know the laser power required for saturation. Figure (5.1.5) shows the variation of LIF signal of the P(12) rotational line as a function

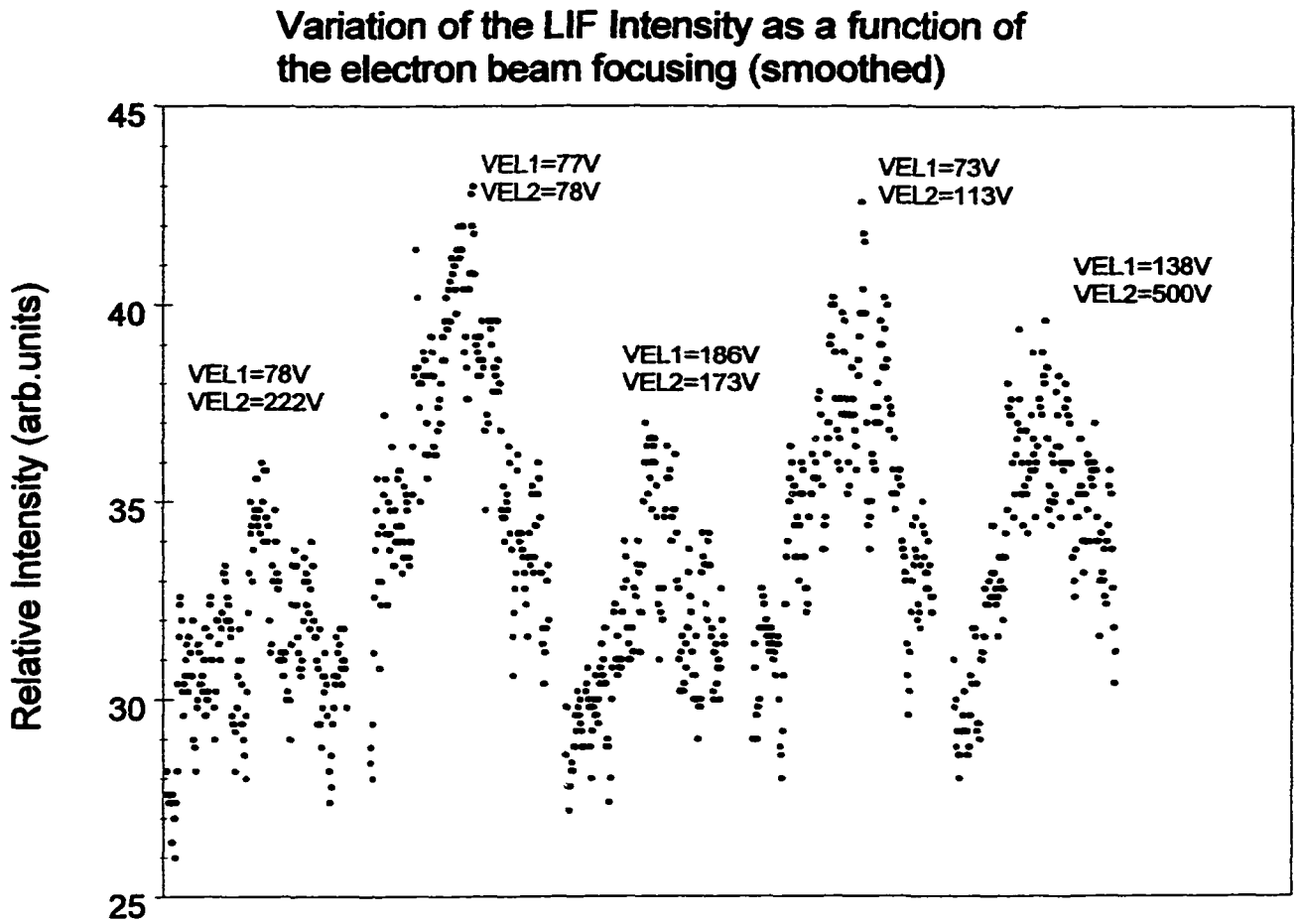

Figure (5.1.4)

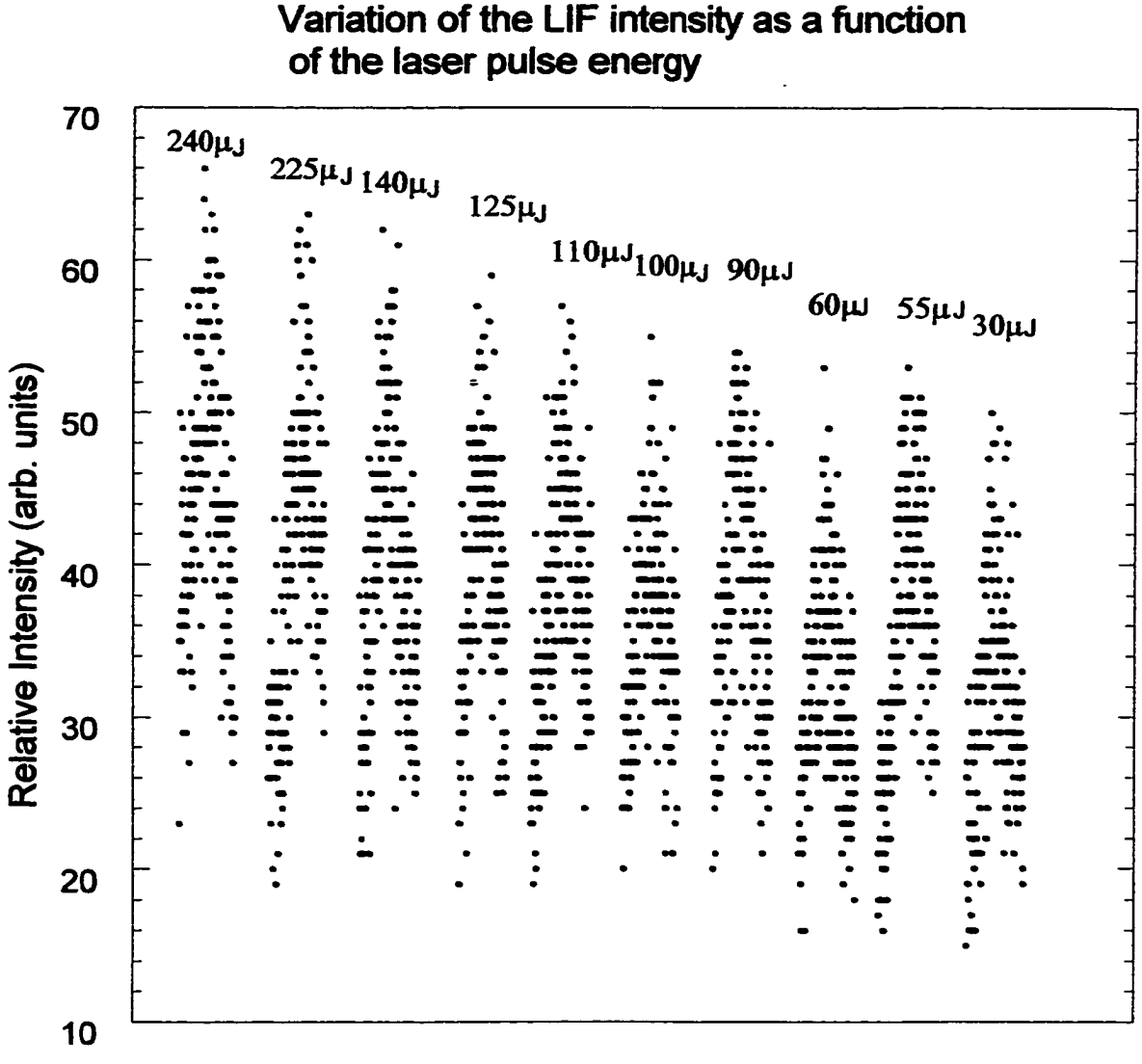

Figure (5.1.5)

of the laser pulse energy. Figure (5.1.5) allows us to extract the intensity of the LIF signal as a function of incident laser pulse energy and this is shown in figure (5.1.6). A linear relationship is established which implies that the saturation limit is not reached even at a laser pulse energy of 230 μJ in the interaction region. This agrees with findings of Hūwel et al. (1984) who reported that saturation is not reached until the laser pulse energy reaches about 430 μJ. Effects of the laser pulse energy on the LIF spectrum in the saturated regime were not studied in this work, since the maximum laser pulse energy that we could achieve was about 230μJ.

Variation of the LIF spectrum as a function of the target gas density.

Figure (5.1.7) shows the variation of the LIF spectrum as a function of the pushing pressure behind the gas nozzle which serves as indirect measure of the target gas number density in the interaction region. At a pressure in the vacuum chamber of 2.6×10^{-5} Torr (which corresponds to a pushing pressure of 1.5 Torr and a number density of approximately $2 \times 10^{13}/cm^3$, see section (3.3), the number density of the N_2 molecules in the interaction region is comparatively low, which results in a LIF spectrum of low intensity. At a pressure of 1×10^{-4} Torr (which corresponds to a pushing pressure of 3 Torr and a number density of approximately $4 \times 10^{13}/cm^3$), the gas beam is wide presumably due to the fact that significant deviation from molecular flow condition occur. This results in a broad interaction volume which, in turn, leads to increased background fluorescence from the large overlap of the electron beam and the gas beam. We found that the S/N ratio is highest at pressures around 5×10^{-5} Torr corresponding to a pushing pressure of 2 Torr.

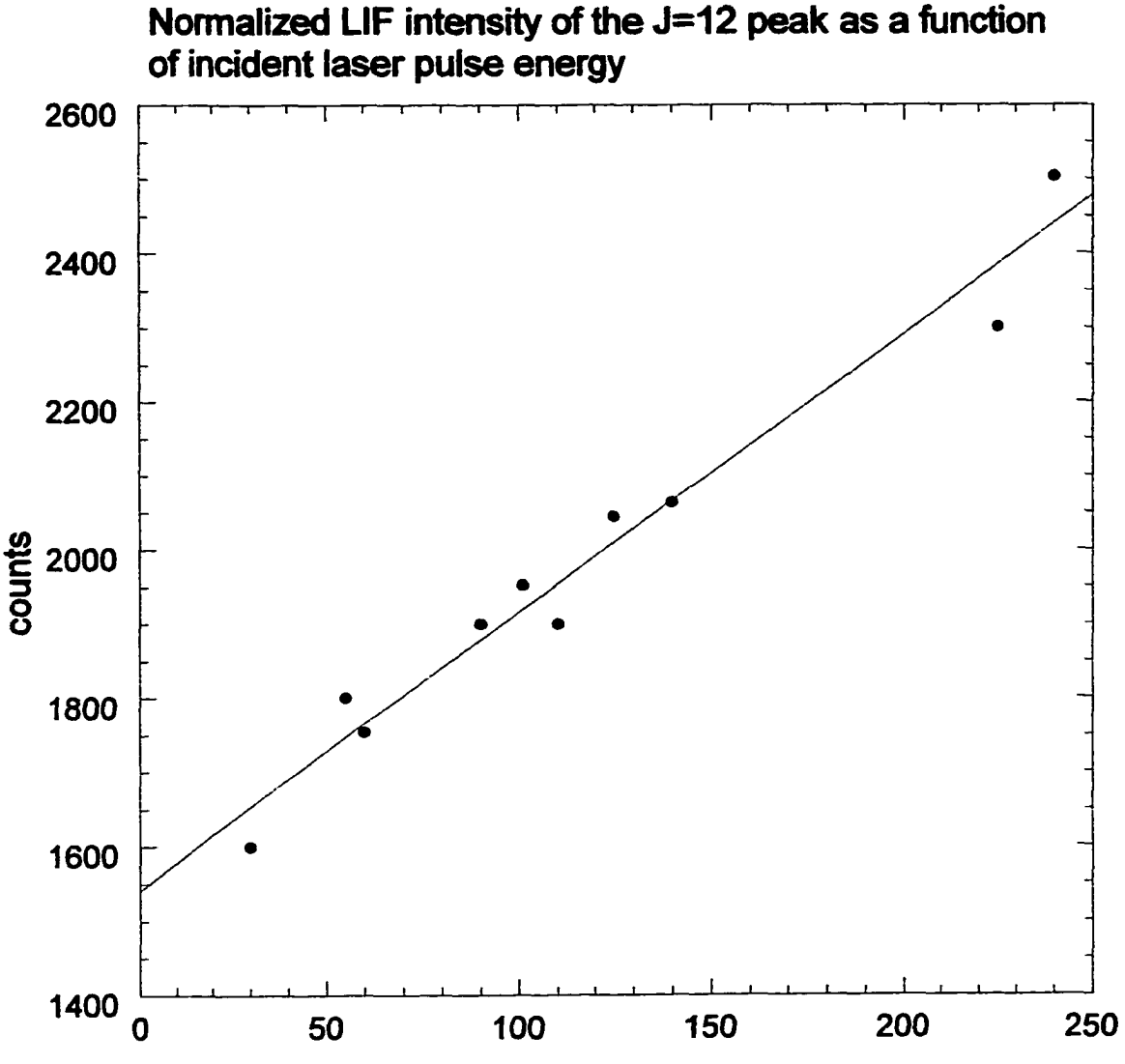

Figure (5.1.6)

Variation of the LIF intensity as a function of the pressure (smoothed)

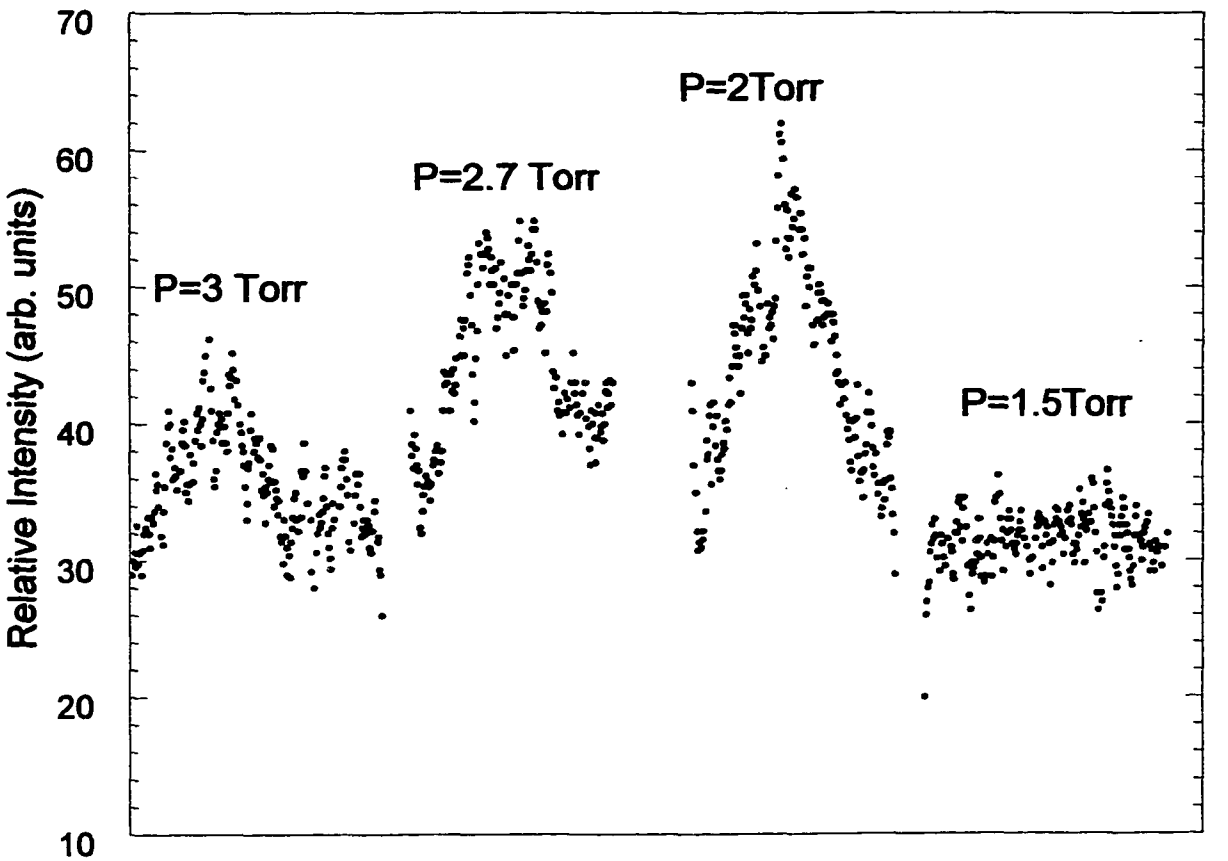

Figure (5.1.7)

Summary

In summery, we found that the best operating conditions for obtaining LIF spectra of optimum signal intensity and S/N ratio in our experimental set-up are

1) using a time delay of 30 ns- 35 ns between the time the laser pule is in the interaction region and the beginning of the gated LIF detection, 2) operating the electron gun in an acceleration mode, 3) maximizing the laser pulse energy of our laser beam (up to 230 μJ), and 4) using a pressure inside the vacuum chamber of about $5x10^{-5}$ Torr corresponding to a pushing pressure of 2 Torr and a target gas density of about $3x10^{13}$ molecules/cm^3.

Figure (5.1.8) shows a LIF signal of the P(12) rotational line at an electron impact energy of 100 eV taken at the optimum operating conditions. This is the line that was typically used for the cross section measurements.The total number of LIF counts (area under the peak) is approximately 2000 counts which results in a <3% uncertainty in the counting statistics.

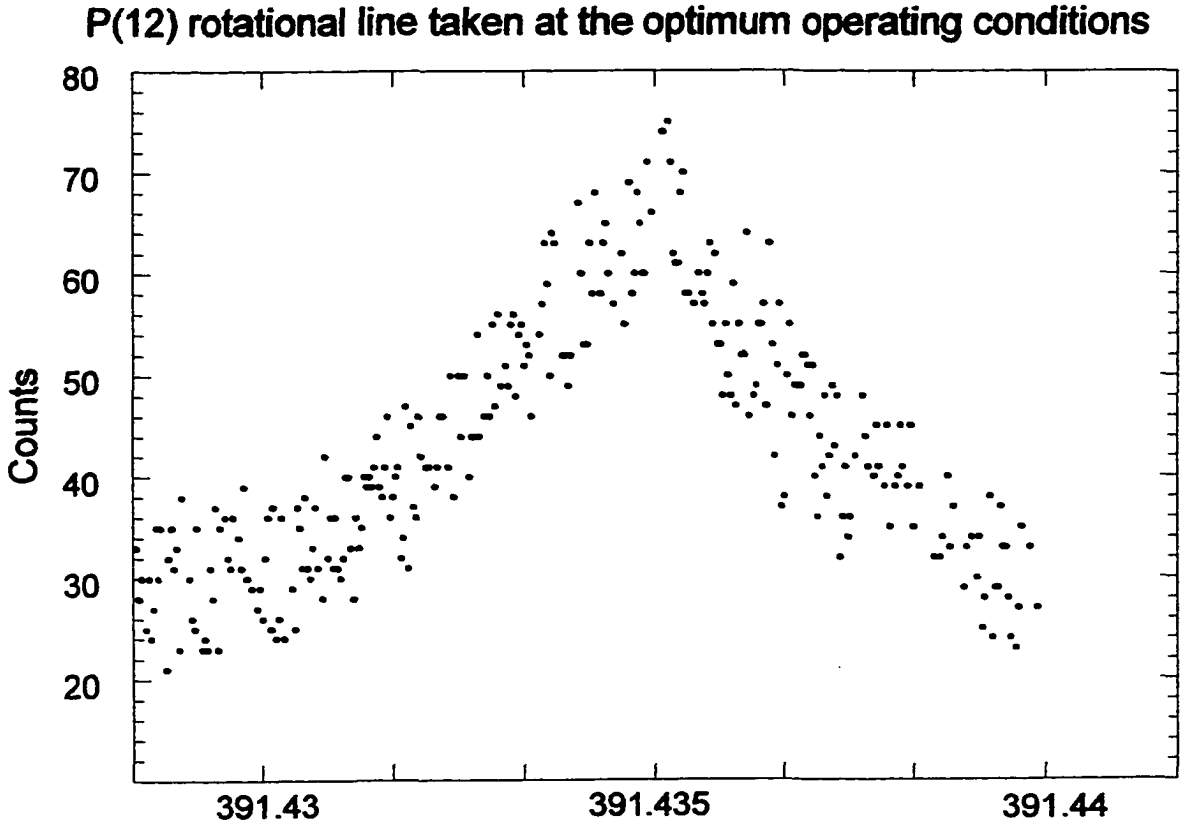

Figure (5.1.8)

5.2 Cross Section for the formation of N_2^+ in its $B^2\Sigma_u^+$ state.

The relative cross section for the production of N_2^+ in the $B^2\Sigma_u^+$ excited state following electron impact was measured by monitoring the $B^2\Sigma_u^+ \rightarrow X^2\Sigma_g^+$ (0,1) spontaneous emission at 428 nm as a function of electron impact energy. Figure (5.2.1) shows the measured cross section as a function of the electron impact energy. Each data point represents a data acquisition time of 5 s. A number of comments should be made: 1) We used an interference filter with a 10 nm (FWHM) band width to isolate the emission under study. Therefore, the measured signal for the monitored (0,1) band is a summation over all the individual rotational lines populated by the electron impact process. The structure in the low energy region below 20 eV is due to the fact that the (1,5) vibrational band of the N_2 ($C^3\Pi_u \rightarrow B^3\Pi_g$) transition emits radiation at 427 nm. This emission falls within the band pass region of the interference filter and, therefore, contributes to the measured cross section. Figure (5.2.2) shows the N_2 ($C^3\Pi_u \rightarrow B^3\Pi_g$) (0,0) cross section (Aarts and Heer 1969) . Since the N_2 ($C^3\Pi_u \rightarrow B^3\Pi_g$) cross section shape is independent of the vibrational band, the cross section shown in figure (5.2.2) also reflects the cross section shape of the N_2 ($C^3\Pi_u \rightarrow B^3\Pi_g$) (1,5) band. The N_2 ($C^3\Pi_u \rightarrow B^3\Pi_g$) emission has a threshold of (11 eV) which is below the (19 eV) onset of the $B^2\Sigma_u^+ \rightarrow X^2\Sigma_g^+$ (0,1) emission. The excitation of the upper $C^3\Pi_u$ of the N_2 (C→ B) second positive band system is the result of a spin-forbidden excitation process from the N_2($X^2\Sigma_g^+$) ground state. Spin forbidden excitation processes typically reach a maximum in their cross section a few electronvolts above threshold and decay

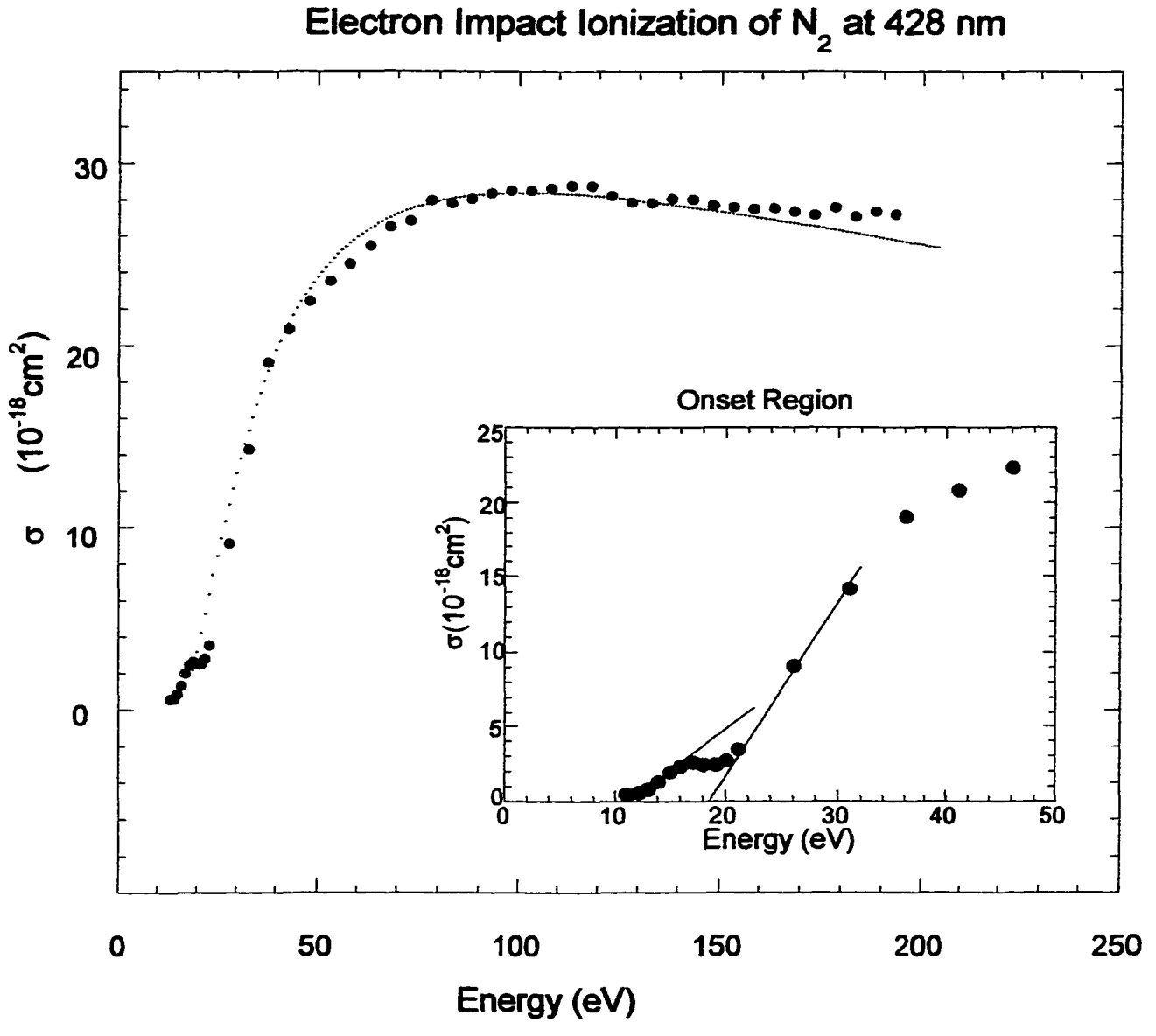

Figure (5.2.1)

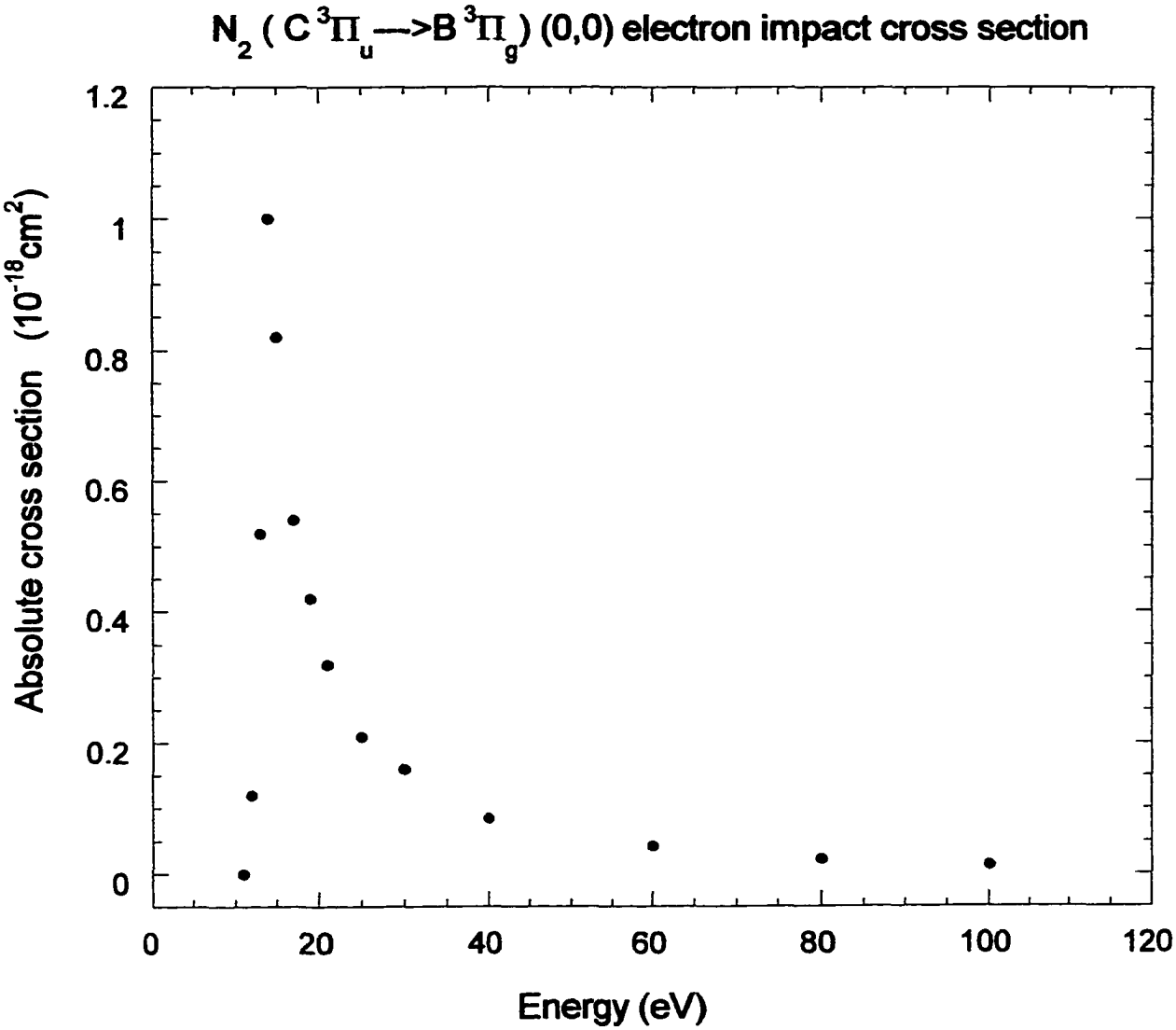

Figure (5.2.2)

rapidly for higher impact energy with a $1/E^3$ asymptotic energy dependence with the electron energy E (Stanton et al. 1969). Therefore, it is not expected that the N_2 C→ B (1→5) emission contributes significantly to the measured emission cross section above approximately 30 eV or 40 eV. The doted line in figure(5.2.1) indicates the shape of the cross section measured by Borst and Zipf (1970) . The good agreement between our measured cross section shape and the cross section shape of Borst and Zipf (1970) (better then 4 % for energies above 30 eV) indicates that our electron-beam optics and photon detection optics are designed in such a way as to ensure an interaction volume that does not change as we change the electron energy. Relative cross section measurements of the N_2^+(B→X) emission were routinely carried out before and after the LIF measurements to ensure optimum operating conditions for the LIF detection during the entire data acquisition cycle.

5.3 Cross Section for the formation of N_2^+ in its $X^2\Sigma_g^+$ state.

Preview of Previous Work

Before beginning the cross section discussion, it is worthwhile to review what is known about N_2^+ branching ratios. N_2 is perhaps the most thoroughly studied molecule in terms of its interactions with electrons both theoretically and experimentally (A. Zecca et al. 1996). There are three electronic states of N_2^+ which are appreciably populated following electron impact ionization of ground state N_2, the ground state and the $A^2\Pi_u$ and $B^2\Sigma_u^+$ excited states. Measurements carried by Fano et al.(1994) confirmed that the N_2^+ ($X^2\Sigma_g^+$) state is cascade free in the sense that the ionization-excitation of N_2 by electron impact ions are formed via the following process i) direct ionization of N_2 and ii) ionization-excitation of N_2^+($A^2\Pi_u$, $B^2\Sigma_u$,...) followed by the subsequent decay of the excited N_2^+ state directly to the $X^2\Sigma_g$ ground state. Processes such as the formation of $N_2^+(D^2\Pi_u)$ ions followed by the two-step decay $D^2\Pi_u \rightarrow B^2\Sigma_u$, $A^2\Pi_u \rightarrow X^2\Sigma_g$ do not contribute to the formation of N_2^+ ($X^2\Sigma_g$) ions. In fact even though the $D^2\Pi_g \rightarrow A^2\Pi_u$ emission was detected and its emission cross section was measured (Fano et al. 1994), its intensity is such that the $D^2\Pi_g \rightarrow A^2\Pi_u$ cascade contribution to the $A^2\Pi_u \rightarrow X^2\Sigma_g^+$ cross section is estimated to be only 1%. In the same experiment, the $D^2\Pi_g \rightarrow B^2\Sigma_u$ emission was sought, but no discernible signal was found. Therefore, we can assume that the the N_2^+ ($X^2\Sigma_g^+$) state is cascade free.

Total N_2^+ Production:

Even though the data of Rapp and Englander-Golder (1965) are more then 30 years old, many workers today still use them for the total ionization cross section for $e^- + N_2$ collisions (Van Zyl et al., 1995) This cross section is given by

$$\sigma_i = \sigma [N_2^+] + 2\sigma [N_2^{++}] + \sigma [N^+] + 2\sigma [N^{++}] \quad , \quad (5.3.1)$$

where the factor of two denotes the fact that the doubly-charged ions are counted twice in the product-ion current measurement. σ_i was reported to be 25.3×10^{-17} cm^2 at 100 eV. In another paper, Rapp et al. (1965) reported a fraction of 0.22 contained in σ_i that results from dissociative ionization processes which is given by the sum of the last two terms in 5.3.1. Recently, Van Zyl and Stephen (1994) estimated that this value should be increased to about 0.25, a value which is also supported by the work of Straub et al. (1995). In addition, Märk (1975) found the ratio of $\sigma [N_2^{++}] / \sigma [N_2^+]$ to be 0.018, while Halas and Adamczyk (1972) obtained a value of 0.014. Van Zyl et al. (1995) used the average of 0.016 and a dissociative ionization fraction of 0.25 in (5.3.1) and estimated $\sigma [N_2^+]$ to be 18.4×10^{-17} for the total N_2^+ production cross section. Table (5.3.1) summarizes the results for the total N_2^+ production cross section for 100 eV electron impact on N_2 .

Investigators	Cross Section (10^{-18} cm^2)
Halas and Adamczyk (1972)	191
Märk (1975)	165 ± 11.5
Krishnakumar and Srivastava (1990)	208 ± 16.64
Freund et al. (1990)	179
Van Zyl et al (1995)	184
H. C. Straub et al. (1995)	195 ± 9.75

Table (5.3.1) Total N_2^+ Production Cross Section for 100 eV Electron Impact on N_2

$N_2^+(B)$ Production:

The first three studies of the N_2^+ first negative (0,0) band emission cross section located the maximum of the cross section near 100 eV. Dalgarno et al. (1965) reported a maximum value of $6x10^{-18}$ cm^2. McConkey and Latimer (1965) and McConkey et al. (1967) found a cross-section that was 2.5 times larger, with a maximum value of $15.2x10^{-18}$ cm^2 at 120 eV. Table (5.3.2) summarizes the results of N_2^+ first negative (0,0) band emission cross sections (10^{-18}) for 100 eV electron impact on N_2 done after 1965.

Investigators	Cross Section(10^{-18} cm^2)
McConkey and Latimer(1965)	14.7
McConkey et al. (1967)	$15.2 \pm 0.6^*$
Aarts et al. (1968)	21.2 ± 2.1
Sarvastava and Mirza (1968)	16.8 ± 3.6
Borst and Zipf (1970)	17.4 ± 2.6
Shaw and Campos (1983)	15.4 ± 1.5
Stanton and St. John (1996)	$15.6 \pm 2.8^*$
Doering and Yang (1997)	14.8 ± 2.5

* Value at 120 eV

Table (5.3.2). N_2^+ first negative (0,0) band emission cross sections (10^{-18}) for 100 eV electron impact on N_2

Almost universally, the carefully executed measurements of this emission cross section performed by Borst and Zipf (1970), are adopted (Van Zyl and Pendleton, 1995). While we agree that these data are probably the most accurate result currently available, it should be pointed out that Doering et al. (1996) suggested that there are several reasons to question whether the Borst and Zipf (1970) cross section is the most reliable one. First, McConkey et al. (1967) used a tungsten filament standard lamp calibration method to repeat the earlier measurements of McConkey and Latimer (1965), who had used helium lines with known excitation cross sections for calibration. Excellent agreement between the two sets of measurements was obtained. The measurements of

Borst and Zipf (1970) used only a standard lamp calibration. Second, Table (5.3.2) shows that, aside from the very high result of Aarts et al. (1968), the results of all measurements are below the Borst and Zipf data. Third, the recent optical emission measurement by Shaw and Campos (1983), who used helium lines for calibration, agreed well with the results of McConkey and Latimer (1965), McConkey et al. (1967) and Stanton and St. John (1969).

$N_2^+(A)$ Production:

In sharp contrast to the first negative band emission discussed above, the data on Meinel band (A→X) emission cross section from electron impact on N_2 show poor agreement. Much of the scatter in the reported cross sections can be attributed to the long radiative lifetimes (~ 10 μs) of the various $N_2^+(A, v')$ vibrational levels (Holland and Maier, 1972; Peterson and Moseley, 1973). Thus, unless an experimental photon detector has an extensive field of view, some excited $N_2^+(A)$ ions may drift out of the field of view before decaying causing the measured emission cross section to be too small. Table (5.3.3) summarize the N_2^+ Meinel band emission cross sections (10^{18} cm^2) for 100 eV electron impact on N_2.

Investigators	Cross Section(10^{-18} cm^2)
Staton and St.Jhon (1969)	48.0
Piper et al. (1986)	115.0±23
Goembel et al. (1994)	66.2±8.0
Van Zyl and Pendleton (1995)*	101.0±19.2
Doering and Yang (1997)	87.9±7.0

* Calculated from Borst and Zipf (1970) first negative system (0,0) cross section

Table (5.3.3) N_2^+ Meinel band emission cross sections (10^{-18} cm^2) for 100 eV electron impact on N_2

$N_2^+(X)$ Production:

From the above discussion N_2^+ cross section data the cross section for the formation of $N_2^+(X)$ ions can be estimated. Fons et al. (1993) based on the measurements of St. John and Stanton (1969) obtained an estimated value for the $N_2^+(X)$ cross section of $130x10^{-18}$ cm^2. However, because of the conflicting sets of cross sections for $N_2^+(A)$, Fons et al. (1993) found the cross section for $N_2^+(X)$ to range from $130x10^{-18}$ to $370x10^{-18}$ cm^2. In view of the wide variance in the cross sections involved, they could only conclude that the cross section for $N_2^+(X)$ and $N_2^+(A)$ are roughly comparable, but the that $N_2^+(B)$ cross section is probably several times smaller. Several more authors estimated the $N_2^+(X)$ cross section in a similar way, Kawazumi et al. (1987), Darrach et al. (1990), and Van Zyl et al. (1995). Van Zyl et al. (1995) deduced a value of

$60.5x10^{-18} \pm 45\%$ for the $N_2^+(X)$ cross section. In conclusion, the cross section for ionization-excitation of the $N_2^+(B)$ state is rather well-known as are the total N_2 ionization cross section and the total N_2^+ parent ionization cross section (see above). On the other hand, the experimentally determined cross section of N_2^+ ions in the A-state is known only to within an error margin of about 50% (see above). This renders it impossible to estimate the cross section for the formation of $N_2^+(X)$ ground-state ions with reasonable confidence. Recently, Doering and co-workers (1997) used the electron-electron coincidence (e,2e) technique to study electron impact ionization-excitation processes in N_2 and obtained the branching ratios to the various final states of the resulting ions. Their result- when combined with the known total parent N_2^+ cross section- allowed the extraction of absolute cross sections for the formation of $N_2^+(X)$. Their cross section of $86.9x10^{-18}$ at 100 eV with a quoted error of 8 % agrees purely with the cross section reported by Van Zyl and Pendleton (1995). In addition, both authors only reported a single cross section value at 100 eV, but did not report a cross section shape.

Present Results

Figure (5.3.1) shows the relative cross section for the formation of N_2^+ ions in the ground state obtained in this thesis . The data points were determined by scanning across the J=12 rotational line for various incident electron beam energies. It should be noted that the data presented are an average of 6 different measurements. Also shown in fig (5.3.1) (doted line) is an estimated energy dependence of the N_2^+ (X) cross section normalized to our cross section at 75 eV. This estimated shape has been obtained by

subtracting the N_2^+ B-state cross section shape of Borst and Zipf (1970) and the N_2^+A-state cross section shape of Piper et al. (1986) from the total N_2^+ parent ionization cross section shape of Krishnakumar and Srivastava (1990) (see section 2.2). As one can see, our measured N_2^+(X) cross section shape is in a good agreement with the estimated shape in the energy region from threshold to 200eV. The relative cross section curve was put on an absolute scale by normalization to the absolute cross section value of Doering and Yang (1996) at 100 eV as shown in figure (5.3.2). Also shown in figure 5.3.2 is the estimated absolute N_2^+(X) cross section as obtained in section 2.2 .

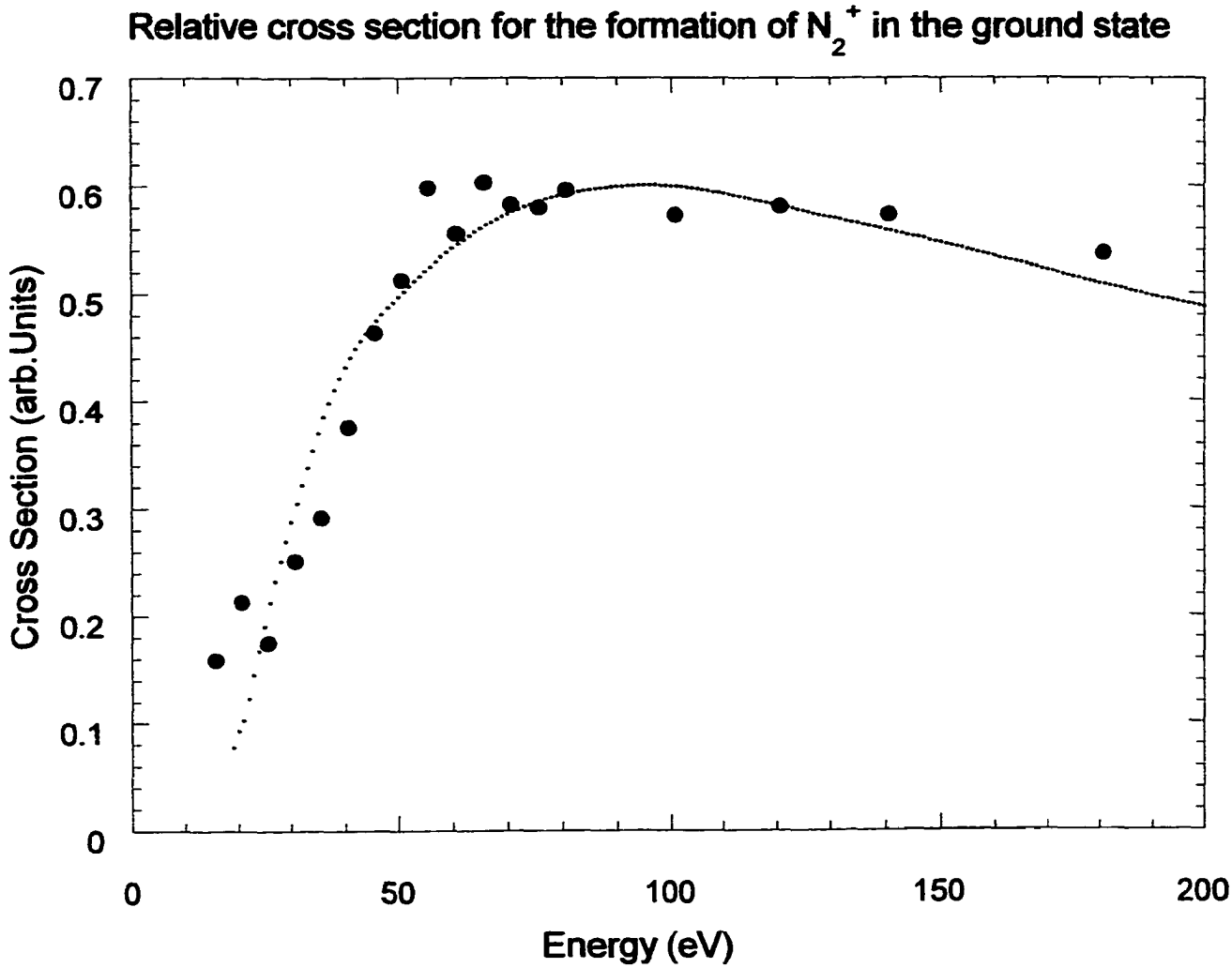

Figure (5.3.1)

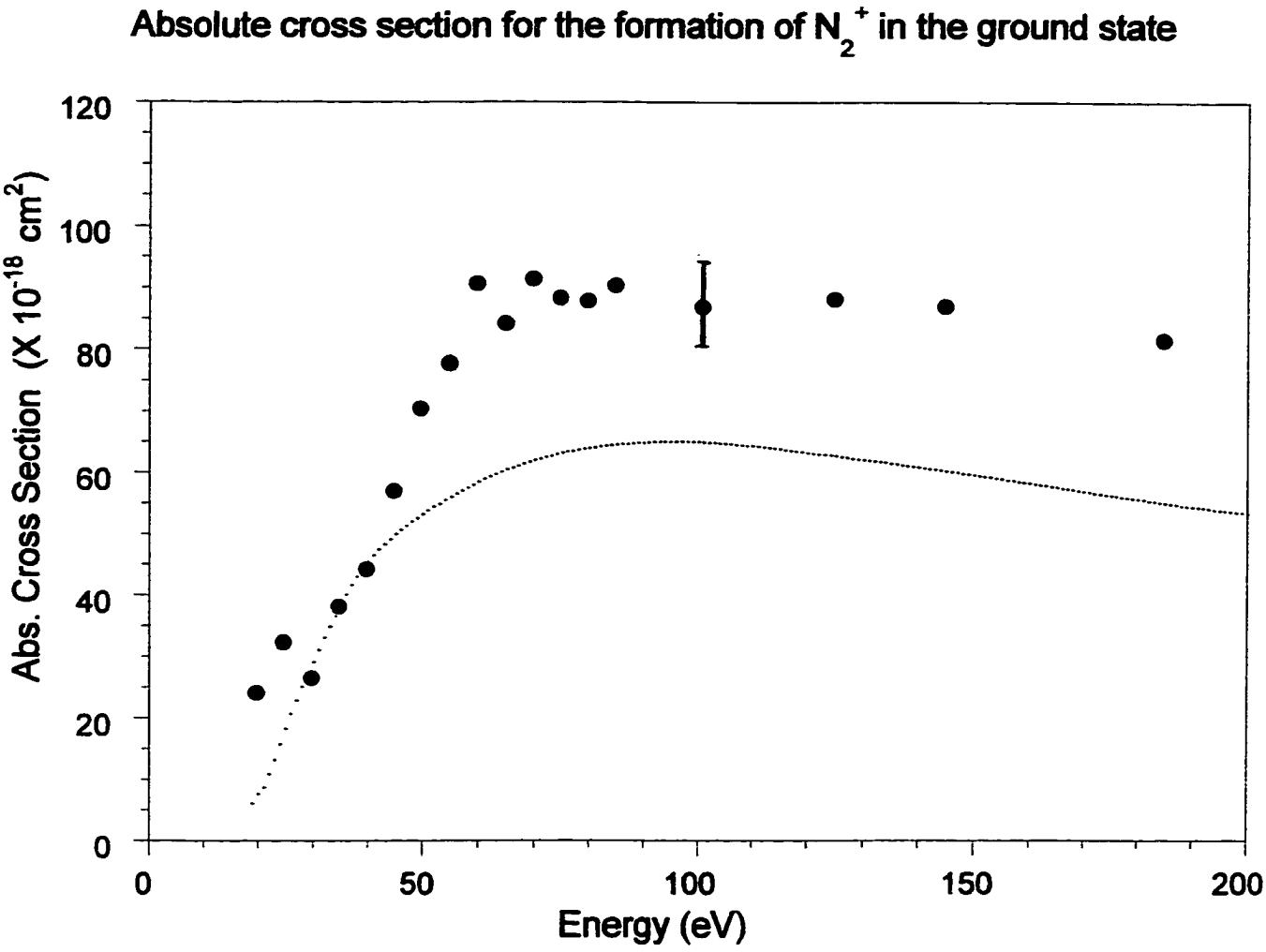

Figure (5.3.2)

Experimental Error

Experimental uncertainties may arise from either systematic or random sources. Systematic uncertainties arise due to known or unknown errors which, if not accounted for, give an overall bias to the results. Random errors arise from the statistical nature of any measurement and may be reduced by repeating the experiment a large number of times. Table (5.3.4) shows the various sources of errors in our measurement.

Description	Contribution to Uncertainty
1) pulse to pulse reproducibility of the laser pulse energy	< 5%
2) stability of electron beam current	< 1%
3) stability of gas beam density	< 1%
4) constancy of the interaction volume as a function of electron energy [1]	< 4%
5) counting statistics[2]	< 1%

Table (5.3.4)

[1] see section (5.1)

[2] The count rate represents a random error whose statistical uncertainty is $1/\sqrt{N}$ where N is the accumulated number of counts. In the present experiment the total number of LIF counts at 100 eV is approximately 2000 and the measurement is repeated 6 times.

A typical error bar for our cross section is given for the data point at 100 eV (Figure 5.3.2). We summed in quadrature the various systematic uncertainties (1-4) and added to it linearly the uncertainty due to the counting statistics. The uncertainty in our measurement is < 8%. Not included in our error bar is the 8% uncertainty in the benchmark cross section value of Doering and Yang (1996).

5.4 Independent Absolute Calibration of the Cross Section for the Formation of N_2^+ Ions in the $X^2\Sigma_g^+$ Ground state.

In this paragraph we present a different, independent way to put the relative N_2^+ ($X^2\Sigma_g^+$) cross section on an absolute scale. The motivation for this comes from the fact that there exists a large discrepancy between the N_2^+(X) cross section obtained by Doering and Yang (1997) from their electron-electron coincidence studies, $86.9 \pm 7.0 \times 10^{-18}$ cm^2 at 100 eV and the value extracted by Van Zyle and Pendleton (1995) from the critical analysis of all previously reported cross section data, $60.5 \pm 27.0 \times 10^{-18}$ cm^2 at 100 eV. One might argue that the cross section of Doering and Yang (1997) is more reliable, since it is based on new experimental data, and it has a smaller error margin. However, acceptance of their cross section value requires the value of the previously accepted N_2^+ B state "benchmark" cross section of Borst and Zipf (1970) to be lowered by 25%, a margin which exceeds the stated uncertainty of that cross section significantly.

Method

The determination of an absolute cross section requires the measurement of all quantities and parameters that determine the cross section such as electron beam current, number density of target gas atoms or molecules, overlap of electron beam and gas beam (and, if applicable, laser beam), and sensitivity of the detection system (Van Zyl et al. 1983). This is often difficult to do. Therefore, a different approach, which is more frequently employed, is based on a relative measurement of the cross section under study which is subsequently

put on an absolute scale by e.g. normalization relative to a well-known "benchmark" cross section. The simplest example for such a normalization is the normalization of the relative $N_2^+ (X^2\Sigma_g^+)$ ionization cross section to the "benchmark" value of 86.9×10^{-18} cm^2 at 100eV determined by Doering and Yang (1997) as described in the previous section. In this section, we discuss the result of a normalization procedure that employes a different "benchmark" cross section, one which is obtained directly in our apparatus. We use the well known cross section for the production of helium atoms in the $2s\ ^3S$ state by electron impact at 20.4 eV on He in the $1s\ ^1S$ ground state. The resulting He ($2s\ ^3S$) number density is probed by LIF of the He $2s\ ^3S \leftrightarrow 3p\ ^3P$ transition at 388.86 nm. The energy level diagram for the processes involved is shown figure 5.4.1.

Partial energy-level diagram of helium indicating the relevant energy levels (not to scale)

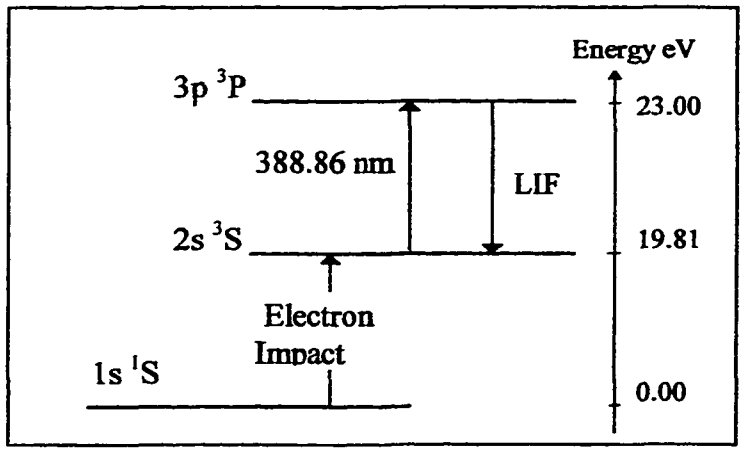

Figure 5.4.1

One advantage of this procedure is the fact that the same dye and the same detection filter can be used for both the He and the N_2 measurements. The choice of 20.4 eV for the measurement in He was motivated by several factors, (i) the $1s\ ^1S \rightarrow 2s\ ^3S$ excitation cross section is sufficiently large at this energy to produce an appreciable density of He $2s\ ^3S$

atoms,(ii) this energy is just below the 20.61 eV onset for the formation of metastable He 2s ^{1}S atoms, which is important in view of the fact that the most reliable absolute cross section values are available only for the formation of the combined (unresolved) He 2s ^{1,3}S metastable states, and (iii) the energy of 20.4 eV is below the threshold for populating the He 3p ^{3}P state the lowest lying state above the 2s ^{3}S state which can decay radiatively to the 2s ^{3}S state and, as a sequence, the LIF measurement in He is free of any 3p ^{3}P→2s ^{3}S background arising from the direct population of the upper state by the continuos electron beam.

Experimental details

For the He LIF calibration measurement, additional experimental difficulties had to be overcome, (i) the expected signal is small based on the comparatively small cross section for producing He (2s ^{3}S) of 4.0 x 10^{-18} cm^2 at 20.4 eV (Borst 1974), (ii) the electron beam current at 20 eV is only about 1 μA, (iii) pumping and detecting the LIF signal at the same wavelength renders blinding of the PMT by scattered laser light a serious issue (see section 4.3.2), and (iv) the need to work below the onset for the 3p ^{3}P state requires an accurate determination of the electron beam energy. The scattered laser light problem was addressed by modifying the apparatus as described in section 4.3.2. and by reducing the laser pulse energy in the interaction region to about 20 μJ. In addition, the delay between the end of the laser pulse in the interaction region and the start of the data acquisition cycle was extended to 100 ns (about 1 lifetime of the He (3p ^{3}P) state), so that the scattered laser light was less then 1 count in the time interval from 100 ns to the end. Unfortunately, a delay of 100 ns reduces the LIF signal significantly due to the exponential decay of the

fluorescence . The electron beam energy was calibrated by measuring the onset region of the excitation function of the He($3p\ ^3P \rightarrow 2s\ ^3S$) emission following electron impact excitation of the $3p\ ^3P$ state from the $1s\ ^1S$ ground state. The onset of this emission cross section is 23.0 eV . In order to compensate for the small expected LIF signal we increased the data accumulation time (see below) and we worked at a relatively high pushing pressure of about 20 Torr. The data acquisition procedure is similar to that described in section 4.4. The only difference is that the delay in gate A was 100 ns after the laser beam has traversed the interaction region, and the gates were open for 500 ns (corresponding to about 5 lifetimes of the He ($3p\ ^3P$) state) . Figure (5.4.2) shows the LIF signal of the He ($3p\ ^3P \rightarrow 2s\ ^3S$) emission at an electron impact energy of 20.4 eV taken under the above conditions and with a laser pulse energy of 20 μJ and an electron beam current of 0.8 μA. The data accumulation time was 68 min (17 data points, 4 min. data accumulation time per point). The total number of LIF counts (area under the peak) is 4890. Immediately after measuring the LIF signal in He, we measured the LIF signal of the P(6) rotational line of the N_2^+ ($X \rightarrow B$) (0,0) band by changing only the gas and the electron beam energy. Figure 5.4.3 shows the LIF signal of the P(6) rotational line of the (0,0) band at 100 eV electron beam energy. The delay in gate A was 55 ns after the laser beam has traversed the interaction region, the laser pulse energy was 28 μJ, the electron beam current was 8 μA, and the pushing pressure was 2.51 Torr. The data accumulation time was 50 min (100 data points, 30 s data accumulation time per point). The total number of LIF counts (area under the peak) is 5671. It should be noted that the LIF spectrum of the

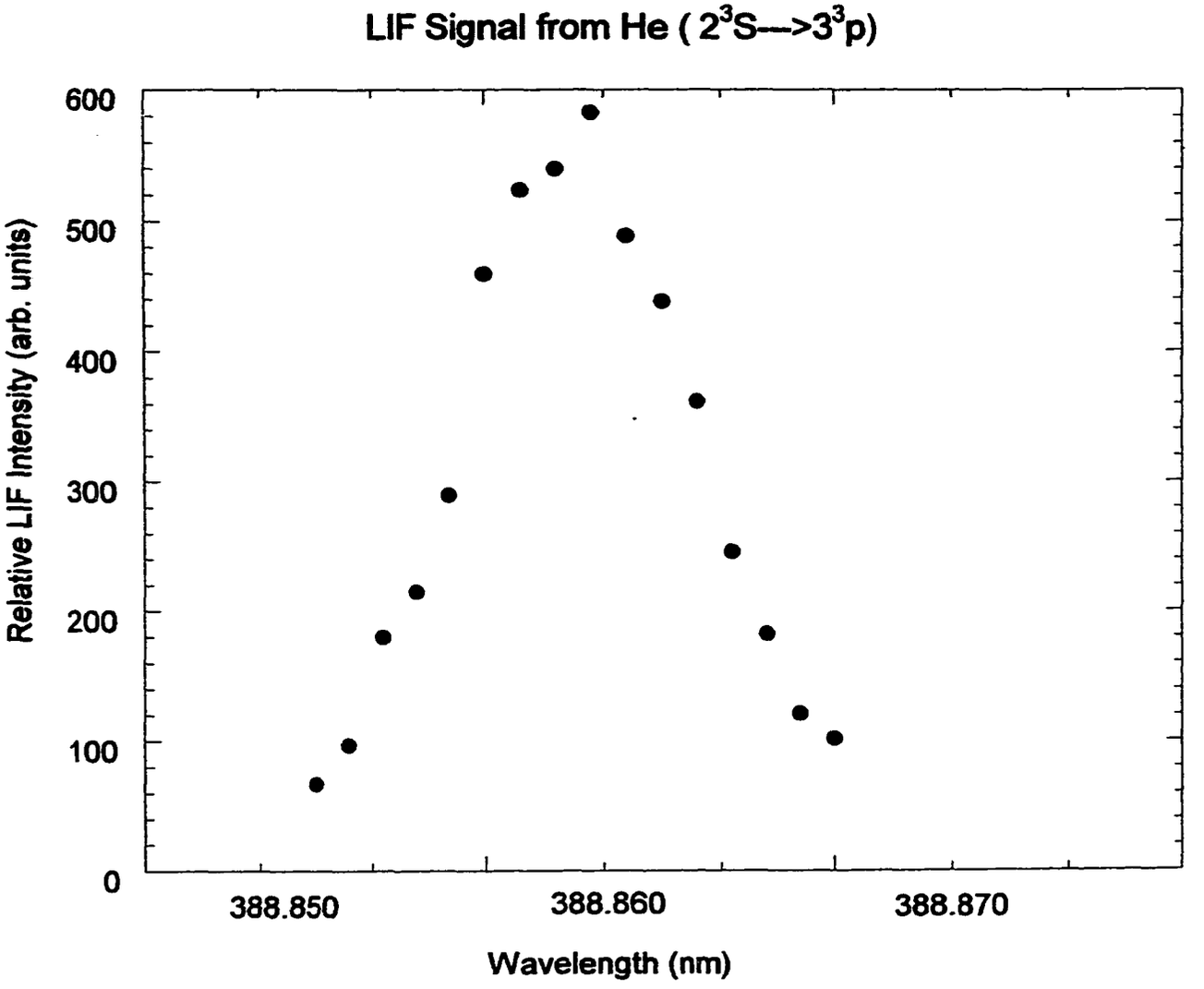

Figure 5.4.2

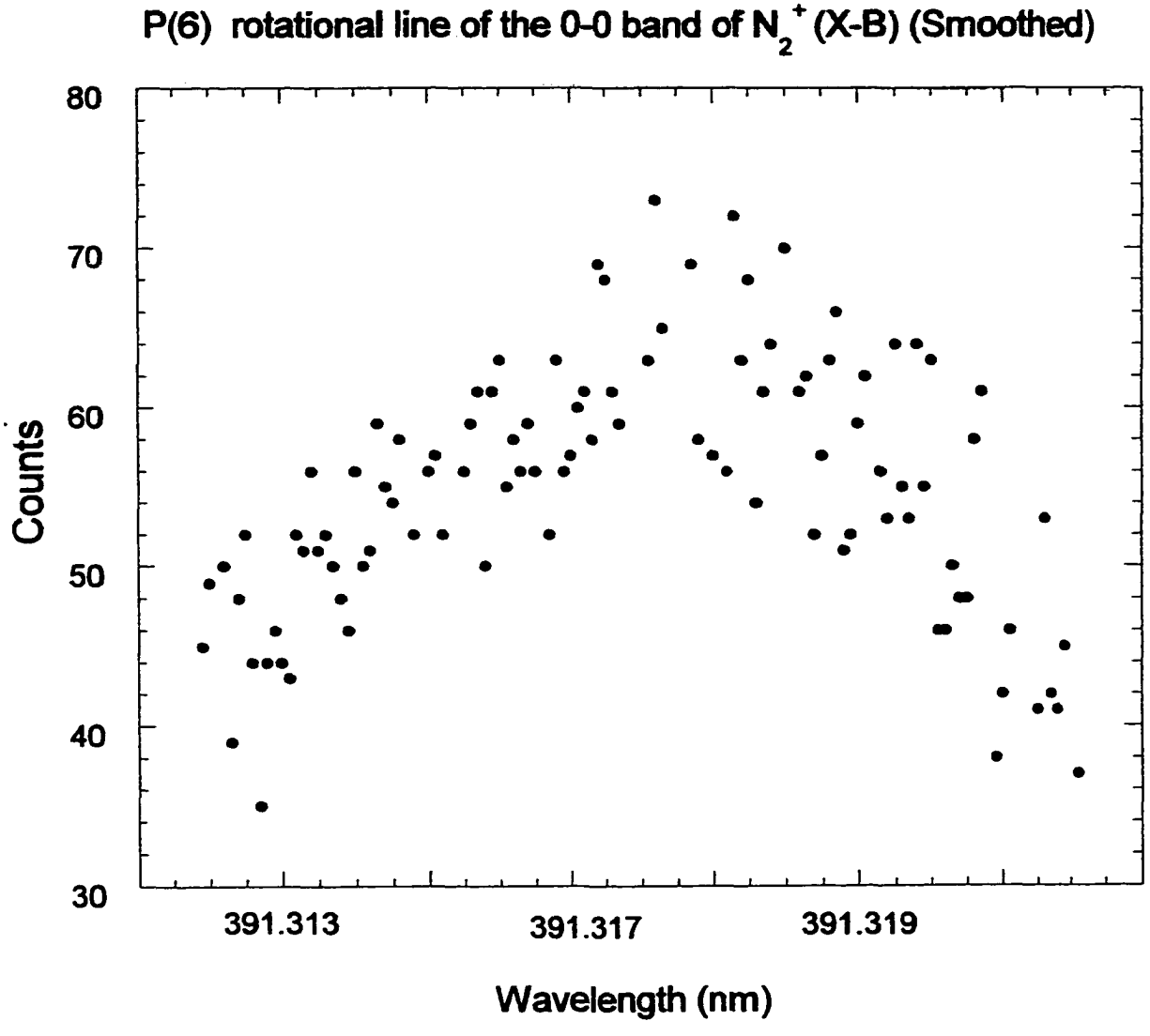

Figure 5.4.3

P(6) line shown in figure 5.4.3 was not taken under the optimum operating conditions (see discussion before). Since we were pumping and detecting at the same wavelength, a laser pulse energy of only 28 μJ was used and a time delay of 55 ns (about 1 lifetime of the N_2^+ (B) state) was introduced. In addition, to ensure the same size of the interaction region for both the He and the N_2 measurements, we used the same electron beam focusing conditions in He and in N_2 . The electron beam focusing was optimized for the He measurement at 20.4 eV and these focusing conditions are not necessarily the optimum conditions for the N_2 measurement at 100 eV.

Normalization Procedure

The total number of counts (area under the peak) of the LIF signal of He ($3p\ ^3P \rightarrow 2s\ ^3S$) emission at an electron energy of 20.4 eV is 4.488 Torr counts per minute per μJ per μA at 19.6 Torr. Here we have normalized the observed LIF signal to the electron beam current and the laser pulse energy, but not to the pushing pressure. The electron beam current and the laser pulse energy were in a region, where the LIF signal varies linearly with those parameters, whereas the pushing pressure was outside the linear region. The delay time between the time at which the laser pulse had traversed the interaction region and the time at which the signal was recorded was about 1 lifetime (100 ns) in the He measurement and slightly less in the N_2 measurement. Appropriate corrections to the data for this difference were made. The absorption coefficient for the He ($2s\ ^3S \rightarrow 3p\ ^3P$) is proportional to $0.0945 \times 10^8\ s^{-1}$ (West 1984), while the absorption coefficient for the N_2^+ ($X \rightarrow B$) (0,0) transition is proportional to $0.1214 \times 10^8\ s^{-1}$ (Laux et al 1992). Appropriate corrections to the data for this difference were made. In addition, the transmission of the

interference filter is 46% for the transition in He and 50% for the transition in N_2 which must be taken into account. As a consequence, the LIF signal of the $N_2^+(X \rightarrow B)$ (0,0) P(6) emission at an electron impact of 100 eV is 0.325 Torr counts per minute per μJ per μA at 2.51 Torr. Now we need to take into account that the $N_2(X, v=0) \rightarrow N_2^+ (X, v=0)$ cross sections represents 91.7% of the total $N_2(X, v=0) \rightarrow N_2^+ (X)$ cross section (Gilmore et al 1992). We also account for the fact that the $N_2^+(X \rightarrow B)(0,0)P(6)$ line corresponds to 10.95% of the total $N_2^+(X \rightarrow B)$ (0,0) transition (Hönl-London factor, Herzberg 1950), and that the N_2^+ (B, v=0) state decays to the N_2^+ (X, v=0) state with a branching ratio of 0.710 (Gilmore et al 1992). Therefore, the total LIF signal of the $N_2^+(X \rightarrow B)$ emission at an electron energy of 100 eV is 0.325 / (0.917*0.1095*0.710) = 4.559 Torr counts per minute per μJ per μA at 2.51 Torr. The pushing pressures used here were higher than those for which strict molecular flow occurs, and as a consequence, the relationship between the LIF signal and the pushing pressure is not linear. Therefore, it was necessary to quantify the deviation from the linear dependence of the observed LIF signal with the pushing pressure for both He and N_2 . For that purpose we used a procedure that was used successfully before to normalize optical intensities to pressures outside the molecular flow regime (Rogue et al. 1991) which is based on a variation of the molecular flow technique (Brinkman et al. 1981). Figure 5.4.4 shows the emission intensity (in arbitrary units) of the He $4p\ ^1P \rightarrow 2s\ ^1S$ transmission at 396 nm as a function of the pushing pressure. As shown, a linear fit was applied to the low pressure regime (below 1 Torr) and a quadratic fit was applied to the region above 1 Torr. The normalization procedure consists of converting the

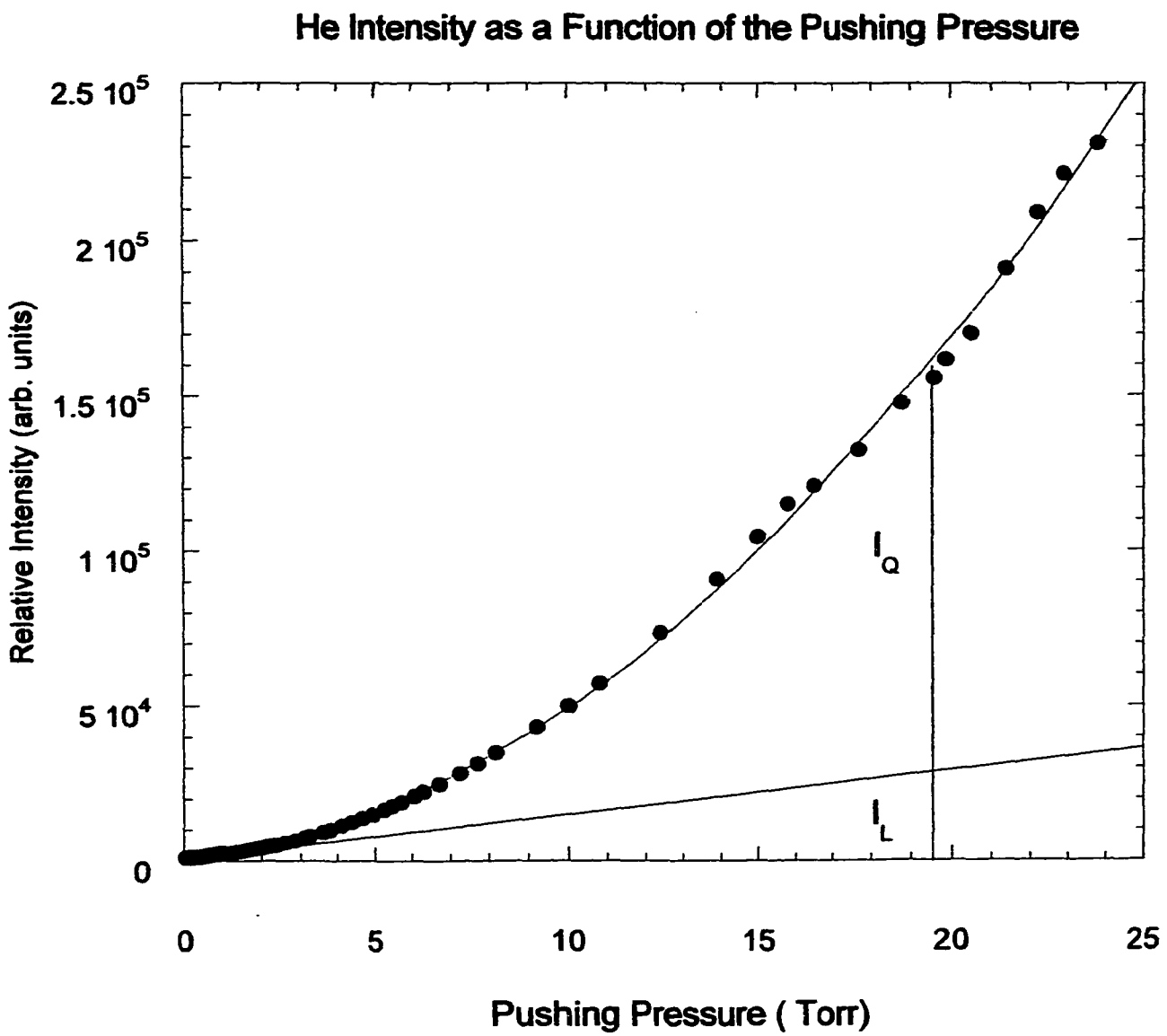

Figure 5.4.4

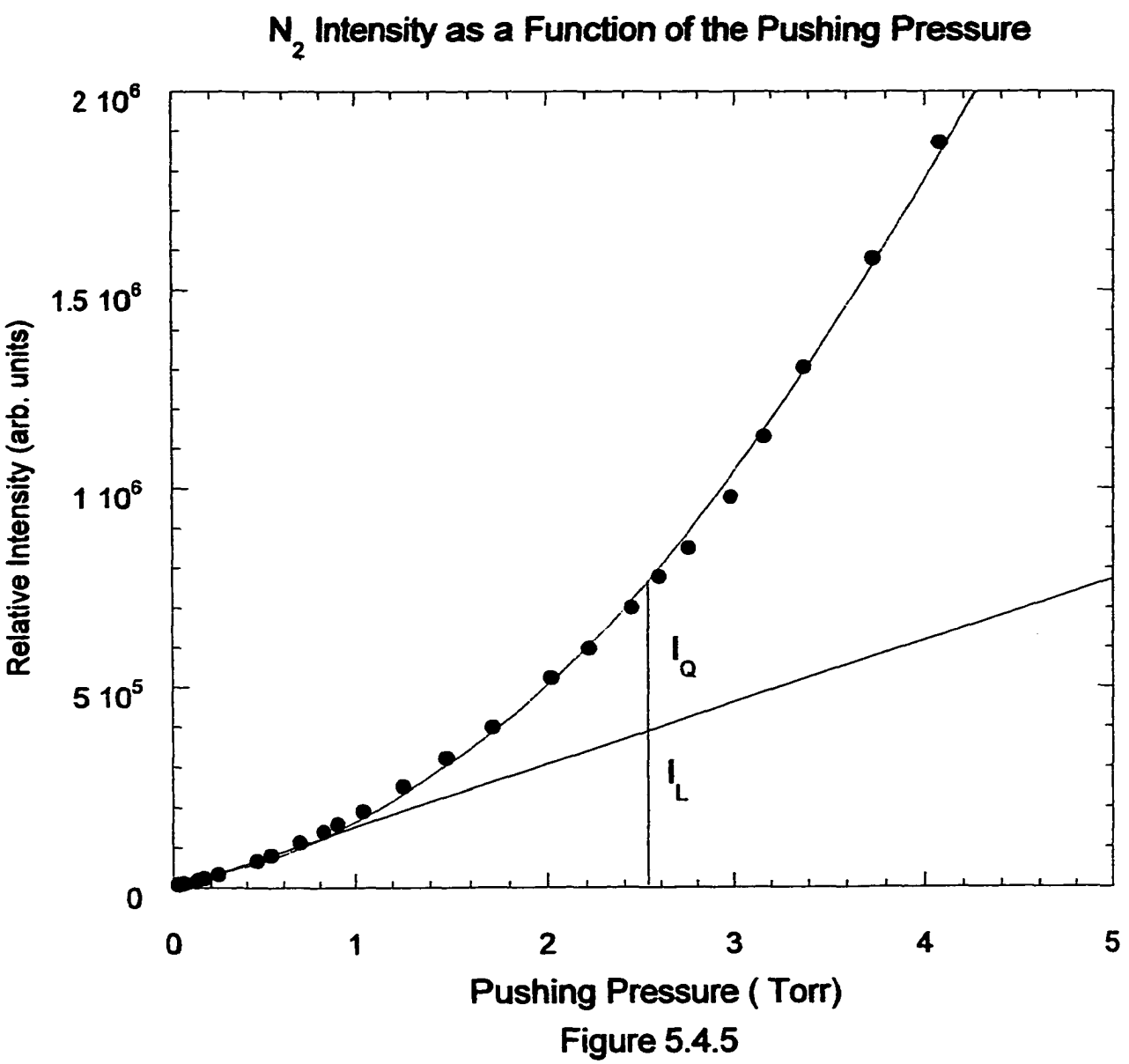

Figure 5.4.5

intensity measured at a given pressure outside the linear regime to the intensity corresponding to the linear fit extrapolated to the same pressure, $I_{norm} = I_{meas}(I_L/I_Q)$ as shown in the figure. I_L/I_Q in figure 5.4.4 is determined to be 0.204. From that it follows that the number of counts for the He transition properly normalized to the pushing pressure is 0.047 counts per minute per μJ per μA per Torr. Figure 5.4.5 shows a similar plot for the N_2^+ intensity of the B→ X (0,0) emission. Following the same normalization procedure as before, we find, I_L/I_Q to be 0.483. The number of counts for the N_2^+ (transition properly normalized to the pushing pressure is therefore 0.877 counts per minute per μJ per μA per Torr.

The ratio of the normalized LIF signals for N_2^+ and He can be equated with the ratio of the cross sections for the formation of N_2^+ (X) from ground-state N_2 at 100 eV and He (2s ^{3}S) from ground-state He at 20.4 eV. Using the well-known cross section for He (2s ^{3}S) formation at 20.4 eV (Borst 1974, Mason and Newell 1987, Lin and Anderson 1991) of 4.0 $X10^{-18}$ cm^2 we obtain the absolute cross section for the formation of N_2^+ (X) ions at 100 eV of 74.7 $X\ 10^{-18}$ cm^2.

Error Estimate

The uncertainty in our relative N_2^+ cross section measurement was 6.34% (see section 5.3).Table (5.4.2) shows the source of errors for the He measurement.

Description	Contribution to Uncertainty
1) pulse to pulse reproducibility of the laser pulse energy	< 5%
2) stability of electron beam current	< 1%
3) stability of gas beam density	< 1%
4) Pressure measurement[1]	< 3%
5) counting statistics	< 1.4

[1] Since we were working at a high pressure in the vacuum chamber there is an uncertainty in the pressure measurement which contributes 3% uncertainty to the cross section value.

Table (5.4.1)

We summed in quadrature the various systematic uncertainties (1-4) and added to it linearly the uncertainty due to the counting statistics. The uncertainty in the He measurement is 7%. Summing the uncertainty in the relative N_2^+ cross section measurement in quadrature with the uncertainty in the He measurement we find the error in the absolute N_2^+ cross section measurement to be 9% . Mason and Newell (1987) assigned an error margin of about 2.5% to the He (2s ^{3}S) cross section. This results in a total error margin of our cross section of about 10%. We note that the various absolute measurements of the He (1s ^{3}S→2s ^{3}S) cross section in the literature (Borst 1974, Masonand Newell 1987) carry individual error margins from 15% to 30%. However, there

is excellent agreement between the various absolute measurements, which were obtained from different experimental techniques (including optical as well as non-optical methods). On that basis, Mason and Newell (1987) argued that the level of confidence with which this cross section is known is much higher than the error margins of the individual measurements and assigned a 2.5% error margin to this cross section. This notion was supported in the recent review of Lin and Anderson (1991)

Results and discussion

Figure (5.4.6) shows the N_2^+ (X) cross section put on an absolute scale by normalization to the cross section value achieved in the present work. Also shown in the figure is the value of Doering and Yang (1996) at 100 eV and the respective error bars at 100 eV. In addition, we show the cross section value of Van Zyl and Pendleton (1995) at 100 eV, (without their quoted 45% error margin). This is motivated by the fact that the present data and the cross section of Doering and Yang (1997) result from experiment and carry experimental determined error margins. By contrast, the cross section value reported by Van Zyl and Pendleton (1995) results from the analysis of data reported by other authors and their uncertainty has been taken from other sources. There is a good agreement between our cross section and the absolute value at 100 eV obtained by Doering and Yang (1997), whereas the absolute value of Van Zyl and Pendleton (1995) is lower. However both the values of Doering and Yang (1997) and our cross section value fall within the estimated 45% uncertainty quoted by Van Zyl and Pendleton (1995) for their value. The good agreement between our cross section value and the value of Doering and Yang

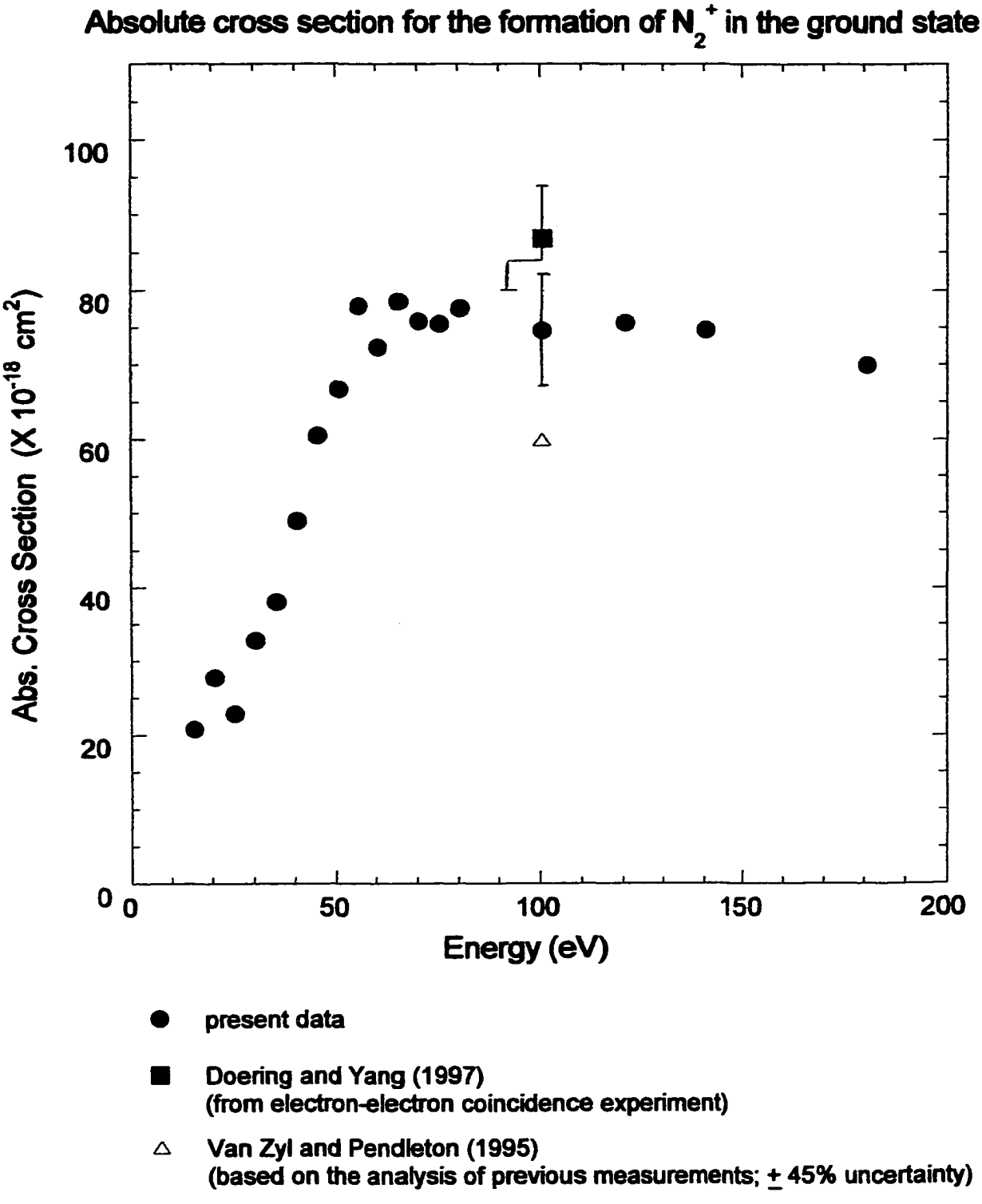

Figure (5.4.6)

(1997) supports the notion of Doering and Yang (1996)(see section 5.3) that the value of the previously accepted N_2^+ B state "benchmark" cross section of Borst and Zipf (1970) may have to be lowered but perhaps not by as much as Doering and Yang (1996) suggested .

Based on the work on the formation of final-state-specific N_2^+ ions by electron impact on N_2 in the past few years including the important result of the present thesis, the $N_2^+(X)$ cross section can now serve as a benchmark cross section. As such, the $N_2^+(X)$ cross section (at 100 eV) can serve as a calibration standard for future studies using the LIF technique to probe electron-impact ionization and dissociation processes.

Chapter 6. Summary and Future Directions

We developed a new technique to combine electron scattering and LIF technique to probe electron-impact-induced final-state-specific ionization and dissociation processes. We constructed, tested, and successfully utilized a triple-beam apparatus (crosses electron beam-gas beam-laser beam) for the absolute measurement of the N_2^+ (X) ionization cross section. Extensive studies were carried out to optimize the experimental conditions that yield a high LIF signal and a good signal-to-noise ratio. From LIF spectra obtained at various electron energies we obtained the absolute $N_2^+(X^2\Sigma_g)$ ionization cross section as a function of electron energy from threshold to 200 eV . The $N_2^+(X)$ cross section can now serve as a benchmark cross section. This clarifies a long-studying ambiguity in the N_2^+ ionization process induced by electron impact. Furthermore, the benchmark N_2^+ (X) cross section can now be used for the calibration of future neutral dissociation cross section studies , for e.g. we can now study the following dissociation processes in the same apparatus:

$$e^- + CH_4 \rightarrow CH(X^2\Pi) + 3H \quad (\text{or } H_2 + H)$$

$$e^- + CF_4 \rightarrow CF(X^2\Pi) + 3F \quad (\text{or } F_2 + F)$$

$$e^- + SiH_4 \rightarrow Si(3s^2 3p^2) + 4H \quad (\text{or } H_2 + H_2 \text{ or } 2H + H_2)$$

$$e^- + H_2O \rightarrow OH(X^2\Pi) + H$$

Fragment	Band /Line	Wavelength
CH	$A^2\Delta \rightarrow X^2\Pi$	430 nm
Si	$3s^23p4s\ ^1P^0 \rightarrow 3s^23p^2\ ^1D$	288 nm
	$3s^23p4s\ ^1P^0 \rightarrow 3s^23p^2\ ^1S$	391 nm
OH	$A^2\Sigma^+ \rightarrow X^2\Pi$	306.4 nm
CF	$A^2\Sigma^+ \rightarrow X^2\Pi$	233.2 nm

Methane (CH_4) is an important constituent of the terrestrial atmosphere and of the atmospheres of the planets Jupiter, Saturn, Uranus, Neptune and Pluto and some of their satellites. Methane has also emerged as a frequently employed constituent of feed gas mixtures in technological processing plasmas used in deposition applications (diamond and diamond-like carbon films). Cross sections for the production of the various fragments by electron collisional ionization and dissociation are important for the understanding and modeling of the chemistry in both planetary atmospheres and discharge plasmas.

SiH_4, is a frequently used constituent of low temperature processing plasmas used in fabrication of microelectronic devices and other semiconducting components. SiH_4 is also a constituent of the atmosphere of several other planets and their satellites.

The importance of OH radicals is due to their role in the breakdown of ozone molecules. The OH radicals also determine the lifetimes of common atmospheric constituents carbon monoxide, methane and sulfur dioxide.

CF_4 has been widely used in the semiconductor industry as a plasma etching gas. The neutral and ionic fragments of CF_4, generated in the low energy electron impact

(1-100 eV) play an important role in dry plasma etching of silicon and silicon compounds. To understand and model the plasma etching process using CF_4 one needs to know all types of electron impact cross sections. Especially important are the partial ionization and neutral dissociation cross sections.

In conclusion, the use of the LIF technique to measure the population densities of ground state products created by electron impact is a very powerful technique that is applicable to the study of a wide range of important processes.

Bibliography

Aarts, J. F. M., De Heer F.J., and Vroom D.A., Physica, **40**, 197 (1968)

Aarts, J. F. M., De Heer F.J., Chem. Phys. Letters **4** , 116 (1969)

Becker, K.H., "Electron-Impact Ionization and Dissociative Exitation of Halogen-Containing Molecules" Comments on Atomic and Molecular Physics 30 (5) 261-284, (1994).

Borst, W. L. Phys. Rev. A **9**, 1195 (1974)

Borst W.L. and Zipf E.C., Phys.Rev., **A1**,835 (1970).

Bouchoux A. M. and Bacis R. and Goure J. P. and Lambert A. M., Journal of Quantitative Spectroscopy and Radiation Transfer **16**, 451-456 (1976).

Brion C. E. and Hamnett A., in The Excited State in Chemical Physics, edited by Mcgowan J. W. (John Wiley and Sons, New York, 1981), Vol. XLV, p. 1-80.

Dalgarno, A., Latimer I., and. McConkey J. W, Planet. Space. Sci., **13**, 1008, 1965.

Darrach M., in Physics Department (The University of Windsor, Windsor, Ontario, Canada, 1990,), p. 170.

Demtröder W., Laser Spectroscopy, Springer-Verlag, Berlin, (1982)

Doering J. P. and J.Yang , J. Geophys. Res., **101**, A9, 19,723 (1996)

Doering J. P. and J.Yang , J. Geophys. Res., **102**, A5, 9683 (1997)

Dymond,E.G (1927). Phys.Rev.**29**,433-441

Exciton Inc., "Laser Dyes," (Exciton, Inc., Dayton, Ohio, 1992)

Eisberg and Resnick, Quantum Physics of Atoms, Molecules, Solids, Nuclei, and Particales (Wiley , New York, 1985)

Filippei, A. R., C. C. Lin, L. W. Anderson and J. W. McConkey, Advances in Atomic, Molecular and Optical Physics (1994), Vol.33, pp. 1-62.

Fons J. T. and Allen J. S. and Schappe R. S. and Lin C. C., Physical Review A **49**, 927-932 (1994)

Franck,J.,and Hertz,G. Verh. Dtch. Phys. Ges. (Berlin) **16**.457-467 (1914).

Freund, R. S., R. C. Wetzel, and R. J. Shul, Phys. Rev. A, **41**, 5861, (1990)

Gilbert P. G. and Siegel R. B., and Becker K., Physical Review A **41**, 5594-5599 (1990).

Gilmore, F., R. Laher, and P. J. Espy, J. Phys. Chem. Ref. Data, 21, 1005, 1992.

Giodmane J. A. and Wang T. C., Journal of Applied Physics **31**, 463-471 (1960).

Goembel, L., J. Yang, and J. P. Doering, J. Geophys. Res., **99**, 17,477 (1994)

Halas, S., and B. Adamczyk, Int. J. Mass Spectrom. Ion Phys., **10**, 157 (1972)

Hamamatsu Corp., "Photomultiplier Tubes, " (Japan 1985)

Herzberg G., Molecular Spectra and Molecular Structure Volume 1- Spectra of Diatomic Molecules (Van Nostrand Reinhold , New York 1950).

Holland, R. F. W. B. Maier , J. Chem. Phys., **58**, 2673 (1973)

Itikawa Y.,. Hayashi M.,. Ichimura A., Onda K., Sakimoto K., Takayanagi K., Nakamura M., Nishimura H. and Takayanagi T., J. Phys. Chem. Ref. Data,**15**,985(1986)

Kawazumi H. and Ogawa T. Chem. Phys. Letters **140**, (5) , 458 (1987)

Krishankumar E., and Srivastava S. K., J.Phys.B, **23**, 1893(1990).

Laux, C. O., and C. H. Kruger, J. Quant. Spectrosc. Radiat. Transfer, 48, 9, 1992

Lenard, P.(1902).Ann.Phys.**8**,149-198.

Lin C. C., and Anderson L. W. (1991) Adv. At. Mol. Opt. Phys. **29**, 1.

Lofthus A. and Krupenie P. H., Journal of Physical and Chemical Reference Data 6, 113-307 (1977).

Lumonics Inc., " Instruction Manual- Lumonics -Series HD 500 Pulsed Dye Laser," (Ontario, Canada, 1994)

Lutz Hüwel, Dean R Guyer, Guang-Hai Lin, and Stephen R. Leone J. Chem. Phys. 81 , 3520 (1984).

Märk, T. D. , "Ionization of Molecules by electron impact " in Electron Molecule interactions and their Applications, edit by L.G.Christophorou, vol. 1. (1984)

Märk, T.D., J. Chem. Phys., **63**, 3731 (1975)

Marmet,P.,and Kerwin,L.(1960). Can. J. Phys. **38**,787-796.

Massey , H. S. W., Burhop, E. H. S., and Gilbody, H. B. (1969). "Electronic and Ionic Impact Phenomena", Vol. I. And Vol. II., 2nd Ed. Calrendon Press Oxford.

Mason, N. J., and Newell, R. R. J. Phys. B., **20**, 1357 (1987)

McConkey J. W. , Woolsey J. M, and Bruns D.J. Planet. Space. Sci., **19**, 1192, (1971)

McConkey J. W. and Latimer I. D., Phys. Soc., **86**, 463 (1965)

McDaniel E.W. Atomic Collisions (1989) Ed. John Wiley & Sons

Mohr, C.B.O., and Nicoll, F. H. (1932). Proc. R. Soc. London A **138**, 229-244, 469-478.

Moor J. H. Davis C. C and Coplan M. A, Building Scientific Apparatus A Practical Guide to Design and Construction (Addison-Wesely, London, 1983)

Oppenheimer, J.R. (1928). Phys. Rev. **32**, 361-376

Peterson, J.R., Moseley J.T, J. Chem. Phys., **58**, 172 (1973)

Piper L.G., Green B.D., Blumberg W.A.M and Wolnik S.J., J.Phys.B,**19** 3327(1986). Press Oxford.

Ramsauer, a:Annalender Physik **64**, 513(1921) b: Annalender Physik **66**, 546(1921)

Rapp, D., P. Englender-Golden, and D. D. Briglia, J. of Phys., **42**, 4081 (1965)

Rogue, M.B., R. B. Siegel, K. E. Martus, V. Tarnovsky, and K. Becker, J. Chem. Phys **94** (1), 341-350 (1991)

Roth, A., Vacuum Technology, 3rd ed. (Elsevier Science Publishers B.V., Amsterdam, 1990)

Sarvastiva, B. N., and. Mizra I. M, Phys. Rev. **168**, 86, (1968)

Shaw, M., and Campos J., Quant J. Spectrosc. Radiat. Transfer, **30**, 73, (1983)

Siegel R.B (1996) (Thesis, City University of New York)

Skerbele, A. M., and Lassettere, E. N. (1964). J. Chem. Phys. **40**, 1271-1257

Stanton P.N and R. M. St. John, Journal of the Optical Society of America **59**, 252-260 (1969)

Steinfeld J. I. Molecules and Radiation (MIT Press 1986)

Thompson, J.J., Phil.Mag. October (1897)

Townsend and Bailey, Phil.Mag.**43**,593(1922)

Trajmar S.and, Cartwright D.C in Electron Molecule interactions and their Applications, edit by Christophorou L.G., vol. 1. (1984)

Van Zyl, B., and W. Pendleton Jr., J. Geophys. Res., **100**, 23, 755 (1995)

Van Zyl, B., M. W. Gealy, and H. Neumann, Phys. Rev. A, **28**, 2141, (1983)

West C. CRC Handbook of Chemistry and Physics, 65th Edition, CRC Press, Inc. Florida.

Yardley Y.T., Moor C.B.: J. Chem. Phys.**45**, 1066 (1966)

Zecca A, Karwasz G. P., Brusa R. S., La Rivesta del Nuovo Cimento , della Societa Italiana di Fisica **3** , 94-106 (1996)

Zetner P. W. and Darrach M. and Hammond P. and Westerveld W. B. and McConkey R. L. and McConkey J. W. , Chemical Physics **124**, 453-464 (1988).